

Final Report to NASA; NAG5-10520
Tectonic-Climate Interactions in Active Orogenic Belts: Quantification of
Dynamic Topography with SRTM data

Douglas W. Burbank ¹, Mike Oskin ¹, Nathan Niemi¹, Scott Miller²

¹Dept. of Geological Sciences, University of California, Santa Barbara, CA 93106

²Dept. of Geosciences, Pennsylvania State University, University Park, PA 16802

Introduction

This project was undertaken to examine the approach to steady state in collisional mountain belts. Although the primary thrust of this grant was to look at larger collisional mountain belts, such as the Himalaya, the Tien Shan, and Southern Alps, we began by looking at smaller structures represented by growing and propagating folds. Like ranges that are evolving toward a topographic steady state, these folds undergo a series of morphologic changes as they are progressively uplifted and eroded. We wanted to document the nature of these changes and to try to discern some of the underlying controls on them. We initially focused on the Wheeler Ridge anticline in southern California.

Subsequently, we progressed to looking at the topographic development and the effects of differential uplift and glaciation on the Kyrgyz Range in the northern Tien Shan. This range is unusual inasmuch as it is transformed along its length from a simple uplift with a largely preserved Mesozoic erosion surface arching across it to a highly dissected and heavily glaciated uplift in the region where uplift has been sustained at higher rates over longer intervals.

In efforts to understand the distribution of erosion rates at 10^3 - 10^5 year time scales, cosmogenic radionuclide (CRN) concentrations have been gaining increasingly widespread usage (Brown et al., 1995; Riebe et al., 2004; Riebe et al., 2001; Vance et al., 2003). Most studies to date, however, have been conducted in slowly eroding ranges. In rapidly eroding mountains where landslides deliver most of the sediments to the rivers, we hypothesized that CRN concentrations could be highly perturbed by the stochastic processes of landsliding. Therefore, we undertook the development of a numerical model that simulated the effects of both landsliding and grain-by-grain attrition within fluvial catchments. This modeling effort has shown the effects of catchment size and erosion rate on CRN concentrations and allows a prediction of where to sample to obtain the optimal erosion rate estimates using CRN techniques.

Finally, we developed computational techniques to operate on DEMs to extract useful information that would enable quantification of climate-erosion interactions. In particular, we worked on rapid techniques to define catchments of any given range of sizes, to extract channel gradients, to combine precipitation information to calculate discharge, and to utilize various stream-power models to determine the erosional energy within any given catchment within a transect.

Below, we briefly describe results from Wheeler Ridge, the Kyrgyz Range, the Nepal Himalaya, and our numerical modeling.

Background geology of the Wheeler Ridge, California

The Wheeler Ridge anticline is the outermost structure in a fold-and-thrust belt (Davis and Namson, 1986) that uplifts the San Emigdio Mountains at the interface between the northern edge of the Transverse Ranges and the southern end of the San Joaquin valley in Southern California (Medwedeff, 1992). Wheeler Ridge is the surface expression of the anticline (Hoots, 1930), and is an east-west trending, east-plunging anticline whose eastern terminus is buried beneath the modern depositional surface (Figure 1). Wheeler Ridge is approximately 10 km long, up to 3 km wide, and has a maximum relief of about 500 meters (Medwedeff, 1992). Extensive subsurface and surface data supports the interpretation that Wheeler Ridge is underlain by a north-directed wedge thrust that merges southward into the basal detachment (Medwedeff, 1992). Because a 7 ka surface has been uplifted above the modern depositional plain, we infer that the Wheeler Ridge anticline is an actively growing structure, even though no recent earthquakes have occurred on the Wheeler Ridge Thrust.

The topography of the Wheeler Ridge anticline comprises abandoned and uplifted Holocene and late Pleistocene alluvial surfaces. Particularly at the eastern end of the anticline, these surfaces are very well preserved; to the west, the surfaces are increasingly dissected leaving remnants on interfluvies. The forelimb of the anticline lies on the northern side of Wheeler Ridge and is generally steeper and more dissected than the southern side. Previous work has dated several of the surfaces using radiocarbon dating and comparative soil stratigraphy (Keller et al., 1998, 1999). These results indicate that the anticline is propagating eastward at about 29 mm/yr, that the rate of fold uplift of the easternmost portion of the fold is 3 mm/yr and that folding initiated about 400 ka ago (Keller et al., 1998, 1999; Medwedeff, 1992).

The availability of subsurface structural data, dated geomorphic surfaces, aerial photographs shot periodically since 1930, and a 10-meter TOPSAR digital elevation model makes Wheeler Ridge an ideal place to quantify the tectonic geomorphology of an actively growing structure and to calibrate the resolution of the DEM. Below we describe the methods used to constrain the temporal and spatial development of topography in response to surficial and tectonic processes.

Geomorphology of the Wheeler Ridge Fold

Because Wheeler Ridge is propagating to the east, there is a progressively larger amount of uplift and erosion from east to west. This shows up very clearly in the geomorphology, whereby smooth surfaces characterized by few stream valleys characterize the newly uplifted surfaces, whereas deep dissection and steep slopes characterize the older parts of the fold. Using the 10-m DEM, we can quantify spatial variations in the magnitude of erosion (Figure 2). These clearly indicate that, ignoring the water and wind gaps, the western part of the fold has experienced far greater erosion.

In an effort to quantify the character of and controls on that erosion, we have divided the fold surface into forelimb and backlimb surfaces and into age-dependent zones (Figure 3) according to the ages and criteria set forth by Keller et al. (1998, 1999). This delineates a suite of surfaces ranging from <10ky to >200 ka along a 5 km length of the fold. There are systematic changes in the slope angles and hypsometry along the fold (Fig. 4). Hillslope angles steepen, but they do not vary linearly with uplift. In fact, the diminished difference in slope angles between areas Q4 and Q5 suggest that the threshold angle for landsliding is being approached, such that the slopes will not steepen much above this level. The hypsometry shows that, in the older parts of the fold, the topography becomes more evenly distributed. Early on, the fold has an uplifted crest with short, steep limbs, such that most of the topography is concentrated near the crest. Over time, the limbs lengthen and both streams and landslides cut through the uplifted surface, such that the topography becomes more evenly distributed.

We can use the present stream gradients in conjunction with the reconstructed, pristine surface (Fig. 2), to estimate the amount of erosion in each stream valley. When we do this calculation both for the streams alone and for the entire landscape, we find that there is a dramatic increase in erosion rate associated with the older part of the fold (Figure 5). The reasons for these differences are not obvious. With the exception of one outlier, the rates show a good correlation with mean channel curvature (m/n) and with the mean hillslope gradient. When we use a stream power law to predict erosion rates, there is also a generally good correlation (Figure 6). Surprisingly, we note that within any area with consistent uplift, the north-facing channels are always less steep than the south-facing ones. The reason for this is unknown at present. We suggest that the drier conditions, more sparse vegetation, and thicker soil carbonate leads to

higher runoff on the southerly slopes, thereby creating higher stream power for a given slope and catchment and permitting the same rate of erosion to be sustained on gentler slopes. We are pursuing this further to try to understand what is controlling the erosion patterns along this growing fold.

Pre-Steady-State Topography of the Kyrgyz Range, Tien Shan

Studies of the geomorphology of the Kyrgyz Range were undertaken to elucidate the role of glacial and fluvial weathering on the establishment of steady-state topographic relief. The Kyrgyz Range is a 250 km-long, east-west trending range within the Tien Shan of Central Asia. Drainage basins within the Kyrgyz Range typically traverse 3 to 4 km of topographic relief, and the upper reaches of most of these drainages are presently glaciated. The larger drainage systems of the Kyrgyz Range drain to the north, across the active, main frontal thrust system which builds the range (Figure 1). South-facing catchments are much smaller with less well-developed tributary networks.

An unconformity formed on resistant Paleozoic metamorphic and crystalline rocks forms a prominent pre-uplift marker horizon which is to be used in this study to estimate erosional denudation of the Kyrgyz Range. Extensive exposures of this unconformity surface on the east end of the range indicate that stream systems in this region are less mature than further west. The present study of the Kyrgyz Range exploited this along-strike variation in drainage development to explore the evolution of a range toward steady-state topography. Also, extensive glaciation in the upper elevation reaches of the Kyrgyz Range provided a strong signal of the role of glacial processes in the development of drainage networks.

Overall, we examined the topographic development and the effects of differential uplift and glaciation on the Kyrgyz Range in the northern Tien Shan. This range is unusual inasmuch as it is transformed along its length from a simple folded uplift with a largely preserved erosion surface arching across it to a highly dissected and heavily glaciated uplift in the region where uplift has been sustained at higher rates over longer intervals.

We have defined the differential uplift using extensive fission-track transects that enable us to define the changing height of the partial annealing zone as well as the time of the initiation of deformation along strike. The fission-track and topographic results are described in a manuscript that has been submitted to *Tectonics* [Edward R. Sobel, Michael Oskin, Douglas Burbank, and Alexander Mikolaichuk, Exhumation of basement-cored uplifts: Example of the Kyrgyz Range quantified with apatite fission-track thermochronology: *Tectonics*, in review]. These data yield a clear image of outward propagation from the core of the range. In addition, we have mapped the erosion surface and characterized the topographic changes (using the SRTM DEM) to define the gradual dissection and removal of the erosion surface in the older (Miocene), more uplifted parts of the range, as well as changes in slopes, catchments, and channels with increasing dissection. Methods to analyze these topographic data have been developed with the intention of rapid application to DEMs anywhere. Thus, considerable effort has been made to build a set of portable routines to automatically analyze stream networks.

For example, a striking attribute of the along-strike topographic variation of the Kyrgyz Range is the size and geometry of watersheds from east to west. This trend appears to strongly reflect the maturity of the drainage system. Thus, it appears that understanding the topographic evolution of the Kyrgyz Range requires a 3-dimensional approach to measurement of stream systems. To address this issue, a set of flexible, modular routines were developed that extract and analyze all tributary streams of a watershed. Results are maintained within a georeferenced framework using Arc-Info GIS so that spatial relationships may be compared within a drainage system or with other geologic features. To document the extent of glaciation, data for over 500

glaciers from the Russian Catalog and georeferenced panchromatic 15m ASTER imagery have been integrated into this database.

Our analyses indicate that glaciation plays a strong role in forming mature drainage networks in the Kyrgyz Range. Large, mature drainages within the western half of the study area contain extensive regions of glaciated uplands. Within the largest drainage basins, these upland areas are expanded along the range crest. Interestingly, the highest peaks within the Kyrgyz Range occur not at the range crest, but on the ridges between these mature watersheds. It appears that vigorous glaciation of the range crest has promoted an increase in the catchment area of a few watersheds, leaving wider ridges between the major watersheds that support higher peaks. These ridges also display a pronounced mismatch between downcutting of the trunk stream and downcutting of the tributaries. Typically, high-elevation, low relief uplands drain into steep tributary streams that then join the gently-sloping central trunk stream. Moraines at the outlet of these trunk streams indicate complete glaciation during the Pleistocene and it is likely that glacial downcutting is the primary cause of the mismatch between trunk streams and the inter-watershed ridge areas.

In sharp contrast to the large, extensively glaciated north-facing drainages of the Kyrgyz Range, the south side of the range is characterized by far less mature, smaller, and steeper drainages inset into a partially dissected unconformity surface. Many of these streams have poorly-developed concave profiles or slope parallel to the unconformity surface. Even where the uppermost reaches of these drainages is occupied by a glacier or cirque, the drainage slope appears to be mostly unaffected by glaciation. Two possible causes for the contrast between the north and south side of the Kyrgyz Range are proposed: 1. The southeast side of the range has been exhumed much more recently than the more well-developed central part of the range. This may be caused by propagation of the frontal thrust system to the east. This however does not explain the asymmetry of the drainage network in the central part of the range. 2. A pronounced rain-shadow affect has restricted precipitation on the south side of the range. The preliminary conclusion from these observations is that formation and integration of a tributary network is a critical step in development of a mature stream profile.

Our efforts to quantify the effects of glaciation on the development of stream networks have yielded new insights on how glaciers modify large-scale topography. Some of these results have been submitted to *Geology* for review [Oskin, M.E., and Burbank, D.W., Alpine landscape evolution dominated by cirque retreat: see attached manuscript]. In combination with analysis of aerial photos and satellite imagery, we have used the SRTM data extensively to quantify the extent of glaciations, changes in snowlines, differences between fluvial and glacial catchments, and rates of headward retreat by glaciers.

A break in relief and stream channel concavity probably related to glacial erosion occurs at ~2600m within several drainages on the north side of the range. This elevation is 1200-1500m lower than the present snowline in the Kyrgyz Range, reported at 3800 to 4100m for numerous glaciers within the range, and is consistent with Pleistocene ELA estimates. The south side of the range displays a much less well-developed signature of glacial erosion, as described above. Subtle shallowing of stream profiles above 3500m elevation indicates enhanced glacial erosion in the uppermost reaches of the south-facing streams. This suggests a considerable difference on Pleistocene ELA between the north and south side of the ranges, and lends support to the rain-shadow hypothesis proposed above. Analysis of the SRTM data shows that initially streams form as shallow linear troughs on the erosion surface. These have little concavity and are analogous to halfpipes, with rather uniform valley width along their lengths. As glaciation occurs

in their headwaters, the upper valley profile flattens and the valley head widens. Where the erosion surface is well preserved, we can show that the glaciers initially erode headwards 2-4 times faster than they erode downwards. This surprising result emphasizes the effects of efficient erosion processes in the headwall area and of relative ineffectual vertical erosion by the juvenile glaciers.

Cosmogenic radionuclide erosion rates in rapidly denuding landscapes

Samples of fluvial sediment for cosmogenic radionuclides (CRNs) have great potential because fluvial samples represent a natural, stochastic integration of all upstream concentrations. Landslides, however, have the potential to perturb CRN concentrations away from the long-term mean because they can incorporate rocks that have received little cosmic ray exposure. In such cases, they can produce low CRN concentrations that suggest rapid denudation. Alternatively, because landslides are infrequent events, it is likely that even in small valleys with landslides, one has not occurred recently. Hence, when collecting fluvial samples for CRN analysis, one should ask, "How large a catchment do I need to sample to iron out all of the CRN irregularities due to landsliding?" and "How well does a well-integrated downstream sample represent the actual mean of total sediment flux?" To address these questions, we built a numerical model that utilizes a DEM, calculates CRN concentrations and production throughout the study area, scatters landslides across the area, recalculates CRN distributions in both the remaining bedrock and in the landslide debris. We examined different rates of grain-by-grain bedrock weathering in combination with various rates of landsliding (0.7 to 9.7 mm/yr that span most of the naturally occurring rates. The results of this study are reported in the attached paper that is in press at EPSL: Nathan Niemi, Mike Oskin, Douglas Burbank and Arjun Heimsath, Effects of Bedrock Landsliding on Cosmogenically Determined Erosion Rates: EPSL in press: see attached.

Climate-erosion coupling in the central Himalaya

We utilized both SRTM and DTED data in the analysis of channels and catchments in the central Himalaya. Our related research had discovered that rapid erosion rates persist into the rain shadow of the Himalaya. So, despite a 10-fold decrease in monsoon precipitation, the long-term rate of erosion (as indicated by apatite fission-track dating) remains steady (and rapid) in the northern, arid part of the study area. To examine why this might happen and in particular how rivers with less rainfall could incise just as rapidly in the dry area as in the wet regions, we extracted all 3-7 km² catchments in the DEM, measured their channel slopes, combined them with a calibrated rainfall model to calculate runoff, and then calculated changes in specific stream power. We discovered that about half of the "erosion energy" deficit was made up by narrowing of channels in the arid areas. These results were reported in an attached Nature article: Burbank, D. W., A. E. Blythe, J. Putkonen, B. Pratt-Sitaula, E. Gabet, M. Oskin, A. Barros, and T. P. Ojha (2003), Decoupling of erosion and precipitation in the Himalayas, *Nature*, 426, 652-655.

Overall, as a result of this grant, one article has been published, one is in press, another is in review, and a fourth is still being completed by a graduate student.

References

- Brown, E.T., Stallard, R.F., Larsen, M.C., Raisbeck, G.M., and Yiou, F., 1995, Denudation rates determined from the accumulation of in situ-produced ¹⁰Be in the Luquillo experimental forest, Puerto Rico: *Earth and Planetary Science Letters*, v. 129, p. 193-202.

- Davis, T. L. and Namson, J. S. (ed.), 1986. Geologic transect across the Western Transverse Ranges: Los Angeles, California, Pacific Section, Society of Economic Paleontologists and Mineralogists, 74 p.
- Hoots, H. W., 1930, Geology and oil resources along the southern border of the San Joaquin Valley, California: U.S. Geological Survey Bulletin, v. 812, p. 243-332.
- Keller, E. A., Gurrola, L., and Tierney, T. E., 1999, Geomorphic criteria to determine direction of lateral propagation of reverse faulting and folding: *Geology*, v. 27, p. 515-518.
- Keller, E. A., Zepeda, R. L., Rockwell, T. K., Ku, T. L., and Dinklage, W. S., 1998, Active tectonics at Wheeler Ridge, southern San Joaquin Valley, California: *Geological Society of America Bulletin*, v. 110, p. 298-310.
- Medwedeff, D. A., 1992, Geometry and kinematics of an active, laterally propagating wedge thrust, Wheeler Ridge, California, in Mitra, S. and Fisher, G.W., eds., *Structural Geology of Fold and Thrust Belts*: Baltimore, Johns Hopkins University Press, p. 3-28.
- Riebe, C.S., Kirchner, J.W., and Finkel, R.C., 2004, Erosional and climatic effects on long-term chemical weathering rates in granitic landscapes spanning diverse climate regimes: *Earth and Planetary Science Letters*, v. in press.
- Riebe, C.S., Kirchner, J.W., Granger, D.E., and Finkel, R.C., 2001, Strong tectonic and weak climatic control of long-term chemical weathering rates: *Geology*, v. 29, p. 511-514.
- Vance, D., Bickle, M., Ivy-Ochs, S., and Kubik, P.W., 2003, Erosion and exhumation in the Himalaya from cosmogenic isotope inventories of river sediments: *Earth and Planetary Science Letters*, v. 206, p. 273-288.
- Zepeda, R. L., Keller, E. A., Rockwell, T. K., Ku, T., and Dinklage, W. S., in review, Active tectonics and soil chronology of Wheeler Ridge, Southern San Joaquin Valley, California: *GSA Bulletin*.

**Publications resulting from this research
(see attached manuscripts)**

- Michael Oskin and Doug Burbank, Alpine landscape evolution dominated by cirque retreat (in review, *Geology*)
- Nathan Niemi, Mike Oskin, Douglas Burbank and Arjun Heimsath. Effects of Bedrock Landsliding on Cosmogenically Determined Erosion Rates (in press, *EPSL*)
- Burbank, D.W., Blythe, A.E., Putkonen, J., Pratt-Sitaula, B., Gabet, E., Oskin, M., Barros, A., and Ojha, T.P., 2003, Decoupling of erosion and precipitation in the Himalayas: *Nature*, v. 426, p. 652-655.
- Edward R. Sobel, Michael Oskin, Douglas Burbank, Alexander Mikolaichuk, Exhumation of basement-cored uplifts: Example of the Kyrgyz Range quantified with apatite fission-track thermochronology (in review: *Tectonics*).

In review (*Geology*): Alpine landscape evolution dominated by cirque retreat

Michael Oskin University of North Carolina at Chapel Hill, Chapel Hill, NC 27599-3315, oskin@unc.edu

Doug Burbank Department of Geological Sciences, University of California, Santa Barbara, CA, 93106, burbank@crustal.ucsb.edu

Abstract

Despite the abundance in alpine terrain of glacially dissected landscapes, the magnitude and geometry of glacial erosion can rarely be defined. In the eastern Kyrgyz Range, a widespread unconformity exhumed as a geomorphic surface provides a regional datum with which to calibrate erosion. As tectonically driven surface uplift has progressively pushed this surface into the zone of ice accumulation, glacial erosion has overprinted the landscape. With as little as 500 m of incision into rocks underlying the unconformity, distinctive glacial valleys display their deepest incision adjacent to cirque headwalls. The expansion of north-facing glacial cirques at the expense of south-facing valleys has driven the drainage divide southwards at rates up to 2 to 3 times the rate of valley incision. Existing ice-flux-based glacial erosion rules incompletely model expansion of glacial valleys via cirque retreat into the low-gradient unconformity remnants. Local processes that either directly sap cirque headwalls or inhibit erosion down-glacier appear to control, at least initially, alpine landscape evolution.

Introduction

The remarkable coincidence of glacial snowlines with average height of high mountains suggests that glaciation may exert primary control on mountain-range elevation, irrespective of tectonic rates (Broecker and Denton, 1990; Brozovic et al., 1997; Montgomery et al., 2001; Spotila et al., 2004). Thus the topographic evolution that accompanies the transformation of nascent, unglaciated landscapes to highly glaciated ones is a key to unraveling the erosional component of a climate-erosion feedback system (Molnar and England, 1990). Comparative geomorphic studies support contentions that glaciation enhances valley erosion and topographic relief (Brocklehurst and Whipple, 2002; Kirkbride and Matthews, 1997; Montgomery, 2002; Small and Anderson, 1998). Observations of planimetric cirque expansion (Federici and Spagnolo, 2004; Olyphant, 1981) and truncated glacial valleys (Brocklehurst and Whipple, 2002) indicate cirque retreat could play a competing role by expanding valleys horizontally and removing high topography. The significance of cirque retreat in limiting mountain range height, however, has not been conclusively established.

For tectonically active mountain ranges undergoing surface uplift, their progressive penetration into the zone of glaciation can provide a proxy for transformation of landscapes during the well-documented late Cenozoic cooling (Shakleton and Opdyke, 1973). Growth of the Tien Shan (Fig. 1, inset), when combined with its unique geologic history, establishes a natural laboratory to investigate glacial valley erosion and cirque retreat. Basement-cored uplifts of the northern Tien Shan exhumed resistant Paleozoic plutonic and metamorphic bedrock from beneath unconsolidated Cenozoic non-marine sedimentary strata. A regionally extensive, pre-Cenozoic low-relief unconformity separates these units (Chediya, 1986). In the arid environment of central Asia, significant areas of this exhumed unconformity form geomorphic surfaces that appear little modified by fluvial erosion, and instead faithfully delineate the geometry of range-scale folding (Burbank et al., 1999). When surface uplift causes ranges to intersect the local Pleistocene glacial equilibrium-line altitude (ELA), however, glacial erosion may cause significant incision of the Paleozoic rocks underlying the unconformity. Reconstruction of this

datum over glaciated topography thus enables reliable estimation of the magnitude of glacial bedrock erosion.

Late Cenozoic uplift of the Kyrgyz Range provides a structurally well-controlled experiment from which to measure sequential glacial landscape evolution. Uplift occurs via hangingwall folding and slip on a reverse fault system that emplaces resistant Paleozoic quartzite, metaconglomerate, granitic, and metavolcanic rocks northward over Miocene through Quaternary foreland-basin strata. Bedrock thermochronology supports erosion rates of ~1 km/Myr from 3 Ma to present in the central, highest part of the range (Bullen et al., 2001). Detrital apatite fission-track ages from foreland-basin strata and modern rivers indicate progressively less exhumation in the eastern Kyrgyz Range (Bullen et al., 2003), consistent with preservation of exhumed, tilted remnants of the unconformity on over 50 km of its south-facing slope (Fig. 1). These observations support an eastward propagation or an eastward-declining rate of coeval rock and surface uplift that has progressively elevated the range crest into the zone of glaciation above the local Pleistocene ELA.

Glacial Erosion of the eastern Kyrgyz Range

Exhumation of the pre-Cenozoic unconformity as a geomorphic surface underpins the quantification of erosion. Swath topographic profiles (Fig. 2) reveal minimal topographic relief development on its unglaciated south-facing slope. Maximum elevations of these areas are defined by low relief, upland surfaces with concordant elevation and southward tilt preserved between larger, incised drainages that descend from the range crest (Fig. 3). These surfaces merge with outcrops of the unconformity beneath Cenozoic strata at the base of the range. A fourth-order polynomial surface with curvature of $<1^\circ/\text{km}$ fit to the distribution and tilt of mapped remnants defines a continuous envelope over the south-facing slope of the range (Fig. 4). This envelope captures the mapped unconformity within ± 100 m (1σ), over >1500 m of structural relief. Tilting of the restored unconformity surface increases both with elevation and from east to west, consistent with a gradient of slip over a curvilinear reverse fault at depth.

Comparison of three adjacent catchments incised into the south-facing slope of the Kyrgyz Range reveals details of the form of initial glacial erosion and the continuity of interfluvial geomorphic surfaces (Fig. 5). All three streams descend at steep ($>8^\circ$) slopes incised <600 m into the tilted unconformity preserved at concordant undissected interfluves. The fluvial part of each valley is analogous to a half-pipe, with uniform valley width and fairly uniform incision. In contrast, the glaciated parts of these catchments display significant widening and deepening with the greatest incision at their glaciated headwaters. Adjacent glaciated catchments show a similar pattern of maximum incision at their headwaters (Fig. 4).

North-facing glaciated catchments of the eastern Kyrgyz Range consist of high-elevation, gently sloped U-shaped valleys linked to steep, V-shaped canyons that descend to the range-bounding reverse fault (Fig. 1). Absence of preserved remnants of the unconformity near the fault limits precise estimation of incision of these catchments. To conservatively evaluate glacial incision by north-facing catchments, the slopes of north-facing glaciated valleys are examined with respect to slope of the adjacent, south-dipping unconformity surface preserved at the range crest (Fig. 4). The difference of these slopes defines a ratio of valley length to valley incision (0.3–0.4) that is significantly less than the average slope (0.8 ± 0.1 (1σ), $n=66$) of cirque headwalls along the range crest.

The presence and extent of glaciation in north-facing catchments corresponds to changes of trend and elevation of the range crest. Outside of the zone of glaciation, the range crest tracks ~5 km south of the trace of the range-bounding reverse fault, the range shape reflects growth of the underlying geologic structure (e.g. Fig. 2a), and peak elevations climb steadily from 2400 m near the Chu River in the east to 3400 m at the first glaciated catchment. Within the zone of

glaciation, peak elevations stabilize at ~4000 m elevation and the position of the range crest shifts systematically southward relative to the range front in proportion to the degree of Late Pleistocene ice cover (e.g. Figs. 2b through 2d).

Discussion

The gradient in rock uplift of the eastern Kyrgyz Range permits along-strike space-for-time substitution of observations of incision of the range by glaciers. Because the range is rising above an active reverse fault at approximately 1 km/Ma, glaciation of the eastern range tip is likely to have occurred sequentially during the Pleistocene. Although each valley has a unique incision history, spatial trends of landscape evolution that are shared among several adjacent valleys may represent temporal trends within an individual valley. Much of the transformation of the Kyrgyz Range into its glacially sculpted form involves competition between adjacent catchments that drives migration of drainage divides over time. Exhumation of the pre-Cenozoic unconformity as a geomorphic surface datum affords a unique opportunity to quantify the degree of glacial incision that accompanies progressive changes in valley form.

Rapid formation of gently sloped upland U-shaped valleys accompanies initial glacial erosion of the eastern Kyrgyz Range. Glaciers on south-facing slopes accomplish this by widening and eroding their valleys deeper than adjacent fluvial valleys, evidenced by incision and valley-width maxima near the range crest (Fig. 5). Approximately 0.5 km of incision into the unconformity surface forms these characteristically glaciated valleys, consistent with low erosion depths required to obtain stable glacial valley cross-sections in numerical simulations (Harbor, 1992).

Systematic, relative southward migration of the drainage divide of the eastern Kyrgyz Range shows that cirque retreat also accompanies initial glacial erosion. Expansion of north-facing valleys via glacial cirque retreat provides a consistent explanation for these spatial trends of landscape evolution with progressive rock uplift above the local ELA (Fig. 6): (1) range crest elevation stabilizes at ~4000 m with the onset of erosion by glaciers; (2) further uplift and tilting of the range is accompanied by southward relative migration of the drainage divide; and (3) the pre-Cenozoic unconformity is preserved as a geomorphic surface at the range crest. Peak heights remain constant along trend and the range crest preserves remnants of the exhumed unconformity because the divide has shifted southward with progressive uplift and glacial erosion (Fig. 2). In effect, during initial glacial erosion, the range crest remains more or less pinned to the intersection of the 4000-m contour line with the tilted unconformity. This explanation requires that a competitive advantage for cirque erosion exists for north-facing catchments over their south-facing counterparts and that glacial erosion of the Kyrgyz Range occurs, at least initially, by a combination of cirque retreat and glacial valley incision.

Alternative origins for southward migration of the divide include differential fluvial incision, exposure of lithologies that resist glacial erosion, or formation in place of the present divide by range-scale folding. Range-scale folding may be ruled out as an explanation because peaks and ridges north of the present divide are locally at the same elevation or higher than the exhumed unconformity preserved at the divide (Figs. 1, 2c, and 2d). This geometry requires that the structural axis of the Kyrgyz Range trends north of the present drainage divide in the zone of glacial erosion. Metasedimentary rocks that underlie the glaciated area strike transverse to valleys and dip steeply, inconsistent with lithologic control of valley floor elevation. It is also unlikely that the present low-gradient upland valleys formed entirely by glacial incision of steeper fluvial valleys (c.f. Brocklehurst and Whipple, 2002) because the valley heads terminate at uneroded remnants of the unconformity. Only headward erosion of low-gradient glaciated valleys by cirque retreat could maintain this geometry at the range crest (Fig. 6). To estimate the

total amount of cirque retreat and valley incision requires additional knowledge of the divide position that developed by range-scale folding and fluvial incision prior to glaciation. A tentative reconstruction of the original divide position across the easternmost four glaciated catchments indicates between 0.9 and 4.4 km of cirque retreat with only 0.4 to 1.3 km of valley incision (Fig. 4). Further extrapolation of the pre-glaciation divide suggests that >10 km cirque retreat dominates erosion of north-facing valleys.

Evidence for substantial headward expansion of catchments via cirque retreat in the Kyrgyz Range, the Sierra Nevada (Brocklehurst and Whipple, 2002), and potentially elsewhere (Olyphant, 1981) compels a closer examination of the resulting valley form. The immediate cause of cirque retreat is the collapse of steep headwalls at the expense of adjacent low-relief uplands. Processes that sap the cirque walls at the head of the glacier ultimately determine the retreat rate. Because the ratio of valley length to valley incision (0.3–0.4) in the headwaters of north-facing catchments is 2 to 3 times less than the slope of adjacent cirque headwalls (0.8 ± 0.1), sapping by valley incision alone is unlikely to cause the observed retreat. Rather, erosion localized at the base of cirque headwalls is required to propagate cirque retreat across the range at a rate 2 to 3 times greater than the glacial valley incision rate. Incision maxima developed at the heads of south-facing glaciated valleys (Fig. 4) are consistent with a localized sapping process at cirque headwalls.

Because cirque headwalls form within the glacial accumulation zone, modeling cirque erosion via ice-flux based rules (Hallet, 1979, 1996) predicts in greater downstream valley incision than erosion of the cirque floor: a prediction incompatible with observations from the Kyrgyz Range. This may be reconciled if subglacial water pressure fluctuations within cirques locally enhance erosion (Hooke, 1991), or if development of glacial bedforms, such as terminal moraines and overdeepenings, restricts pressure fluctuations and erosion down-glacier (Alley et al., 2003). It is also possible that the integrated residence time of vestigial cirque glaciers under average Quaternary conditions (Porter, 1989) has been sufficient to tip the balance of erosion in favor of cirque incision and consequent headward retreat. Such erosion is consistent with preferred erosion of north-facing catchments, where shading of glacier surfaces lowers the local ELA by ~200 m.

Conclusion

Analysis of the configuration and gradient of glacial valleys in the eastern Kyrgyz Range indicates that cirque retreat dominates initial glacial erosion. This erosion is quantified in the context of a progressively tilted pre-Cenozoic unconformity that is exhumed as a geomorphic surface. This cirque retreat may be incompatible with existing ice-flux-based glacial erosion rules, and highlights a need to understand erosional processes localized within cirques in order to predict alpine landscape evolution. Cirque retreat can effectively bevel across an elevated alpine plateau and keep pace with moderate rock uplift rates, as documented here for the Kyrgyz Range where retreat rates are at least 2 to 3 times greater than the accompanying valley incision rate. Although cirque retreat may not be as significant in all alpine settings (White, 1970), results from the Kyrgyz Range support the contention that glacial valley incision combined with cirque retreat into interfluvies may be a viable mechanism whereby glaciers simultaneously erode at high rates and limit alpine relief.

Figures

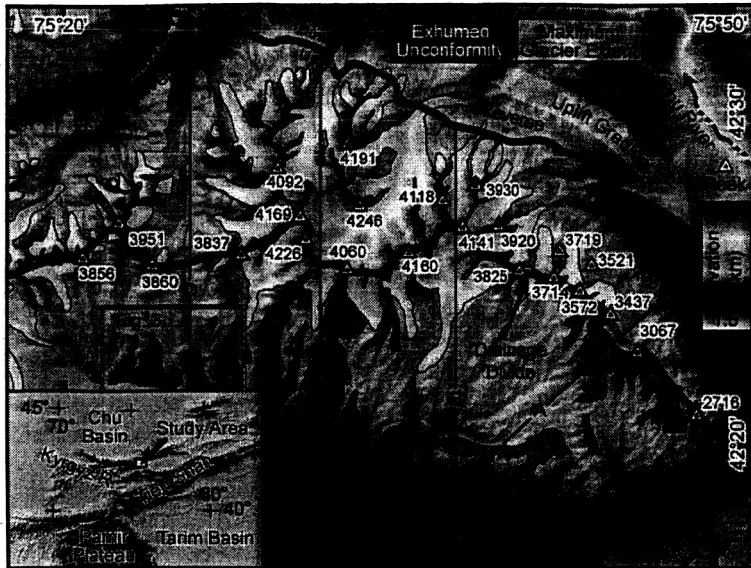


Figure 1. Exhumed pre-Cenozoic unconformity and maximum glacial extent in the eastern Kyrgyz Range. Present-day drainage divide shown as line of peaks (elevations in meters) connected by heavy gray solid line. A-D are center lines of swath profiles in Fig. 2. Inset: shaded relief map of central Asia with Kyrgyz Range crest as hatched line.

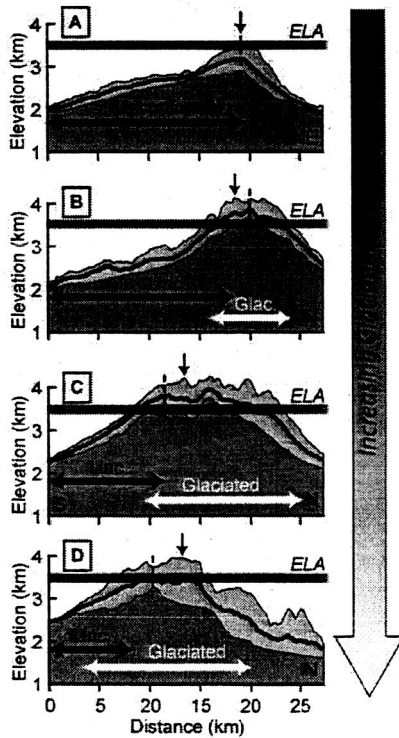


Figure 2. Topographic swath profiles across the easternmost Kyrgyz Range. Each profile samples topography from a 5-km-wide swath centered on profile lines shown on Figure 1. Light gray band depicts range of minimum and maximum topography, with mean values shown as thicker central line. Horizontal black arrow depicts extent of geomorphic surfaces formed by exhumed remnants of the pre-Cenozoic unconformity. ELA is last glacial maximum equilibrium-line altitude. White arrow is extent of last maximum glaciation. Glaciated areas correspond to areas of higher relief and erosional removal of the pre-Cenozoic unconformity at the range crest. Extent of glaciation is inversely proportional to northward position of drainage divide, illustrated by vertical dashed lines. Highest elevation of the range crest shown by downward arrows.

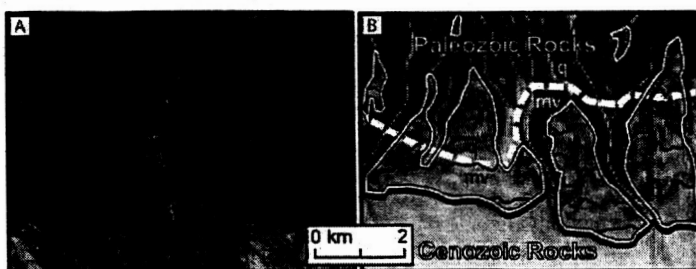


Figure 3. A. ASTER scene of geomorphic surfaces formed by exhumed pre-Cenozoic unconformity on south slope of the Kyrgyz Range. Surfaces are visible as medium albedo with intricate dendritic stream network. B. Interpreted slope map of area shown in A. Steeper slopes (darker gray) correspond to valley sides. White solid lines outline surface remnants mapped from analysis of the SRTM topography, ASTER, and Corona imagery (not shown). Elevation contours at 100-m intervals (black lines) show minimal local relief formed by incision of geomorphic surfaces. White dashed line shows folded Paleozoic contact (truncated by the unconformity) between metavolcanic rocks (mv) and quartzite (q).

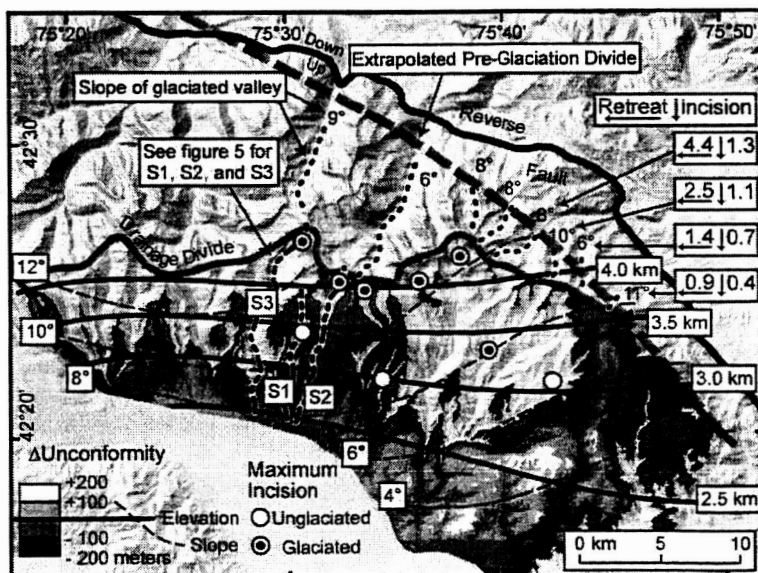


Figure 4. Contours of reconstructed pre-Cenozoic unconformity elevation (solid lines) and slope (dashed lines) overlain on a shaded relief image of the Eastern Kyrgyz Range derived from SRTM topography. Δ Unconformity depicts elevations within 100 m and 200 m from modeled unconformity and compares well with its mapped exhumed remnants on Fig. 1. Dotted lines show gradients of north-facing glacial valley floors. Pre-glaciation divide extrapolated along front of prominent faceted spur ridges that separate glaciated valleys.

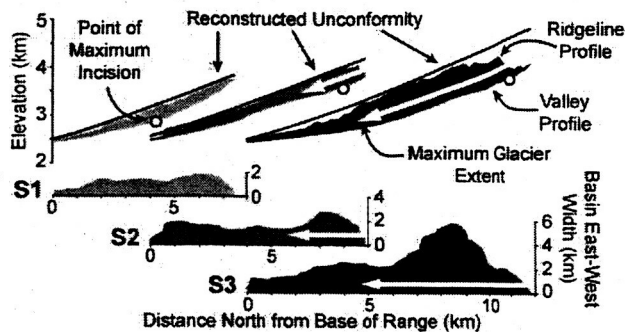


Figure 5. Valley profiles, incision beneath the reconstructed unconformity, and catchment width from three adjacent south-facing streams with varying amounts of glaciation. See Fig. 4 for catchment locations. In the absence of glaciation, incised valleys (S1) are shaped like half-pipes with uniform width. Glacial erosion corresponds to incision maxima at cirque floors and widening of catchments in the zone of ice accumulation, supporting valley expansion via cirque retreat.



Figure 6. Landscape evolution of the eastern Kyrgyz Range with progressive rock uplift. Compare to Figs. 2a through 2c. Light and dark gray represent ridgeline and valley elevation, respectively. Dashed line shows extrapolation of folded unconformity surface over north slope of range. 1. Range form prior to glacial erosion with divide controlled by fluvial erosion and range-scale structural fold axis. 2. Initial glacial erosion of north-facing valley causes southward divide migration relative to fold axis. Unconformity surface is preserved on south-facing slope at range crest. 3. Further range uplift accompanied by additional cirque retreat and expansion of north-facing valley. Note peak of northern ridgeline is higher than unconformity preserved at the drainage divide.

Acknowledgments

This research was supported by NASA Shuttle Radar Topography Mission science program. We thank K. Ye. Abdrakhmatov for logistical support in Kyrgyzstan and K. Davis, M. Jakob, R. Heermance, and B. Bookhagen for assistance in the field.

References

- Alley, R.B., Lawson, A.C., Larson, G.J., Evenson, E.B., and Baker, G.S., 2003, Stabilizing feedbacks in glacier-bed erosion: *Nature*, v. 424, p. 758-760.
- Brocklehurst, S., and Whipple, K.X., 2002, Glacial erosion and relief production in the Eastern Sierra Nevada, California: *Geomorphology*, v. 42, p. 1-24.
- Broecker, W.S., and Denton, G.H., 1990, The role of ocean-atmosphere reorganizations in glacial cycles: *Quaternary Science Reviews*, v. 9, p. 305-341.
- Brown, E.T., Stallard, R.F., Larsen, M.C., Raisbeck, G.M., and Yiou, F., 1995, Denudation rates determined from the accumulation of in situ-produced ^{10}Be in the Luquillo experimental forest, Puerto Rico: *Earth and Planetary Science Letters*, v. 129, p. 193-202.
- Brozovic, N., Burbank, D.R., and Meigs, A.J., 1997, Climatic limits on landscape development in the northwestern Himalaya: *Science*, v. 276, p. 571-574.
- Bullen, M.E., Burbank, D.W., and Garver, J.I., 2003, Building the northern Tien Shan: integrated thermal, structural, and topographic constraints: *Journal of Geology*, v. 111, p. 149-165.
- Bullen, M.E., Burbank, D.W., Garver, J.I., and Abdurakmatov, K.Y., 2001, Late Cenozoic tectonic evolution of the northwestern Tien Shan: New age estimates for the initiation of mountain building: *Geological Society of America Bulletin*, v. 113, p. 1544-1559.
- Burbank, D.W., McLean, I.J.K., Bullen, M.E., Abdurakmatov, K.Y., and Miller, M.G., 1999, Partitioning of intermontane basins by thrust-related folding, Tien Shan, Kyrgyzstan: *Basin Research*, v. 11, p. 75-92.

- Chediya, O.K., 1986, Morphostructure and Neo-tectonics of the Tien Shan: Frunze, Academia Nauk Kyrgyz CCP.
- Federici, P.R., and Spagnolo, M., 2004, Morphometric analysis on the size, shape, and areal distribution of glacial cirques in the maritime Alps (Western French-Italian Alps): *Geografiska Annaler*, v. 86, p. 235-248.
- Hallet, B., 1979, A theoretical model of glacial abrasion: *Journal of Glaciology*, v. 23, p. 39-50.
- , 1996, Glacial quarrying: a simple theoretical model: *Annals of Glaciology*, v. 22, p. 1-8.
- Harbor, J.M., 1992, Numerical modeling of the development of U-shaped valleys by glacial erosion: *Geological Society of America Bulletin*, v. 104, p. 1364-1375.
- Hooke, R.L., 1991, Positive feedbacks associated with erosion of glacial cirques and overdeepenings: *Geological Society of America Bulletin*, v. 103, p. 1104-1108.
- Kirkbride, M., and Matthews, D., 1997, The role of fluvial and glacial erosion in landscape evolution: The Ben Ohau Range, New Zealand: *Earth Surface Processes and Landforms*, v. 22, p. 317-327.
- Molnar, P., and England, P., 1990, Late Cenozoic uplift of mountain ranges: chicken or egg? *Nature*, v. 346, p. 29-34.
- Montgomery, D.R., 2002, Valley formation by fluvial and glacial erosion: *Geology*, v. 30, p. 1047-1050.
- Montgomery, D.R., Balco, G., and Willett, S.D., 2001, Climate, tectonics, and the morphology of the Andes: *Geology*, v. 29, p. 579-582.
- Olyphant, Greg A., 1981, Allometry of cirque evolution: *Geological Society of America Bulletin*, v. 92, p. 679-685.
- Porter, S.C., 1989, Some geological implications of average Quaternary glacial conditions: *Quaternary Research*, v. 32, p. 245-261.
- Riebe, C.S., Kirchner, J.W., and Finkel, R.C., 2004, Erosional and climatic effects on long-term chemical weathering rates in granitic landscapes spanning diverse climate regimes: *Earth and Planetary Science Letters*, v. in press.
- Riebe, C.S., Kirchner, J.W., Granger, D.E., and Finkel, R.C., 2001, Strong tectonic and weak climatic control of long-term chemical weathering rates: *Geology*, v. 29, p. 511-514.
- Shakleton, N.J., and Opdyke, N.D., 1973, Oxygen isotope and paleomagnetic stratigraphy of equatorial Pacific core V28-238: Oxygen isotope temperatures and ice volumes on a 10^5 and 10^6 year scale: *Quaternary Research*, v. 3, p. 39-55.
- Small, E.E., and Anderson, R.S., 1998, Pleistocene relief production in the Laramide mountain ranges, western United States: *Geology*, v. 26, p. 123-126.
- Spotila, J.A., Buscher, J.T., Meigs, A.J., and Reiners, P.W., 2004, Long-term glacial erosion of active mountain belts: Example of the Chugach-St Elias Range, Alaska: *Geology*, v. 32, p. 501-504.
- Vance, D., Bickle, M., Ivy-Ochs, S., and Kubik, P.W., 2003, Erosion and exhumation in the Himalaya from cosmogenic isotope inventories of river sediments: *Earth and Planetary Science Letters*, v. 206, p. 273-288.
- White, W.A., 1970, Erosion of cirques: *Journal of Geology*, v. 78, p. 123-126.

Effects of Bedrock Landsliding on Cosmogenically Determined Erosion Rates

Nathan Niemi^{a*}, Mike Oskin^b, Douglas Burbank^{a†} and Arjun Heimsath^c

^aInstitute for Crustal Studies, University of California, Santa Barbara, CA 93106 USA

^bDepartment of Geological Sciences, University of North Carolina, Chapel Hill, NC 27599 USA

^cDepartment of Earth Sciences, Dartmouth College, Hanover, NH, 03755 USA

The successful quantification of long-term erosion rates underpins our understanding of landscape formation, the topographic evolution of mountain ranges, and the mass balance within active orogens. The measurement of in situ-produced cosmogenic radionuclides (CRNs) in fluvial and alluvial sediments is perhaps the method with the greatest ability to provide such long-term erosion rates. In active orogens, however, deep-seated bedrock landsliding is an important erosional process, the effect of which on CRN-derived erosion rates is largely unquantified. We present a numerical simulation of cosmogenic nuclide production and distribution in landslide-dominated catchments to address the effect of bedrock landsliding on cosmogenic erosion rates in actively eroding landscapes. Results of the simulation indicate that the temporal stability of erosion rates determined from CRN concentrations in sediment decreases with increased ratios of landsliding to sediment detachment rates within a given catchment area, and that larger catchment areas must be sampled with increased frequency of landsliding in order to accurately evaluate long-term erosion rates. In addition, results of this simulation suggest that sediment sampling for CRNs is the appropriate method for determining long-term erosion rates in regions dominated by mass-wasting processes, while bedrock surface sampling for CRNs is generally an ineffective means of determining long-term erosion rates. Response times of CRN concentrations to changes in erosion rate indicate that climatically driven cycles of erosion may be detected relatively quickly after such changes occur, but that complete equilibration of CRN concentrations to new erosional conditions may take tens of thousands of years. Simulation results of CRN erosion rates are compared with a new, rich dataset of CRN concentrations from the Nepalese Himalaya, supporting conclusions drawn from the simulation.

1. Introduction

The successful quantification of long-term erosion rates underpins our understanding of landscape formation, the topographic evolution of mountain ranges, and the mass balance within active orogens [1]. Observed changes in long-term erosion rates are often considered proxies for changes in the climatic or tectonic boundary conditions that control landscape evolution. As the importance of long-term erosion rates to unraveling significant geomorphic and tectonic problems has become clear, a widely applicable means of measuring long-term surface denudation rates has been sought. The measurement of in situ-produced cosmogenic radionuclides (CRNs) in fluvial and alluvial sediments has been shown to yield spatially averaged erosion rates, and has become perhaps

the method with the greatest applicability in measuring erosion rates over 10^3 – 10^5 years and across a wide variety of landscapes and erosional processes [2–6]. Most existing studies that utilize CRN-derived erosion rates have focused on regions with fairly spatially and temporally homogeneous erosion rates. Here we present a simulation to explore the effects of bedrock landsliding on cosmogenic erosion rates, and potential for exploiting cosmogenic nuclides to measure erosion rates in rapidly eroding, active orogens.

Large bedrock landslides incise to depths greater than one or more attenuation lengths of cosmic rays, thus mobilizing sediments with little or no cosmogenic nuclide abundance (Fig. 1). For example, based on empirical relationships of landslide depth to area [7], a landslide with a radius of just 10 meters will incise to ~ 100 cm, below one attenuation depth for spallogenic nuclide production. An extraordinarily large slide may incise to a maximum depth of several tens of meters, below one attenuation depth for

*Also at: Division of Geological and Planetary Sciences, California Institute of Technology, Pasadena, CA 91125 USA.

†Also at: Department of Geological Sciences, University of California, Santa Barbara, CA 93106 USA.

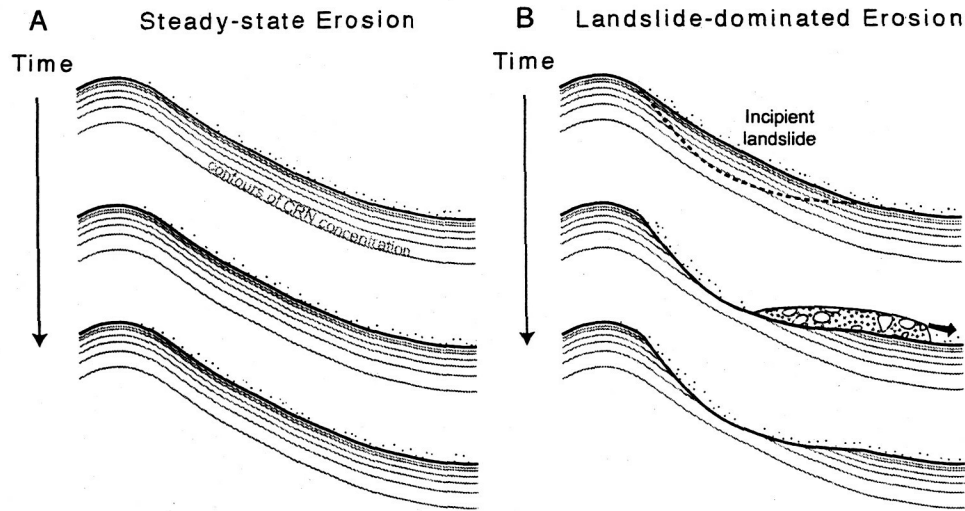


Figure 1. Cartoon showing the effects of landslides on surface cosmogenic nuclide concentrations. A) Homogeneous CRN surface concentration and sediment volume and concentration during steady-state erosion. B) Heterogeneous surface CRN concentration and heterogeneous sediment volume and CRN concentration during landslide-dominated erosion.

muogenic nuclide production. In catchments where deep landslides have recently occurred, the addition of nuclide-poor landslide detritus to the fluvial system will dilute the CRN concentration in the fluvial sediment, yielding apparently higher erosion rates. For example, samples from low-order fluvial catchments in the Nepalese Himalaya yield 'erosion rates' determined from cosmogenic nuclides that range from 0.01 to 0.5 mm/yr, even along the same ridge crest (Heimsath, in prep.). Similar results are reported from the San Bernardino Mountains in southern California, where 'erosion rates' along a landslide-dominated escarpment vary from < 0.3 to > 2.7 mm/yr, while rates from an adjacent region dominated by sediment detachment are on the order of hundredths of mm/yr [8]. Whereas such variability may be expected for data sets that are focused on small, steep catchments in actively deforming mountain belts, it does not explain how in situ-produced CRNs may be utilized to understand the rates of erosion in regions affected by both sediment detachment and landsliding processes.

Here we address the effects of bedrock landsliding on CRN-derived erosion rates from bedrock and

fluvial samples in an attempt to answer several basic questions: As the rate of landsliding increases, how are CRN concentrations in fluvial sediment affected? Can reliable CRN erosion rates be derived from fluvial sediment or bedrock samples when landsliding is the dominant erosional process? Over what spatial scales do fluvial systems integrate the effects of landsliding? What timescales are required for CRN concentrations to respond to changes in erosion rates? We present the results of a numerical simulation of cosmogenic nuclide production and erosional removal in landslide-dominated catchments to assess these questions. A series of simulations with varying sediment detachment and landslide erosion rates are used to create statistical populations of CRN-derived erosion rates for both 'sediment' and 'bedrock' samples for a theoretical landscape. Finally, simulated distributions of CRN-derived ages are compared to a new, rich data set of CRN-derived erosion rates from the Nepalese Himalaya.

2. Numerical Simulation

The numerical simulation is based on actual digital elevation data, and simulates the production of cosmogenic nuclides at each model cell, the removal of material through sediment detachment, the removal of material by landsliding, and the radioactive decay of cosmogenic nuclides. A Geographic Information System (GIS; in this case ArcInfo) is used for the backbone of the simulation. Model initialization, data assimilation, and data output are all controlled through the GIS using Arc Macro Language (AML). Computationally intensive portions of the model are passed from the GIS to customized Perl modules for computational efficiency. The three main functionalities of the simulation are described in greater detail below.

2.1. Cosmogenic Nuclide Production

Prior to running the landslide simulation model, cosmogenic nuclide production rates must be calculated for each cell in the model. Calculation of these rates begins with a geo-referenced digital elevation model (DEM) of the study area of interest. For each cell in the digital elevation model, cosmogenic production scaling factors are calculated within the GIS based on cell altitude and latitude following [9,10]. Further corrections to cosmogenic production are applied by calculating the topographic shielding at each point in the DEM. For each cell in the DEM, the vertical angle to every other cell is calculated. These values are binned into 5° radial bins, and the maximum vertical angle in each bin is used to approximate the horizon angle for that bin. The topographic shielding factor for each bin is derived from the horizon angle using a published methodology [11]. The altitude, latitude, and topographic shielding factors are combined within the GIS system to produce an output array of cosmogenic production scaling factors. This array is then multiplied by the high-latitude, sea-level production rate of the cosmogenic nuclide of interest to create an array of cosmogenic production rates. In this case, we have chosen to model ^{10}Be and selected a production rate of 5.3 atoms/g/yr [12]. This array of ^{10}Be production rates is preserved for use through the rest of the model run.

2.2. Model Initialization

Model initialization consists of two separate actions: i) preparing the model for data gathering and assimilation and ii) calculating an initial surface cosmogenic nuclide concentration to start the landslide model. The first of these two tasks is the most time-intensive and must be performed separately for each DEM on which this model is run. Using the hydrologic functions available in a GIS, watersheds within the model area are delineated. A variety of first-through highest-order watersheds are selected and saved for later use in data analysis. Additionally, 100 random points are generated across the model space at which to track cosmogenic nuclide concentrations in bedrock and erosional removal of material. After the data gathering initialization steps are complete, an input cosmogenic surface nuclide concentration array must be calculated for input to the landslide portion of the model. We have chosen to input a surface concentration grid that represents the steady-state concentration of ^{10}Be at the sediment detachment rate specified for the model run. The sediment detachment rate is limited by the rate at which rock can be converted to soil or regolith, and is taken to be less than 0.3 mm/yr [13]. The surface concentration (N) is calculated for each point in the model following this equation:

$$N^{10}\text{Be} = \frac{P^{10}\text{Be}}{(\lambda_{10\text{Be}} + E/\Lambda)} (1 - e^{-(\lambda_{10\text{Be}} + E/\Lambda)t}) \quad (1)$$

Where $N^{10}\text{Be}$ and $P^{10}\text{Be}$ are the concentration (atoms/g) and production rate (atoms/g/yr) of ^{10}Be , respectively; $\lambda_{10\text{Be}}$ is the decay constant of ^{10}Be (yr^{-1}); E is the erosion rate (here equivalent to the sediment detachment rate), in $\text{g/cm}^2/\text{yr}$; Λ is the neutron attenuation length in rock, in g/cm^2 ; and t is time (yr). This initial concentration array is saved for input into future model runs.

2.3. Landslide Simulation

The landslide simulation portion of the model takes as input the surface cosmogenic nuclide concentration array calculated in the previous step, and the cosmogenic production rate array calculated in the first model step. This portion of the model is iterated. At the end of each iteration, two arrays are output, a depth array which contains the sum of all sediment removed by erosion, due to both sediment detachment and landsliding, and a surface concentration ar-

ray that contains the surface cosmogenic nuclide concentration at each model cell after erosional removal of material, cosmogenic ingrowth and radioactive decay. The individual steps are detailed below.

2.3.1. Cosmogenic ingrowth and decay

The first step in the iteration of the landslide model is to add cosmogenic nuclide ingrowth for one model time step (t) to the input surface cosmogenic nuclide concentration array. Given, for each cell in the model, an initial surface cosmogenic nuclide concentration, $N_i^{10}\text{Be}$, and a surface cosmogenic nuclide production rate, $P^{10}\text{Be}$, a resultant surface cosmogenic nuclide concentration, $N_r^{10}\text{Be}$, produced by cosmic ray bombardment and removal by radioactive decay can be calculated by:

$$N_r^{10}\text{Be} = (N_i^{10}\text{Be} + P^{10}\text{Be} \cdot t) e^{-\lambda_{10}\text{Be} \cdot t} \quad (2)$$

The new surface concentration, $N_r^{10}\text{Be}$, replaces the initial value in the surface concentration array.

2.3.2. Sediment detachment

For each model run, a sediment detachment rate, E_s , is specified. This rate represents the spatially homogeneous erosional removal of material from the land surface, limited by weathering and soil production processes (e.g. grussification in granitic terranes). For each model time step (t), a depth equal to $E_s \times t$ is removed from the landscape and added to the depth grid. This material is always removed from the upper surface of the topography, and therefore has the highest concentration of CRNs.

2.3.3. Landslides

After removal of material by sediment detachment, the model is populated with landslides. Landslides are assumed to obey a power-law frequency-magnitude relationship [7,14,15]. Based on this assumption, populations of landslides in the model can be derived from four parameters: β , the power-law exponent for landslide frequency-magnitude relationship, A_{min} , the minimum landslide area considered in the model, A_{max} , the maximum landslide area considered in the model, and E_{ls} , the average rate of erosion by landsliding over the model area. Although short-term landslide erosion rates fluctuate due to the episodicity of landslides, the average rate of erosion by landsliding is produced through the power-law frequency-magnitude relationship over time (Fig.

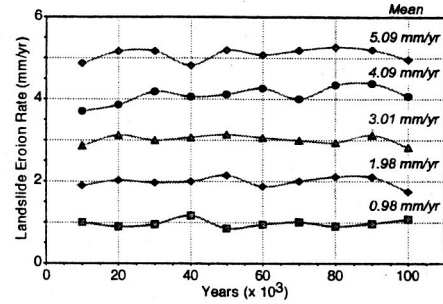


Figure 2. Comparison of output model landslide erosion rates with prescribed landslide erosion rates, averaged over 10,000 year time steps. Mean erosion rates for the 100,000 year model run are shown at the right of the figure. Short term variations in landslide erosion rate are due to random distribution of slide size; long term landslide erosion rates return input erosion rates $\pm 3\%$.

2). Complete derivations of landslide frequency-magnitude distributions in the model space are given in Appendix A. For each model timestep, a landslide distribution is generated, and the landslides are randomly distributed over the model space. The total amount of material removed by landsliding from each model cell during the timestep is then calculated. The total depth of material removed by landsliding is added to the depth of material removed by sediment detachment (see Appendix A).

2.3.4. Surface concentration

Once the depth array is tabulated, the surface cosmogenic nuclide concentration is recalculated to reflect the depth of material removed from each model cell. Assuming, for simplification, a constant rock density (ρ) in the model of 2.65 g/cm^3 , and a cosmogenic ray attenuation length in this rock (Λ) of $150 \text{ cm}^2/\text{g}$, a final surface cosmogenic nuclide concentration at the end of the timestep, $N_f^{10}\text{Be}$, can be calculated for each cell based on the cosmogenic concentration following ingrowth, $N_r^{10}\text{Be}$, above, and the depth of material, D , removed from the cell during the timestep:

$$N_f^{10}\text{Be} = N_r^{10}\text{Be} \cdot e^{-D(\rho/\Lambda)} \quad (3)$$

The value $N_f^{10}\text{Be}$ is stored for each cell in the surface concentration array. At this point, this array is saved

for data extraction, as described in the next section, and then re-opened as the initial surface concentration grid for the next iteration step of the landslide portion of the model.

2.4. Data Extraction

At a user-specified sampling interval, the depth array and surface concentration array are passed back to the GIS, and data are extracted from each array to simulate two potential cosmogenic nuclide sampling methods: surface exposure age dating and stream sediment sampling.

2.4.1. Surface exposure age dating

To simulate the effects of landsliding on surface age exposure dating, at each sampling interval, the depth of material removed from, and the final surface concentration at, each of 100 randomly generated points across the model are recorded. From these data, a volumetric erosion rate (E_v) for this sampling interval is calculated by dividing the depth of material removed (D) by the model time step (t ; recall that D includes both continual removal of rock by sediment detachment and episodic landsliding). Additionally, a cosmogenic erosion rate (E_c) is calculated, for each point using the standard assumption of steady-state erosion [16]:

$$E_c = \frac{\Lambda}{\rho} \left(\frac{P^{10}\text{Be}}{N_f^{10}\text{Be}} - \lambda_{10}\text{Be} \right) \quad (4)$$

Both volumetric and cosmogenic surface-exposure-age erosion rates, along with the depth and surface concentration information, are stored in a database file. Data can be extracted after the completion of the model run to analyze the variation in volumetric and cosmogenic erosion rates at a given point through time, or data from all points can be assimilated and a probability density function (PDF) for either erosion rate can be calculated.

2.4.2. Stream sediment sampling

In addition to surface age exposure dating, cosmogenic nuclide concentrations in stream sediments can be used to estimate average upstream erosion rates. To test the effects of landsliding on such estimates of erosion rates, the model also extracts data by watersheds. At each sampling interval, the following procedures are carried out for each watershed of interest. A volumetric erosion rate (E_v) is calculated by

summing the total depth of material removed from the watershed and dividing it by the watershed area multiplied by the model time step. Second, a cosmogenic erosion rate (E_c) for the watershed is calculated. To calculate this erosion rate, first the concentration of the cosmogenic nuclide of interest in the eroded sediment must be determined. Using the depth array and surface concentration array, the average nuclide concentration in the eroded material at each model cell, $N_D^{10}\text{Be}$, can be calculated as follows:

$$N_D^{10}\text{Be} = N_f^{10}\text{Be} \cdot \Lambda \left(1 - e^{-D(\rho/\Lambda)} \right) \quad (5)$$

The concentration of cosmogenic nuclides in the sediment removed from the watershed, $N_S^{10}\text{Be}$, then, is:

$$N_S^{10}\text{Be} = \sum N_D^{10}\text{Be} / \sum D \quad (6)$$

The erosion rate derived from the cosmogenic nuclide concentration in the material removed from the watershed is then calculated as in Eqn. 4, where $P^{10}\text{Be}$ would represent the watershed-averaged production rate (derived from the GIS-based production calculations), and $N_f^{10}\text{Be}$ would be replaced with $N_S^{10}\text{Be}$. Both volumetric and cosmogenic erosion rates are recorded to database files, and saved for later analysis.

2.4.3. Simplifications and assumptions

It should be noted that the model outlined above makes several simplifying assumptions regarding sediment production and transport. With regards to sediment detachment and transport, this is assumed to occur at a homogeneous rate across the entire model, although in reality the rate at which these processes act on the scale of our model are controlled by local slope and lithology. Landslides are also randomly placed across the landscape, with no considerations for hillslope and aspect. Second, the model contains no provision for sediment storage. All material derived from landsliding is assumed to pass through the model within the timestep in which the landslide occurred (100 years for the models discussed here). Third, the model is intended to produce a population of cosmogenic and volumetric erosion rates for statistical analysis. Erosion and landslides occur through 'time' to produce a variety of surface CRN concentrations that could potentially be sampled; however, this model is not a landscape evolution model. During the course of the model run, the model landscape

Table 1
Statistics for basins tracked in the model.

Basin Order	Number of Basins	Mean Area (km ²)
First	30	0.1
Second	6	0.6
Third	5	2.3
Fourth	4	8.4
Fifth	1	69.0

surface does not evolve, and shielding effects or absolute elevation changes that in reality would alter CRN production rates are not considered. Finally, the role of muogenic production is not explicitly considered in this simulation. The greater attenuation length of muons would likely have the effect of moderating to some extent the surface nuclide concentration in the wake of small- to moderate-sized landslides, but large landslides, which carry the majority of the erosional load, will incise more deeply than the attenuation depth of muons, and thus would have a negligible effect on the model.

3. Model Results

To examine the model, we simulated the effects of landsliding on cosmogenic nuclide equilibrium, and associated CRN-derived and volumetrically calculated erosion rates for the San Antonio Creek catchment, located in the eastern San Gabriel Mountains of southern California (Fig. 3). It is a small ($\sim 70 \text{ km}^2$), mountainous catchment, selected in part because of the availability of high-quality digital elevation model (DEM) data over the region (30-meter resolution), and in part because a significant amount of work exists describing the geomorphology and neotectonics of the region. Low-temperature thermochronologic data indicate that the eastern San Gabriel Mountains are being exhumed at a rate of $\sim 0.3 - 1 \text{ mm/yr}$ [17–19], while geomorphic and geologic studies indicate that landsliding is a prevalent mechanism of erosion in this watershed [20,15]. In fact, both a landslide frequency-magnitude exponential scaling factor (β) and a long-term average erosion rate have been determined for this region [15]. Interestingly, in the San

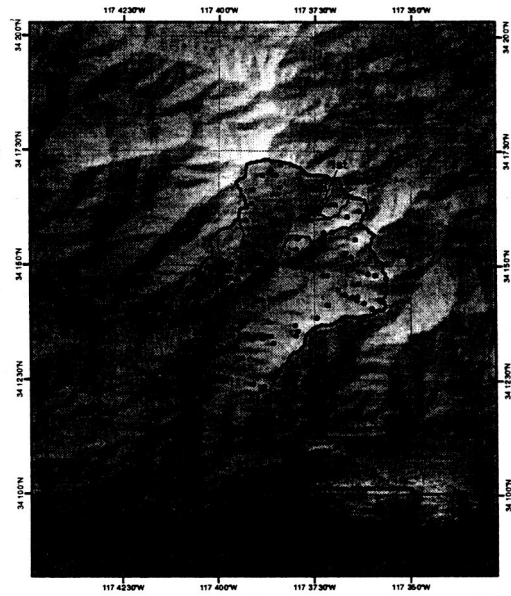


Figure 3. Shaded relief map of the San Antonio Creek watershed, San Gabriel Mountains, California. The full watershed is outlined with a heavy black line, while representative smaller order watersheds are indicated with a lighter black line. Random 'bedrock' sampling points (discussed in the text) are shown as black dots.

Gabriel Mountains, $\beta = 1.1$, similar to results from the Southern Alps of New Zealand [7]. When β is less than 1.5, large, but infrequent landslides dominate the overall sediment flux from a catchment. As such, this watershed potentially provides a natural laboratory to study the effects of landsliding on CRN-derived erosion rates, and for comparison with and calibration of the numerical model.

Within the San Gabriel Mountains, San Antonio Creek is a fifth-order stream. The San Antonio Creek watershed was divided into 46 sub-basins that were tracked as part of this simulation, from which modeled sediment-derived CRN erosion rates were calculated (examples shown in Fig. 3; basin statistics are listed in Table 1). In addition to the sub-basins, 100 points were randomly distributed across the model space to serve as simulated bedrock CRN sampling localities (Fig. 3). For San Antonio Creek, sedi-

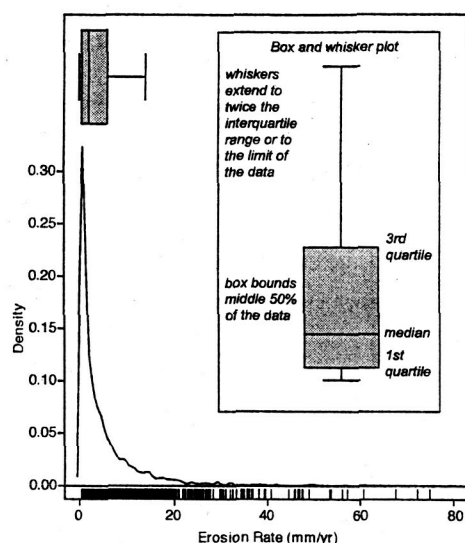


Figure 4. Example of a box-and-whisker plot to graphically display the statistical distribution of a non-Gaussian data set. A probability density function (PDF) and boxplot are shown for actual model results of cosmogenic erosion rates from first-order basins with a sediment detachment rate of 0.1 mm/yr and a total erosion rate of 10 mm/yr. The distribution of erosion rates is plotted across the bottom of the graph as a series of vertical black hash marks.

ment detachment rates of 0.01, 0.1 and 0.3 mm/yr were selected, spanning the range of observed sediment detachment rates in the Transverse Ranges [8] to the most rapid known rates of rock-to-regolith conversion [13]. For each of the three sediment detachment rates, simulations of total erosion rates of 1, 5, and 10 mm/yr were run. The rate of erosion by landsliding in each simulation run is the difference between the total erosion rate and the sediment detachment rate. Once the simulation was equilibrated to the imposed erosion rate, the simulation ran for 100,000 yrs in 100 yr timesteps. Simulated cosmogenic nuclide concentrations were sampled from the 46 tracked catchments and the 100 bedrock locations every 1000 years, yielding 100 data points per analysis element (either catchment or bedrock location).

Results from the simulation are summarized and displayed as a box-and-whisker plot. Such a plot al-

lows a fairly straight-forward visual presentation of the statistical distribution of a data set, and is a valuable graphical method to compare the distribution of two separate data sets (Fig. 4).

3.1. Simulated sediment erosion rates

Catchment-wide erosion rates from the 46 catchments tracked in the model allow comparison of the statistical distributions between CRN-derived and volumetrically averaged erosion rates for each of the nine simulations, and illustrate variations in the statistical distributions within each simulation as a function of catchment order (Fig. 5).

Several conclusions can be drawn from these data. First, with increasing proportion of sediment detachment, the CRN-determined erosion rate at any catchment scale more closely reflects the volumetric erosion rate for any given total combined erosion rate (Fig. 6). This is not unexpected, as sediment detachment is modeled as a uniformly continuous process in the simulation, such that increased ratios of sediment detachment-to-landsliding will result in a greater contribution from a steady-state process to the overall erosional volume. (It is worth noting that under this formulation, for any given total erosion rate, an increase in sediment detachment rate results in a decrease in the rate of erosion due to landsliding. This, increasing the rate of sediment detachment CRN-derived erosion rates that are closer to the volumetric erosion rates, but further from the total erosion rate due the reduction in frequency of landslides; Fig. 6). Additionally, the data emphasize that the observed magnitude-frequency relationships of landslides skew volumetric erosion towards the larger, more infrequent, landslides [14,15]. This is reflected in all nine simulations, where the median 50% of the CRN-derived and volumetric erosion rates generally fall below the total imposed erosion rate in the simulation. The outer statistical bounds of the CRN-derived and volumetric erosion rates are substantially higher than the imposed erosion rates, reflecting the the infrequency, but importance, of these large events in controlling erosion rates in landslide dominated catchments.

The damping and averaging effect of erosion rates derived from CRNs in sediment are also illustrated in the statistical spread of volumetric- versus CRN-derived erosion rates at all catchment scales, sediment

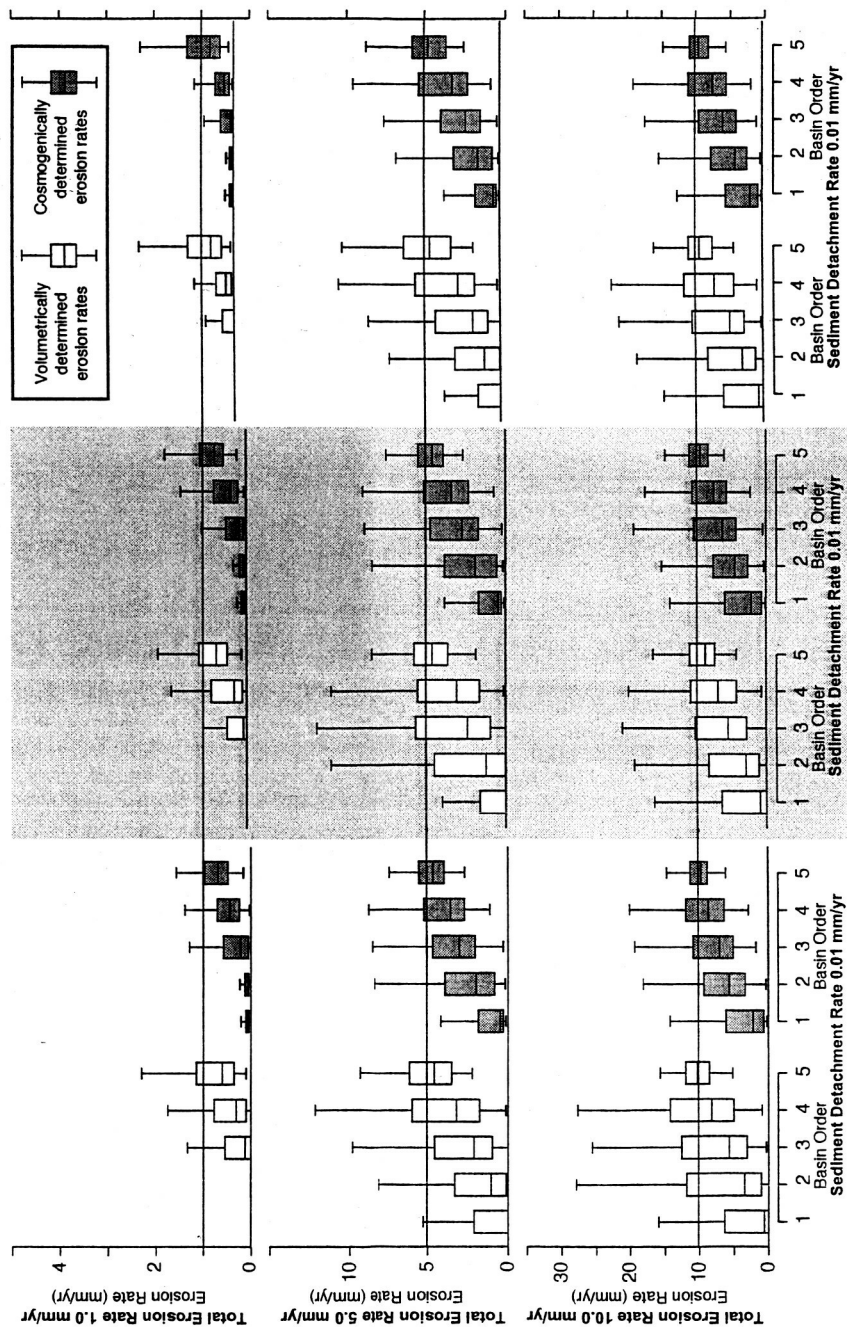


Figure 5: Box-and-whisker plots of CRN-derived erosion rates and volumetric erosion rates for nine separate simulations with three combinations of sediment detachment and total erosion rates. Upper solid line on each graph indicates total erosion rate; lower solid line indicates sediment detachment rate. See text for detailed discussion.

detachment rates, and landslide rates, where the distribution of CRN-derived erosion rates is tighter than contemporaneous volumetric erosion rates. This effect is particularly notable at small to moderate catchment scales in regions with low rates of erosion by landsliding. In particular, at 1 mm/yr total erosion rate, the CRN-derived rates have a 50% smaller distribution than the volumetric erosion rates.

The effect of spatial averaging on the spread of volumetric- and CRN-derived erosion rates is also highlighted in our results (Fig. 5). The statistical spread of both volumetric erosion rates increases with increasing catchment size, presumably related to the increased likelihood of experiencing a large mass-wasting at greater catchment area, until a threshold is reached, at which point the catchment becomes large enough to adequately average large landsliding events and areas unaffected by mass wasting, and the spread of the data drops significantly. This spatial scale in our simulations appears to occur between fourth- and fifth-order catchments (a jump from $\sim 8 \text{ km}^2$ to $\sim 70 \text{ km}^2$). The exception to this rule is at low total erosion rates, where landslides appear to occur infrequently enough at all catchment scales to never significantly increase the statistical distribution of erosion rates at third- through fifth-order catchments.

Finally, given the damping and spatial averaging affects described above, it is heartening to note that the median 50% of observations are more or less consistent between volumetric and CRN-derived erosion rates (Fig. 5). At small catchment scales, CRN-derived rates are typically higher than volumetric rates (this is particularly clear at low total erosion rates), but converge at larger catchment scales (Fig. 6). The catchment size at which this convergence occurs varies, and decreases with increased rates of erosion. As a general rule of thumb, however, it would appear that CRN-derived rates of erosion from sediments are statistically representative of volumetric rates in our numerical simulation at third-, or at most, fourth-order catchment scales. This observation indicates that CRN-derived erosion rates from sediments in landslide-dominated catchments may in fact be useful for looking at basin-wide erosion. Even modest-scale drainages, such as San Antonio Creek, have several fourth-order catchments. Measuring CRN-derived erosion rates from each of these catchments should allow the identification of

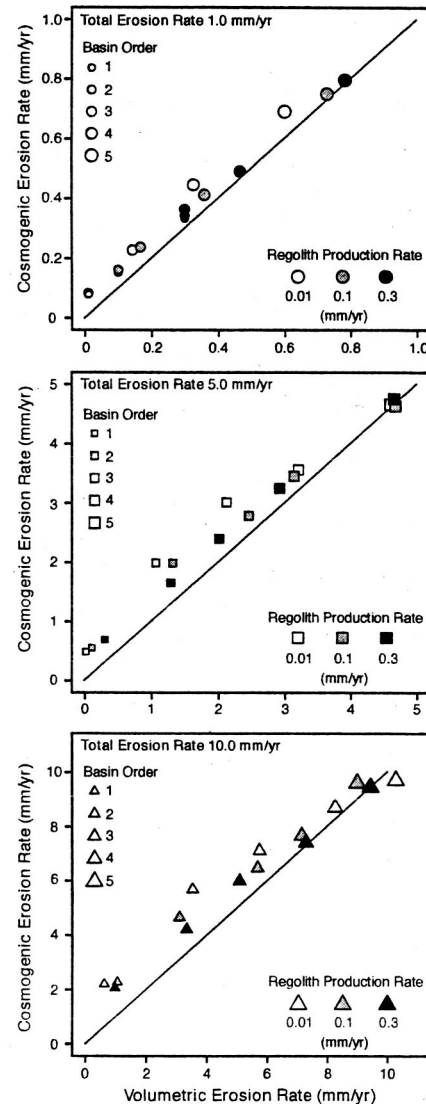


Figure 6. Scatter plots of median cosmogenic versus median volumetric erosion rates for (from top to bottom) total erosion rates of 1, 5, and 10 mm/yr. All plots indicate that cosmogenic erosion rates are higher than volumetric erosion rates, and illustrate the convergence of the two rates with increasing sediment detachment rate.

outlying rates that may be due to recent mass wasting events. Such outlier rates would approximate the recent volumetric erosion rates from the basin (Fig. 5). Nonetheless, even fourth-order catchments are likely to underpredict the overall erosion rate by 20–40%, due to the impact of rare, but unusually large, landslide events.

3.2. Simulated bedrock erosion rates

In addition to tracking the CRN concentration at 46 catchments within the simulation, we also calculated the surface CRN concentration at 100 points randomly distributed throughout the model space, and analyzed such concentrations for erosion rates as though bedrock samples were collected from each of these points (eqn. 4). The statistical distributions of these erosion rates are derived from analysis of 100 random points, sampled 100 times at 1,000 year intervals, over a 100,000 year model run, such that each box-and-whisker in the plot represents the statistical distribution of some 10,000 independently determined erosion rates (Fig. 7).

A first-order observation is that the spread of erosion rates increases with increasing rates of total erosion (and thus, with increasing rates of landsliding). This almost certainly reflects the increased likelihood of any of the randomly sampled points in the model to be affected by landsliding with the increasing frequency of events. A second important observation is that at low rates of total erosion (and landsliding), although sediment detachment encompasses, at most, 30% of total erosion, the median CRN-derived erosion rate is almost identical to the sediment detachment rate. That is, for any given point in the landscape, the likelihood of sampling a point that has been recently enough effected by mass wasting to alter the CRN concentration is virtually negligible. As the total rate of erosion increases, the median erosion rates increases above the background sediment detachment rate, yet fall well below the total erosion rate over the landscape. In contrast to the distribution of sediment-derived CRN erosion rates (Fig. 5), the upper extent of the 'whisker' (3 inter-quartile ranges beyond the median) never exceeds the imposed total erosion rate. Although the CRN-derived erosion rates do not follow a Gaussian distribution, one may draw the analogy that less than 99% of the 'bedrock' samples will fail to accurately reflect the total erosion rate over the

landscape. (The highest actual percentage is 0.25% for a total erosion rate of 10 mm/yr, and a sediment detachment rate of 0.01 mm/yr, where 25 samples out of 10,000 fell within 2 mm/yr of the total erosion rate).

These results suggest that sampling bedrock exposures in basins dominated by mass wasting may provide an upper bound on sediment detachment rates across the basin, but are inadequate as a means to derive overall rates of erosion from the combined effects of sediment detachment and landsliding.

3.3. Response of CRN-derived erosion rates to changes in rates of mass wasting processes

In addition to tracking the CRN concentrations in sediment from catchments, and at individual points, the simulation also calculates the mean CRN concentration across the landscape at each point in the simulation. Whereas the calculation of CRN and volumetric erosion rates is only performed while the simulation is in an erosional 'steady-state' for the imposed landslide and sediment detachment rates, the mean CRN concentration is calculated throughout the model run to gather an estimate of the response time of CRNs in the landscape to changes in erosional boundary conditions (Fig. 8).

These plots record the mean ^{10}Be concentration over the landscape, beginning at the initialization of the model, where the ^{10}Be concentration at each cell in the simulation is analytically solved for the imposed sediment detachment rate and the scaled production factor at each cell. Subsequently, landslides are populated across the model landscape, and the mean concentration of ^{10}Be begins to decrease at a rate controlled by the sediment detachment rate and the total rate of landsliding imposed on the model. After a period when mean ^{10}Be concentration steady-state is achieved during sediment detachment and landsliding, the landslides are eliminated from the simulation, and the mean ^{10}Be concentration in the landscape increases (Fig. 8A).

Tracking of specific points emphasizes the effects of changes in sediment detachment and landsliding rates on the response time of mean ^{10}Be concentration (Fig. 8B). The response time of the landscape to achieve a new equilibrium mean ^{10}Be concentration is a function of both the sediment detachment rate and the landsliding rate. For a given total ero-

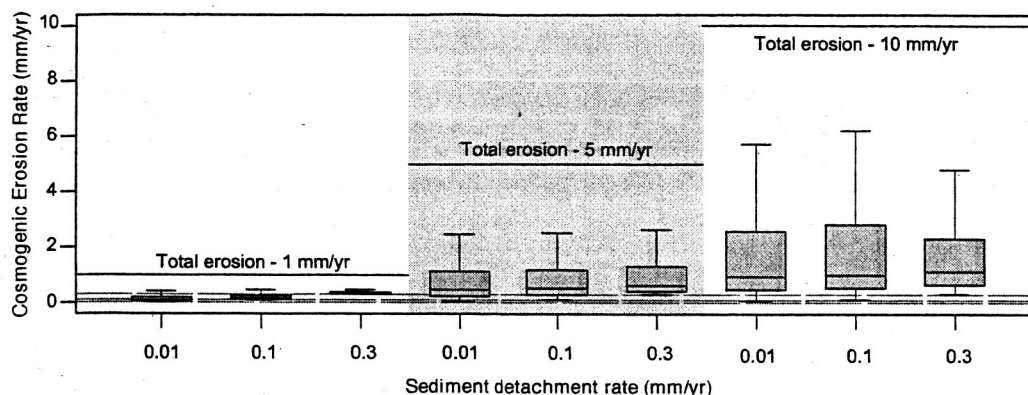


Figure 7. Distribution of cosmogenically determined erosion rates (shaded boxes) from individual sample points for each model run. Total erosion rates for each set of runs are indicated by solid lines; sediment detachment rates are drawn across the lower portion of the graph in dashed lines. As landslide erosion rates increase, the spread and median of cosmogenically derived erosion rates also increase. Median cosmogenically determined erosion rates at these points, however, remain well below total erosion rates for each model run.

sion or sediment detachment rate, the time for ^{10}Be to reach a new equilibrium decreases with an increase in the other rate. Increasing the sediment detachment rate by a factor of ten decreases the time necessary for ^{10}Be to reach a new equilibrium concentration (squares on Fig. 8B); likewise, increasing the rate of landsliding by a factor of 5 causes also yields a decrease in the response time (circles on Fig. 8B). On the other hand, the response time for re-equilibration of mean ^{10}Be concentration at the cessation of landsliding is a function solely of sediment detachment rate. The time necessary for a landscape to recover 95% of its pre-landslide mean ^{10}Be concentration is as little as 2,000 yrs, at sediment detachment rates of 0.3 mm/yr, and as great as 55,000 to 75,000 years at sediment detachment rates of 0.01 mm/yr (triangles on Fig. 8B).

These results indicate that in rapidly eroding landscapes, changes in landsliding rates over relatively short time periods (say a few thousand years or less) may generate transients in CRN concentrations lasting tens of thousands of years. If landsliding is a more prevalent mechanism of erosion under certain climatic regimes (e.g. during interglacial periods; [21,?]), then the response time of mean ^{10}Be concentration to changes in landsliding rate must be consid-

ered when the frequency of these rate changes is of order the ^{10}Be response time of tens of thousands of years.

3.4. Comparison of simulation results of CRN erosion rates to CRN erosion rates from the Nepalese Himalaya

The Khudi River in Nepal, a tributary to the Marsyandi, has been the focus of a multi-disciplinary study of geomorphic and geodynamic coupling in the Himalaya. As part of this study, erosion rates over this catchment have been assessed using a variety of techniques, including long-term erosion rates from low-temperature thermochronometers ($\geq 2\text{--}5$ mm/yr; [22]), and present-day erosion rates from stream-sediment suspended-load determinations (~ 3 mm/yr; E. Gabet, pers. comm.). In addition, ^{10}Be CRN erosion rate determinations were made throughout the catchment, both from bedrock exposures and 0^{th} -order (≤ 0.01 km²) catchments, and from the mouth of the Khudi River where it joins the Marsyandi (Heimsath, in prep.). The measured CRN erosion rates were calculated using the same production rates and scaling factors as in the model, and have an average error of 10%. Here we compare the statistical distribution of 56 ^{10}Be CRN erosion rate determinations from bedrock exposures and 0^{th} -order catch-

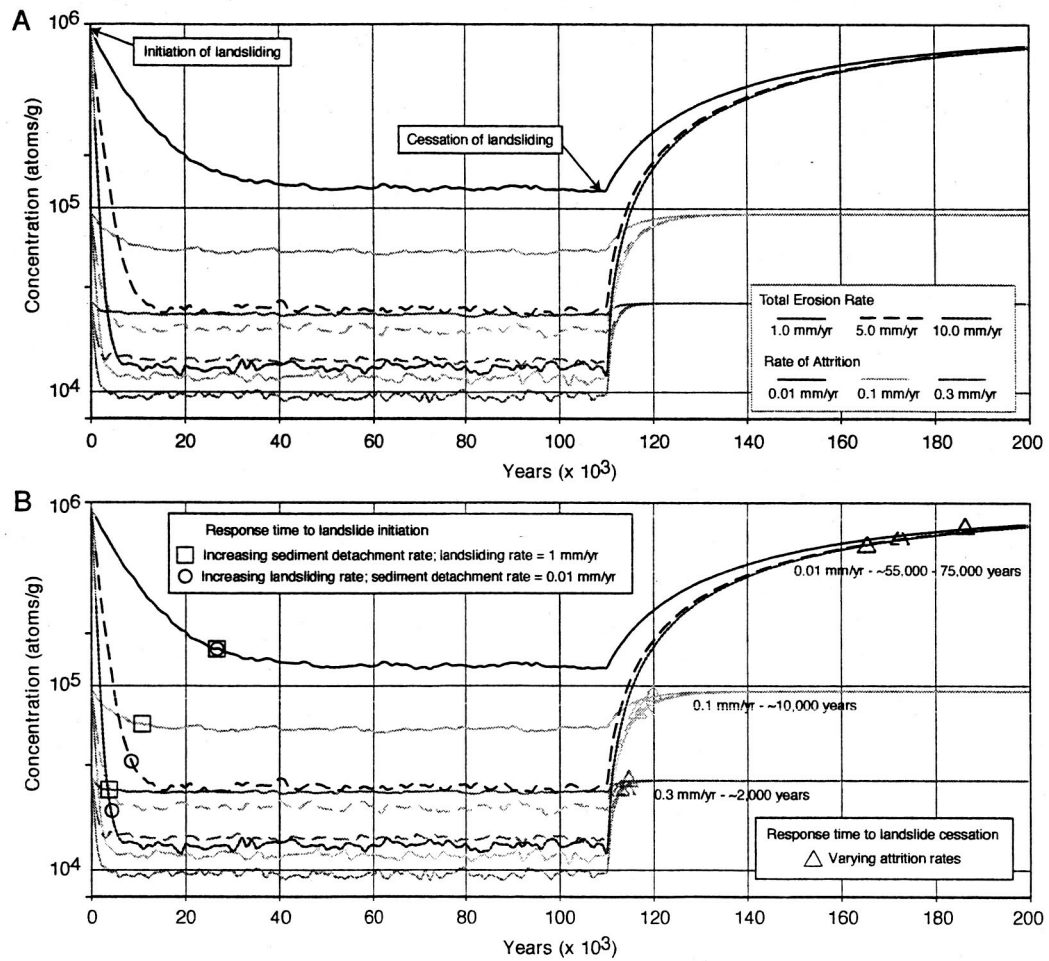


Figure 8. Mean concentration of ^{10}Be across the simulation, showing the effect of initiation and cessation of landslides on ^{10}Be concentration at several different rates of sediment detachment and landsliding. **A)** Mean ^{10}Be concentration through time for all model runs; initiation and cessation of landsliding indicated. **B)** Symbols highlighting variation in response time to changing boundary conditions, see text for discussion.

ments with predicted statistical distributions of CRN erosion rates determined from our simulation. Additionally, we calculate distributions of CRN erosion rates predicted at the mouth of the Khudi River, and compare these with the basin-wide CRN erosion rates determined for the Khudi catchment.

The simulation of landsliding, cosmogenic production, and erosion was performed as described for the theoretical study in the San Antonio Creek watershed, with only a few modifications. First, the highest resolution DEM available for Nepal has roughly 90-m cell spacing, as opposed to the 30-m spacing available for San Antonio Creek. The model cell size was adjusted accordingly, and the smallest landslide populated in the model was also adjusted to have a radius of 90 meters. Second, available erosion rate data from thermochronologic and sediment-load studies were used to establish a range of landsliding rates to input to the model of the Khudi catchment. A sediment detachment rate of 0.15 mm/yr was assumed for the initial model runs, and landsliding rates of 2.85, 3.35, and 3.85 mm/yr (for total erosion rates of 3, 3.5, and 4 mm/yr) were selected. The best-fit run was then re-analyzed with varying sediment detachment rates to derive a statistical distribution of bedrock and small-order catchment CRN erosion rates for comparison with existing CRN data. Finally, the size of the 0th-order catchments is of order the size of the model cell spacing, so these small catchments were treated as points within this model.

3.4.1. Basin-wide CRN erosion rate in the Khudi catchment

The distribution of basin-wide CRN-erosion rates derived from the model were compared with a ¹⁰Be-derived erosion rate measured on sediment deposited at the mouth of the Khudi catchment. The measured CRN erosion rate of 3.4 mm/yr matches the median of the CRN erosion rates for the model run with total erosion rate of 3.5 mm/yr (0.15 mm/yr sediment detachment and 3.35 mm/yr landslides; Fig. 9A). This result supports the theoretical determination that at high landslide erosion rates, the effects of landsliding on CRN erosion rates are spatially averaged over large catchments, and that CRN methods are an effective means of assessing average erosion rates. Further, the median values of each of these three model runs does not overlap the 1st through 3rd quartiles of any

other run (Fig. 9A), indicating that the medians of these model runs statistically differ [23]. The results of this simulation, in concert with the actual CRN erosion rate, allow a determination of the erosion rate in the Khudi catchment of 3 ± 0.5 mm/yr, tightening the constraints on the erosion rate as derived from thermochronologic and sediment-load data.

3.4.2. Bedrock and small-order catchment CRN erosion rates in the Khudi catchment

Using the basin-wide total erosion rate of 3.5 mm/yr, four additional model runs were executed at increasing rates of sediment detachment (0.01, 0.05, 0.10, and 0.15 mm/yr) to compare the simulated distributions of CRN erosion rates with the distribution of CRN erosion rates determined from 56 ¹⁰Be erosion rates from bedrock samples and 0th-order catchments (Heimsath, in prep.; Fig. 9B). In the model space, the same 56 locations that were actually sampled were used to determine a theoretical distribution of bedrock erosion rates. The results of this comparison indicate that, as hypothesized from the theoretical results, sampling bedrock and small area drainage basins for CRN concentrations in regions with significant erosion by bedrock landsliding is not an effective approach to determining basin-wide erosion rates. The data set analyzed in the Khudi drainage is one of the larger CRN erosion rate studies undertaken, yet the number of samples collected, and the percentage of the landscape that they represent, is inadequate to provide a meaningful representation of basin-wide erosional processes. Although thermochronometric, cosmogenic, and sedimentologic techniques all indicate erosion rates in the Khudi of 2–5 mm/yr, the median CRN erosion rate from the Khudi bedrock samples is ~ 0.1 mm/yr, while the median of the simulation runs is ~ 0.25 mm/yr (Fig. 9B). It is also interesting to note that the median erosion rates from the four model runs are very similar, despite an order of magnitude difference in sediment detachment rate among them, and they differ significantly from the median erosion rate determined on the actual bedrock samples. This difference can likely be ascribed to two sources, both due to the fact that the actual bedrock samples from the Khudi catchment almost all came from ridge crests, or small draws that head at ridge crests. The first source of the observed difference is that landslides in the model space are placed ran-

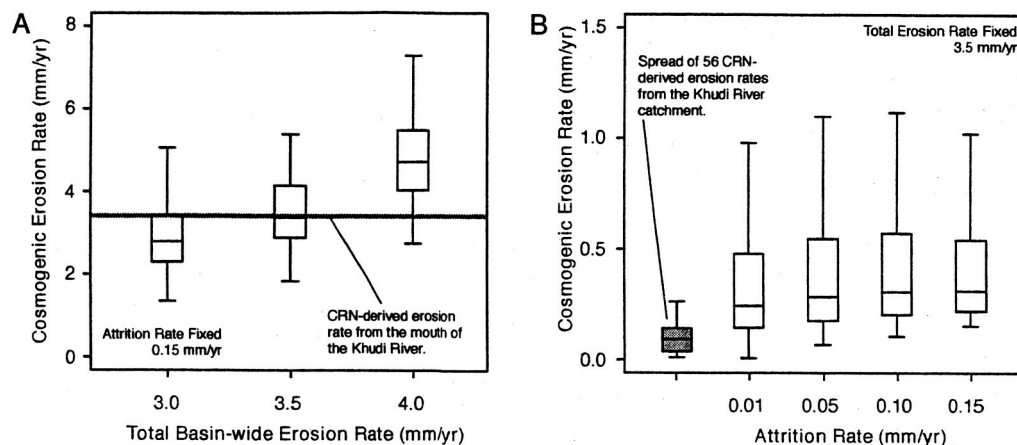


Figure 9. A) Distribution of model basin-wide CRN-derived erosion rates from the mouth of the Khudi drainage for erosion rates of 3.0, 3.5, and 4.0 mm/yr. The thick gray line across the center of the figure is the measured ^{10}Be derived erosion rate of 3.4 mm/yr from the mouth of the Khudi River (A. Heimsath, unpub. data). B) Comparison of simulated distributions of CRN-derived erosion rates from 56 sample locations (white boxes) where actual CRN-erosion rates were measured (gray box; A. Heimsath, unpub. data) for bedrock samples in 0th-order catchments in the Khudi drainage. Median CRN erosion rates for both the simulated data and the actual CRN data are an order of magnitude less than the basin-wide erosion rate (A).

domly, such that a ridge crest is as likely to be affected by landslides as a hillslope. In reality, this is likely to not be the case. Landslide mapping indicates that although landslides are preferentially located in areas of steep slopes near the headwaters of drainage systems, such slides rarely breach the drainage divide and lower the interfluvium (e.g. [24]). Lowering of drainage divides most plausibly occurs during infrequent events when the topographic slope below the ridge crest has been over steepened by repeated landsliding, and is thus this process is likely to be highly undersampled. The second effect is sampling bias. The CRN samples were specifically collected from bedrock outcrops along the crest that were judged to not have been recently affected by landsliding. As such, the spread of CRN ages would be expected to be smaller than a truly random set of ridge crest samples, and the median erosion rate would, as a result, be lower. This difference notwithstanding, the results of this comparison still serve to emphasize the importance of considering the effects of spatial and temporal averaging in collecting material for CRN determinations of erosion rates in actively landsliding re-

gions.

4. Discussion and Conclusions

We have presented a numerical simulation for modeling the production, decay, and distribution of cosmogenic nuclides on a landscape, and their removal through sediment detachment and mass wasting processes. Although this simulation was developed to model the effects of landsliding on CRN-derived erosion rates, the framework of the simulation could be adapted to model any number of factors that effect erosion rates derived from CRNs in sediments, including spatial variations in lithology and mineral content, ice cover, annual snowfall, and recent effects of glaciation. In the past, careful researchers trying to exploit CRNs to obtain erosion rates have commonly restricted their sampling to small, unglaciated catchments with uniform lithologies and slow erosion rates. Variations in CRN production due to topographic shielding, slope, lithology, snow and ice cover, and glacial history have generally been ignored. With the ability to numerically predict the

effects of such variations, studies can be expanded into larger catchments with higher erosion rates, diverse sediment-production processes, and spatial heterogeneities in CRN concentrations and events that can re-set the cosmogenic clock.

Our landsliding model is underpinned by the observed frequency-magnitude relationships of landslides in two mountain ranges. These happen to yield nearly identical exponential scaling factors ($\beta = 1.1$) that imply that large, infrequent landslides dominate the total sediment flux. The observation that implementation of our frequency-magnitude based landsliding module yields volumetric rates that oscillate around the expected value suggests that the model succeeds in mimicking a natural process. This frequency-magnitude relationship and the appropriate scaling factor need to be verified in other mountain ranges before they are routinely applied. In addition, we make the implicit assumption that all of the sediment generated by a landslide is delivered and homogeneously mixed with sediment detachment-derived sediment within a single model time step (100 years). We make no attempt to model sediment storage on hillslopes or within fluvial systems, or to model particle size fractionation between sediment detachment-derived and landslide-derived debris.

Our specific evaluation of the effects of bedrock landsliding on erosion rates derived from CRNs using this simulation yielded several results that have been previously described, particularly that stochastic processes, dominated by large rare events, are difficult to measure using basin-averaging sediment-sampling techniques, because the large, rare events, will often not be represented in the sample population (e.g. [?]). However, our simulations also indicate that the median CRN-determined erosion rates are representative of the volumetric erosion rates derived from the same catchments. This suggests that sampling multiple, similarly sized catchments, even in active, landslide-dominated mountain belts, offers a significant likelihood of yielding several samples with consistent CRN erosion rates. These rates are likely to be representative of the recent erosion within those catchments, although it must be recognized that such results will typically be lower than the long-term average that samples the large, rare events. As long as spatial variations in production can be adequately accounted for, as is done within our model-

ing environment, then larger catchments will always yield a better approximation of long-term erosion rate in landslide-dominated terrains than smaller catchments. Although a specific relationship between the catchment size necessary to spatially average CRN samples and erosion rate is difficult to derive, based on our modeling results a general rule of thumb appears to be

$$A_{avg} = \frac{100}{E} \quad (7)$$

where A_{avg} is the area needed to average the variability in CRN concentration, and E is the estimated erosion rate over the catchment.

Sampling from bedrock outcrops to measure average erosion rates in landslide-dominated catchments, however, is unlikely to be a useful exercise. At the low end of landslide erosion rates, such samples will faithfully yield the sediment detachment rate on the landscape, but at increased rates of landslide erosion, such samples will only yield a very rough upper bound on the sediment detachment rate, and, more likely, will be uninterpretable in the context of the spatially averaged erosion rate over the study area.

Finally, the response time of ^{10}Be concentrations over the landscape to changes in rates of erosional processes is thousands to tens of thousands of years. Regions that have undergone recent changes in rates of erosion may yield CRN-derived erosion rates that reflect some intermediate rate between the previous and current erosion rates during the re-establishment of ^{10}Be equilibrium over the landscape.

Acknowledgements

This work was supported in part by a grant from the Campus-Laboratory Exchange Program of the University of California. Field work in Nepal and analysis of cosmogenic samples were supported by NSF grant EAR-XXXXX. Comments and suggestions from two anonymous reviewers and the editor greatly improved the clarity of this manuscript.

Appendix A

Governing Equations

This Appendix details the derivations of three specific portions of the landslide model, calculating the rate of landsliding, κ , given a mean landslide erosion

rate, E_{ls} ; population of landslides in model space, and determining mean cosmogenic concentration per volume of material removed from the model.

Rate of Landsliding

We assume that landslides follow a power law frequency magnitude distribution [7,14]. For such a distribution, the cumulative frequency of landslides can be written as

$$n_{A \geq A_s} = \kappa (A_s/A_r)^{-\beta} A_r, \quad (A8)$$

where $n_{A \geq A_s}$ is the number of landslides greater than area A_s that occur in a given year, A_r is a specified reference area, κ is the rate of landsliding, and β is the power-law exponent of the frequency-magnitude distribution [7, see eqn. 1]. If A_r is taken to be 1 km^2 , then from Eqn. A8, the total number of landslides per year, n , over the reference area can be written as

$$n_r = \int_{A_{min}}^{A_{max}} \kappa A^{-\beta} dA, \quad (A9)$$

$$= \kappa \left[A^{-\beta} \right]_{A_{min}}^{A_{max}}, \quad (A10)$$

$$= \kappa \left(A_{max}^{-\beta} - A_{min}^{-\beta} \right), \quad (A11)$$

where A_{min} is the area of the smallest landslide to occur in A_r (in the case of the simulation, A_{min} is equal to the model cell size) and A_{max} is the largest slide area, constrained by local topographic relief. Since A_{min} and A_{max} can be constrained either empirically or based on physical characteristics of the model space, and β has been shown to be ~ 1 over a large range of landslide erosion rates [7,14,15], the volume of material removed by landsliding must be controlled by the rate of landsliding, κ . Because we would prefer to prescribe a rate of erosion due to landslides, E_{ls} for the model, we need to solve for κ in terms of E_{ls} . To do this, we start by determining the number of slides, n_{A_s} , of a given area, A_s per year over the reference area, A_r :

$$n_{A_s} = \kappa \beta A_s^{-1-\beta}. \quad (A12)$$

Given this, the volume of erosion in any year due to landslides of area A_s is equal to the number of landslides of area A_s multiplied by the volume of landslides of area A_s ,

$$V_{A_s} = n_{A_s} \cdot V_s \quad (A13)$$

$$= \kappa \beta A_s^{-1-\beta} \cdot V_s. \quad (A14)$$

In this simulation, we have opted to model the landslides with parabolic cross sections and a linear relationship between maximum slide depth and width [25,7]. The scaling between landslide area and depth is defined by a scaling factor, ε , with an empirically determined value of ~ 0.05 [7]. Thus, the depth of the landslide, d , at any radial distance from the landslide center is a function of the maximum slide depth, the radial distance from the landslide center, r , and a constant, C ,

$$d = d_{max} - Cr^2. \quad (A15)$$

We can solve for C at the outer edge of the landslide, r_{max} , where $d = 0$,

$$C = \frac{d_{max}}{r_{max}^2}. \quad (A16)$$

For a slide of a given area A_s , then, the maximum landslide depth, d_{max} and radius, r_{max} , are given by

$$d_{max} = \varepsilon \sqrt{A_s} \quad (A17)$$

and

$$r_{max} = \sqrt{\frac{A_s}{\pi}}. \quad (A18)$$

Substitute these values into Eqn. A16 to solve for C in terms of area, A_s :

$$C = \frac{\varepsilon \sqrt{A_s}}{A_s/\pi} = \frac{\varepsilon \pi}{\sqrt{A_s}} \quad (A19)$$

and substitute Eqns. A17 and A19 into Eqn. A15 to solve for d as a function of A_s ,

$$d = \varepsilon \sqrt{A_s} - \frac{\varepsilon \pi}{\sqrt{A_s}} r^2. \quad (A20)$$

The volume, V_s , of a landslide of area A_s can then be calculated by integrating over cylindrical shells from $r = 0$ to r_{max} ,

$$V_s = 2\pi \int_0^{r_{max}} \varepsilon \sqrt{A_s} - \frac{\varepsilon \pi}{\sqrt{A_s}} r^2 \cdot r dr \quad (A21)$$

$$= 2\pi \varepsilon \left[\frac{\sqrt{A_s}}{2} r^2 - \frac{\pi}{4\sqrt{A_s}} r^4 \right]_0^{\sqrt{A_s/\pi}} \quad (A22)$$

$$= 2\pi \varepsilon \left(\frac{A_s^{3/2}}{2\pi} - \frac{A_s^{3/2}}{4\pi} \right) \quad (A23)$$

$$= \frac{\varepsilon}{2} A_s^{3/2} \quad (A24)$$

Eqn. A24 can be substituted back into Eqn. A14 to yield the volume of material, V_{A_s} , removed from the reference area, A_r per year by slides of area A_s :

$$V_{A_s} = \frac{1}{2} \kappa \varepsilon \beta A_s^{(1/2-\beta)}. \quad (\text{A25})$$

The total volume of erosion per year from reference area A_r , then, is the sum of the erosion due to landslides of all sizes that occur in A_r , from A_{min} to A_{max} ,

$$V_r = \frac{1}{2} \kappa \varepsilon \beta \int_{A_{min}}^{A_{max}} A_{ls}^{(1/2-\beta)} dA \quad (\text{A26})$$

$$= \frac{\kappa \varepsilon \beta}{(3-2\beta)} \left(A_{max}^{(3/2-\beta)} - A_{min}^{(3/2-\beta)} \right). \quad (\text{A27})$$

The total erosion rate per year due to landslides, then, can be determined by dividing the volume of material eroded per year by landslides over A_r by the area of A_r ,

$$E_{ls} = \frac{V_r}{A_r} \quad (\text{A28})$$

and, since we have defined A_r to be a unit area (1 km²),

$$E_{ls} = V_r \quad (\text{A29})$$

Thus, Eqn. A27 can be solved for κ in terms of E_{ls} to yield

$$\kappa = \frac{E_{ls}(3-2\beta)}{\varepsilon \beta \left(A_{max}^{(3/2-\beta)} - A_{min}^{(3/2-\beta)} \right)}. \quad (\text{A30})$$

Substituting Eqn. A30 into Eqn. A11 yields the total number of landslides, n_r , per year over the reference area, A_r in terms of known or prescribed values A_{min} , A_{max} , β , ε , and E_{ls} :

$$n_r = \frac{E_{ls}(3-2\beta) \left(A_{max}^{-\beta} - A_{min}^{-\beta} \right)}{\varepsilon \beta \left(A_{max}^{(3/2-\beta)} - A_{min}^{(3/2-\beta)} \right)} \quad (\text{A31})$$

The total number of landslides, n_{ls} , then, in the simulation for a given time step, t , over the entire simulation is

$$n_{ls} = t \times n_r \times \frac{A_{sim}}{A_r} \quad (\text{A32})$$

where A_{sim} is the area, in km², of the simulation.

Landslide Population and Distribution

With the number of landslides per time step determined, the simulation is populated. The position each landslide is specified by a randomly generated x,y coordinate pair. The size of a given landslide is derived from the landslide frequency-magnitude relationship (Eqn. A8). The probability of a landslide with area A_s occurring is

$$P_{A_s} = \kappa A_s^{-\beta} \quad (\text{A33})$$

therefore, randomly generated numbers mapped linearly onto the range $P_{A_{min}}$ to $P_{A_{max}}$ can be used to create a population of n_{ls} landslides that fit the frequency-magnitude distribution $\kappa A^{-\beta}$.

Cosmogenic Nuclide Concentration in Eroded Material

For each model step, the total depth of material removed from a given cell, D , is the sum of material eroded by sediment detachment, E_s and the material eroded by landslides, E_{ls} . Using the surface concentration of a cosmogenic nuclide at the end of the model step, $N_f^{10}\text{Be}$, the average nuclide concentration in the volume of eroded material, $N_D^{10}\text{Be}$ can be calculated by integrating over the total depth of eroded material the concentration of the nuclide as a function of e-folding depth, Λ ,

$$N_D^{10}\text{Be} = N_f^{10}\text{Be} \cdot \rho \int_{-D}^0 e^{-z(\rho/\Lambda)} dz \quad (\text{A34})$$

$$= N_f^{10}\text{Be} \cdot \rho \cdot \frac{\Lambda}{\rho} \left[-e^{-z(\rho/\Lambda)} \right]_{-D}^0 \quad (\text{A35})$$

$$= N_f^{10}\text{Be} \cdot \Lambda \left(e^{D(\rho/\Lambda)} - 1 \right). \quad (\text{A36})$$

REFERENCES

1. P. Molnar, P. England, Late Cenozoic uplift of mountain ranges and global climate change: Chicken or egg?, *Nature* 346 (1990) 29–34.
2. E. T. Brown, R. F. Stallard, M. C. Larsen, G. M. Raisbeck, F. Yiou, Denudation rates determined from the accumulation of in situ-produced ¹⁰Be in the Luquillo experimental forest, Puerto Rico, *Earth Planet. Sci. Lett.* 129 (1–4) (1995) 193–202.
3. P. Bierman, E. J. Steig, Estimating rates of denudation using cosmogenic isotope abundances in sediment, *Earth Surface Processes and Landforms* 21 (1996) 125–139.

4. D. E. Granger, J. W. Kirchner, R. Finkel, Spatially averaged long-term erosion rates measured from in situ-produced cosmogenic nuclides in alluvial sediments, *J. Geol.* 104 (3) (1996) 249–257.
5. E. M. Clapp, P. R. Bierman, A. P. Schick, J. Lekach, Y. Enzel, M. Caffee, Sediment yield exceeds sediment production in arid region drainage basins, *Geology* 28 (2000) 995–998.
6. C. S. Riebe, J. W. Kirchner, D. E. Granger, R. C. Finkel, Erosional equilibrium and disequilibrium in the Sierra Nevada, inferred from cosmogenic ^{26}Al and ^{10}Be in alluvial sediment, *Geology* 28 (9) (2000) 803–806.
7. N. Hovius, C. P. Stark, P. A. Allen, Sediment flux from a mountain belt derived by landslide mapping, *Geology* 25 (3) (1997) 231–234.
8. S. A. Binnie, J. A. Spotila, W. M. Phillips, M. A. Summerfield, K. A. Fifield, The coexistence of steady and non-steady state topography in the San Bernardino Mountains, southern California, from cosmogenic ^{10}Be and U-Th/He thermochronology, *Geol. Soc. Am., Abstr. Prog.* 35.
9. T. J. Dunai, Scaling factors for production rates of in situ produced cosmogenic nuclides; a critical reevaluation, *Earth Planet. Sci. Lett.* 176 (1) (2000) 157–169.
10. T. J. Dunai, Erratum to Scaling factors for production rates of in situ produced cosmogenic nuclides; a critical reevaluation, *Earth Planet. Sci. Lett.* 178 (2000) 425.
11. A. Dunne, D. Elmore, P. Muzikar, Scaling factors for the rates of production of cosmogenic nuclides for geometric shielding and attenuation at depth on sloped surfaces, *Geomorphology* 27 (1–2) (1999) 3–11.
12. J. Masarik, R. C. Reedy, Terrestrial cosmogenic-nuclide production systematics calculated from numerical simulations, *Earth Planet. Sci. Lett.* 136 (3–4) (1995) 381–395.
13. A. Heimsath, The soil production function, Ph.D., University of California (1999).
14. C. P. Stark, N. Hovius, The characterization of landslide size distributions, *Geophys. Res. Lett.* 28 (6) (2001) 1091–1094.
15. J. Lavé, D. Burbank, Denudation processes and rates in the Transverse Ranges, Southern California; erosional response of a transitional landscape to external and anthropogenic forcing, *J. Geophys. Res.* 109 (1) (2004) 31.
16. D. Lal, Cosmic ray labeling of erosion surfaces; in situ nuclide production rates and erosion models, *Earth Planet. Sci. Lett.* 104 (2–4) (1991) 424–439.
17. A. E. Blythe, D. W. Burbank, K. A. Farley, E. J. Fielding, Structural and topographic evolution of the central Transverse Ranges, California, from apatite fission-track, (U-Th)/He and digital elevation model analyses, *Basin Research* 12 (2) (2000) 97–114.
18. A. E. Blythe, M. A. House, J. A. Spotila, Low-temperature thermochronology of the San Gabriel and San Bernardino mountains, southern California; constraining structural evolution, in: A. Barth (Ed.), Contributions to Crustal Evolution of the Southwestern United States, Special Paper 365, Geological Society of America, 2002, pp. 231–250.
19. J. A. Spotila, M. A. House, A. E. Blythe, N. A. Niemi, G. C. Bank, Controls on the erosion and geomorphic evolution of the San Bernardino and San Gabriel mountains, southern California, in: A. Barth (Ed.), Contributions to Crustal Evolution of the Southwestern United States, Special Paper 365, Geological Society of America, 2002, pp. 205–230.
20. D. M. Morton, F. K. Miller, Preliminary geologic map of the San Bernardino 30' \times 60' quadrangle, California, Open-file Report 03-293, U. S. Geological Survey, 2003.
21. M. Julian, E. Anthony, Aspects of landslide activity in the Mercantour massif and the French Riviera, southeastern France, *Geomorphology* 15 (1996) 175–289.
22. D. W. Burbank, A. E. Blythe, J. Putkonen, B. Pratt-Sitaula, E. Gabet, M. Oskin, A. Barros, T. P. Ojha, Decoupling of erosion and precipitation in the Himalayas, *Nature* 426 (6967) (2003) 652–655.
23. J. M. Chambers, W. S. Cleveland, B. Kleiner, P. A. Tukey, Graphical Methods for Data Analysis, Wadsworth, 1983.
24. J.-c. Chang, O. Slaymaker, Frequency and spatial distribution of landslides in a mountainous drainage basin: Western Foothills, Taiwan, *Catena* 46 (2002) 285–307.
25. H. Ohmori, Morphological characteristics of the

scar created by large-scale rapid mass movement,
Chikei = Transactions - Japanese Geomorpholog-
ical Union 13 (3) (1992) 185-202.

**Exhumation of basement-cored uplifts: Example of the Kyrgyz Range
quantified with apatite fission-track thermochronology**

Edward R. Sobel ¹, Michael Oskin ², Douglas Burbank ³, Alexander Mikolaichuk ⁴

1 Institut fuer Geowissenschaften, Universitaet Potsdam, Postfach 601553, 14415 Potsdam,
Germany, sobel@rz.uni-potsdam.de

2 Dept. of Geological Sciences, University of North Carolina at Chapel Hill, Chapel Hill, NC,
USA 27599

3 Dept. of Geological Sciences, University of California, Santa Barbara, CA USA 93106

4 Institute of Geology, 30 Erkindyk Ave., Bishkek 720481, Kyrgyzstan

Abstract

The Kyrgyz Range, the northernmost portion of the Kyrgyzstan Tien Shan, displays topographic evidence for lateral propagation of surface uplift and exhumation. The highest and most deeply dissected segment lies in the center of the range. To the east, topography and relief decrease, and preserved remnants of a Cretaceous regional erosion surface imply minimal amounts of bedrock exhumation. The timing of exhumation of range segments defines the lateral propagation rate of the range-bounding reverse fault and quantifies the time and erosion depth needed to transform a mountain range from a juvenile to a mature morphology. New apatite fission-track (AFT) data from three transects from the eastern Kyrgyz Range, combined with published AFT data, demonstrate that the range has propagated over 110 km eastwards over the last 7-11 Myr. Based on the thermal and topographic evolutionary history, we present a model for a time-varying exhumation rate driven by rock uplift and changes in erodability and the time scale of geomorphic adjustment to surface uplift. Easily eroded, Cenozoic sedimentary rocks overlying resistant basement control early, rapid exhumation and slow surface uplift rates. As increasing amounts of resistant basement are exposed, exhumation rates decrease while surface uplift rates are sustained or increase, thereby growing topography. As the range becomes high enough to cause ice accumulation and develop steep river valleys, fluvial and glacial erosion become more powerful and exhumation rates once again increase. Independently determined range-normal shortening rates have also varied over time, suggesting a feedback between erosional efficiency and shortening rate.

Introduction

Growth of a contractional mountain range is driven by an evolving relationship between rock uplift, surface uplift, and exhumation. Surface uplift is defined as rock uplift minus exhumation [England and Molnar, 1990]. In the early phase of orogenesis, rock uplift must outpace exhumation; in a steady-state orogen, these reach an equilibrium, while in the final, destructive

phase of an orogen, exhumation dominates [e.g., *Willett and Brandon*, 2002]. Temporal changes in key controlling factors, such as fault geometry, shortening rate, and erosion rate will influence the surface uplift history [e.g., *Burbank et al.*, 1996; *Abbott et al.*, 1997; *Stock and Montgomery*, 1999; *Whipple and Tucker*, 1999]. Erosion rate may be controlled by factors such as channel gradients, surface slopes, relief, precipitation, glacial extent, and rock resistance [e.g., *Ahnert*, 1970; *Howard*, 1994; *Brozovic et al.*, 1997; *Hallet et al.*, 1996; *Schmidt and Montgomery*, 1996; *Sklar and Dietrich*, 2001; *Whipple*, 2004]. Perhaps because complex interactions among these factors undoubtedly occur, the detailed evolution and interdependence of these factors is rarely delineated.

Reverse-fault-bounded mountain ranges propagating into a foreland basin commonly initiate either as a single, localized structure which gradually lengthens along strike with increasing amount of shortening, or as several fault segments which eventually coalesce or overlap [*Dawers*, 1993; *Cartwright et al.*, 1995]. In either case, the active range-front likely lengthens as displacement accumulates on the range-bounding faults. After several million years of displacement, the original, relatively small structures may be impossible to discern. However, if a reference horizon along the trend of the range exists, range growth and exhumation can be placed into a topographic reference frame by combining low-temperature thermochronologic data with structural geology and geomorphic analysis. When ranges grow through lateral and vertical propagation, a space-for-time substitution can illuminate the long-term spatial and temporal distribution of exhumation and surface uplift and can permit reconstruction of progressive changes in the balance between rock uplift and exhumation [*Burbank et al.*, 1999]. Space-for-time substitutions are most reliable when time constraints exist for the interval of range propagation. Such along-strike temporal control, however, is commonly lacking in most studies of fold-and-thrust belts. Only when reliable ages can be assigned to various stages of range growth can the validity of the substitution be assessed. We report here a time-calibrated example of range propagation from the Kyrgyz Tien Shan.

The Kyrgyz range of the northern Tien Shan (Figure 1) provides an example of a reverse-fault bounded mountain range with topographic evidence for progressive lateral propagation of surface uplift and exhumation. The highest and most deeply dissected sector of the range lies in its central portion, south of Bishkek, in the region of the Ala Archa River. Glaciers mantling peaks up to 4800 m have deeply dissected the granitic range in this region, and reset apatite fission-track and U-Th/He thermochronometers indicate >5 km of exhumation at river level [Bullen *et al.*, 2003]. To the east and west, both topography and relief decrease. Moreover, preservation of remnants of a Cretaceous regional erosion surface [Trofimov *et al.*, 1976] implies minimal amounts of bedrock exhumation. If the timing of exhumation of segments of the range outward from the center can be defined, the lateral propagation rate of the range can be estimated and the depth of erosion and time needed to transform a mountain range from a juvenile to a mature morphology can be reconstructed.

Here we present new apatite fission-track (AFT) data from three transects from the eastern half of the Kyrgyz Range that, when combined with published AFT data, demonstrate that the range has propagated over 110 km from the presently highest region towards the east over the last 7-11 Myr. When synthesized with structural data and analysis of recently produced digital topography, we can reconstruct the thermal and topographic evolutionary history of the Kyrgyz range. We present a model for a time-varying exhumation rate driven by the interplay of rock erodability, surface processes, and shortening rate. We propose that easily eroded Cenozoic sedimentary rocks that overlie resistant pre-Tertiary bedrock control early, rapid exhumation and slow surface uplift rates. As increasing amounts of resistant bedrock are exposed, exhumation and shortening rates decrease while surface uplift can persist, thereby growing topography. This decrease in shortening rate may be counterbalanced by basinward-propagation of the deformation front. As the range becomes high enough to cause ice accumulation and orographically enhanced precipitation, fluvial and glacial erosion become more effective and exhumation rates once again increase. A balance between

erosion and rock uplift occurs through establishment of mature drainage networks into the range that connect high-elevation glaciated areas to deeply incised rivers. Based on analysis of the digital topography, we argue that the central part of the range has achieved this balance and represents a topographic steady state.

Geologic history

The Tien Shan records a complex Paleozoic history of island arc accretion [Burtman 1975; Carroll *et al.*, 2001; Bazhenov *et al.*, 2003] followed by Permian strike-slip deformation [Burtman 1975; Bazhenov *et al.*, 1999]. Episodes of intracontinental deformation driven by distal plate margin tectonism occurred during the Early-Middle Jurassic and the Late Jurassic-Cretaceous, documented by foreland-basin formation to the north and south of the Tien Shan, as well as in a prominent transtensional basin cross-cutting the range [Hendrix *et al.*, 1992; Sobel, 1999]. Apatite fission-track data suggest pulses of exhumation during the Permian and the Jurassic [Sobel and Dumitru, 1997; Bullen *et al.*, 2001; Dumitru *et al.*, 2001]; these are likely correlated with episodes of deformation within the Tien Shan and deposition within the Tarim basin.

A widespread regional erosion surface formed within the central Kyrgyz Tien Shan in the late Mesozoic [Trofimov *et al.*, 1976; Makarov, 1977; Chediya, 1986; see Burbank *et al.*, 1999 for photographs]. This surface is unconformably overlain by the Paleocene-Eocene Suluterek formation (also called the Kokturpak formation), containing calcareous sandstone, dolomite, gypsum, and an arid spore-pollen assemblage [Chediya *et al.*, 1973; Fortuna *et al.*, 1994] as well as localized Eocene basalt flows [Krylov, 1960]. The formation is typically ca 150 m thick and is truncated by an erosional unconformity separating it from upper Tertiary sediments [Chediya *et al.*, 1973; Fortuna *et al.*, 1994]; drilling in the Chu basin reveals that the thickness locally reaches 635 m [Burg *et al.*, 2004]. Overall, this Mesozoic to Tertiary interval of erosion and minor deposition

spans ca. 100 Myr period of tectonic quiescence, during which a stable thermal regime in the upper crust was established [Bullen *et al.*, 2001].

The Cenozoic exhumation history of the Tien Shan has been used to study the evolution of the range. Fission-track cooling ages and deposition of apparently syntectonic conglomerates in the adjacent Tarim basin suggest that shortening commenced around the Oligocene – Miocene boundary [Hendrix *et al.*, 1994; Sobel and Dumitru, 1997; Yin *et al.*, 1998]. This intracontinental deformation is driven by the Eocene – present collision of India with Asia. Deformation within the Tien Shan between 73-80°E longitude (Fig. 1) appears to have begun along the southern side of the range adjacent to the Tarim Basin at ca. 26 Ma and then propagated northwards across the individual ranges of the Tien Shan [Sobel *et al.*, 2000; Dumitru *et al.*, 2001]. Deformation has not propagated monotonically northward; at least the last several million years of this history have been marked by deformation throughout the entire range [Thompson *et al.*, 2002]. At present, seismicity is distributed throughout the width of the orogen [Bune and Gorshkov, 1980] and geodetic studies document a continuous gradient of shortening between Kashgar and Bishkek [Abdrakhmatov *et al.*, 1996; Reigber *et al.*, 2001]. Exhumation of the Kyrgyz range on the northern margin of the Tien Shan began in the region of Ala Archa (Fig. 2) at ~11 Ma [Bullen *et al.*, 2001]. Deformation is dominantly north-vergent thrusting, with a minor sinistral transpressional component [e.g., Cobbold *et al.*, 1996; Mikolaichuk, 2000; Thompson *et al.*, 2002] (Fig. 2).

The Oligocene-Miocene Shamsi Formation, exposed in the southern margin of the Chu Basin, was deposited in a foreland basin that pre-dated growth of the Kyrgyz Range [Bullen *et al.*, 2001]. The thickness of the pre-11 Ma sediment in the Chu basin is ca. 1 km. Although it is difficult to constrain the amount of Cenozoic sediment that formerly overlay the Kyrgyz range, it likely exceeded the amount in the Chu basin because of flexural subsidence of the Kyrgyz Range in advance of the northward propagating Tien Shan uplift. This pre-11 Ma burial contributed to the maximum temperature experienced by basement samples during the Neogene. During subsequent

exhumation, the weakly lithified Neogene sediment could be more readily eroded than the underlying Paleozoic strata. The Chu basin is deepest in the region of Bishkek and becomes shallower to the east, west, and north [Abdrakhmatov *et al.*, 2001] (Figure 2), suggesting that the magnitude of flexural subsidence and hence the amount of thrusting in the Kyrgyz range is greatest in the central section of the range. Bullen *et al.* [2001; 2003] present a detailed basin and tectonic analysis based on the stratigraphy and magnetostratigraphy of the last ca. 9 Ma of the Chu basin fill combined with structural and apatite U-Th/He and fission-track thermochronologic studies of the central Kyrgyz range. This work demonstrates that the range was rapidly exhumed between 11 and 10 Ma along a north-vergent thrust; deformation and cooling rates decreased significantly for the next 7 Myr until 3 Ma, when rates increased again. The deformation front propagated slightly between 8 and 3 Ma, coinciding with coarsening-upwards deposition in the basin. During the last 3 Myr, sediment accumulation rates reached a maximum, while the Kyrgyz range was being rapidly exhumed; deformation propagated farther into the foreland, forming a piggyback basin.

Geomorphology and Neotectonics

GPS measurements indicate ~20 mm/yr of modern shortening across the central Tien Shan: nearly half of the total convergence rate between India and Asia [Abdrakhmatov *et al.*, 1996; Reigber *et al.*, 2001]. This shortening is distributed across a 400-km-wide belt of subparallel ranges and intramontane basins that are separated by active reverse faults [Thompson *et al.*, 2002]. The Kyrgyz Range forms the northernmost topographic crest within the central Tien Shan. Young thrust-fault scarps and seismicity along the northern margin of the range [Chediya *et al.*, 1998; Thompson *et al.*, 2002] attest to ongoing shortening. These ranges form an orographic barrier, with precipitation focused on the northern flanks [Aizen *et al.*, 1995].

From a structural perspective, a propagating range would be expected to exhibit increasing amounts of rock uplift and structural relief as a function of distance from the tip toward the center

of the range. From a geomorphological perspective, the temporal lag between surface uplift and erosional response [Kooi and Beaumont, 1996; Willett, 1999] suggests that relief, peak height, hillslope angles, and mean elevation should all initially increase as the range grows. As a range approaches or attains a topographic steady state, relief, mean elevation, and hillslope angles should stabilize. Hillslope angles, topographic relief, and hypsometry were derived from the 3-arcsec DEM (SRTM, 2003) resampled into Universal Transverse Mercator projection with 70 m pixels. Hillslope angle, mean and maximum elevation of the Kyrgyz Range all attain average values within 50 km of its eastern tip, supporting the contention that range-scale topographic steady state may prevail over the majority of the range (Fig. 1c).

A view of the early stages of geomorphic evolution of the Kyrgyz range is provided by observations of uplifted and deformed remnants of the pre-Cenozoic erosion surface on its southeastern slope (Fig. 3). This exhumed unconformity surface is recognized in the field and on remote sensing images as concordant, uniformly tilted regions etched by a distinctive dendritic network of shallow bedrock channels [Oskin and Burbank, *Alpine landscape evolution dominated by cirque retreat, submitted manuscript to Geology, hereafter referred to as Oskin and Burbank, submitted manuscript*]. On the southern flank of the Kyrgyz Range, southward tilting of the erosion surface remnants increases from east to west, consistent with a model of increasing displacement and range-scale limb rotation above a listric thrust fault [Erslev, 1986], such as is proposed to underlie the Kyrgyz Range [Abdrakhmatov *et al.*, 2001]. Field observations at the southern foot of the range and at other nearby outcrops of the erosion surface indicate that it is exhumed from beneath easily eroded Cenozoic continental sedimentary rocks. Remnants of the erosion surface can be traced from the foot of the range to the range crest in the easternmost south-facing slope of the Kyrgyz Range. Outcrops of the erosion surface diminish westward in response to progressively greater range uplift above the Pleistocene glacial equilibrium line altitude (ELA), and corresponding incision of glaciated valleys into bedrock. North-facing glaciated valleys also

expand laterally via cirque retreat into low-relief south-facing erosion surface remnants [Oskin and Burbank, submitted manuscript]. This process expands the area covered by north-flowing glaciers (Fig. 3) and moves the drainage divide relatively southward.

Morphometric analyses of drainage basins that descend from the crest of the Kyrgyz Range link catchment-scale erosion and relief generation to range-scale topographic development. Most of our morphometric analyses focused on the north-facing catchments that reach the range crest. Basins were each derived with standard hydrologic routing functions and hypsometry and hillslope angles (Figure 4) were measured directly from the topography and its derivative, respectively. Relief measurements, calculated as the difference between two elevations, are inherently subject to bias from the horizontal length scale between elevation measurements. Rather than measure mean relief over a fixed distance, which would primarily reflect mean hillslope angle, an alternative relief measure was devised to convey the degree of overall range dissection. This relief measurement, termed here as the internal relief, is defined as the maximum elevation difference among all elevation points equidistant from the basin outlet, e.g., the lowest and highest elevation among all the points that are 5 km from the outlet. Typical values of internal relief climb monotonically upstream from the basin outlet, hover around a maximum level in the middle basin reach, and descend towards the divide (Fig. 5). In practice, internal relief correlates to the product of basin area and mean hillslope angle, and therefore provides a measure of the ridge-to-valley relief that reveals how extensively glaciers and rivers have incised below adjacent peaks. Because extreme values of relief and elevation within Kyrgyz Range catchments tend to bias values toward isolated high peaks that occupy only a small fraction of the landscape, the upper quartile of internal relief and the lower, middle, and upper quartiles of elevation (as defined by the hypsometry) provide a better characterization of key topographic attributes (Fig. 4).

The distributions of hillslope angle, hypsometry, and internal relief from east to west within the Kyrgyz Range reveal a pattern of initial surface uplift followed by dissection and then stabilization

of range-scale morphology. At the easternmost end of the range (surface uplift zone on Fig. 4), the upper quartile of internal relief is < 600 m, the mean elevation is <3100 m, peak heights are <4000 m, and the range of hypsometry (measured by difference between the 1st and 3rd quartiles of the hypsometry) is <500 m. Low relief and a limited range of altitude indicate only limited dissection of this high mountain range and support predominance of surface uplift over erosion here. Moving westward, peak elevations, internal relief, and the range of hypsometry all continue to increase toward the center of the Kyrgyz Range (transition zone on Fig. 4), whereas the mean elevation remains nearly constant across this 80-km span. The increase in the elevation of the highest peaks suggests that total rock uplift increases toward the west. Similarly, the growth of internal relief and hypsometric range indicate increasing dissection across this tract. In this zone, adjacent basins compete to attain necessary size and gradients in order to balance rock uplift. Overall stability of morphologic indices along the central part of the range (steady morphology zone, Fig. 4) suggests that this region may have reached an equilibrium topographic form in which erosion by balances tectonic uplift.

Fission-track methodology

Apatite fission-track data from exhumed basement rocks often yield distinctive age-elevation patterns that can be used to infer the low-temperature exhumation history of a range. Samples may have been exhumed from sufficient depth during the most recent exhumation event that the maximum temperature, T_{max} , exceeded the total annealing temperature (Figure 6a). In this case, the fission-track clock was reset to zero, and fission-track data record information on the time-temperature cooling path of the sample as it cooled through the partial annealing zone (PAZ) during exhumation [e.g. *Green et al.*, 1989a, 1989b]. For apatites that are cooled moderately rapidly (10°C/Myr) and which have kinetic parameters similar to Durango apatite, the total annealing temperature is ~120°C [*Donelick et al.*, 1999; *Ketcham et al.*, 1999]. Samples in the rock

column above the total annealing isotherm experienced lower T_{\max} prior to exhumation; these samples resided in the (now exhumed) PAZ for some period of time and therefore have ages reflecting the penultimate cooling event, (strongly) modified by partial annealing [e.g., *Fitzgerald et al.*, 1995] (Figure 6a). The age of the transition between these two suites of samples is interpreted to represent the onset of rapid exhumation.

The apatites analyzed in this study often have variable kinetic properties, as documented by both etch pit diameter (D_{par}) and Cl content. These two methods have been shown to yield equally useful data for assessing the kinetic properties of apatite [*Donelick et al.*, 1999; *Ketcham et al.*, 1999]. In particular, apatites distinguished by large etch-pit diameters and high Cl content (herein termed “more resistant”) are typified by higher annealing temperatures in contrast to less resistant apatites [e.g., *Green et al.*, 1989b; *Ketcham et al.*, 1999]. Given these contrasting annealing temperatures a superficial interpretation of an age-elevation plot can yield false conclusions about both the onset and rate of exhumation. Although the total annealing temperature of different apatite types is variable, the low temperature annealing behavior of apatites appears to be similar [*Ketcham et al.*, 1999]. Therefore, the slope of the exhumed partial annealing zone on an age-elevation plot for different apatite types cannot be assumed to be parallel (Figure 6). To avoid this pitfall, we have plotted age-elevation curves for apatites with similar kinetic properties. The long period of tectonic quiescence prior to the onset of Neogene exhumation implies a stable thermal structure in the upper crust [*Bullen et al.*, 2001]. Therefore, the slope of the age-elevation curve within the exhumed PAZ for kinetically similar apatites which have experienced similar thermal histories should be about the same for all of our profiles. This assumes that only a small, similar amount of horizontal-axis rotation has been experienced at each of the profiles located in the hanging wall of a major thrust. A contrasting age-elevation slope will pertain for apatites with differing kinetic characteristics (see Figure 6).

Sample preparation and analytical details are presented in Table 1. The young apatite samples yielded very few horizontal confined track-length measurements; up to 100 track-lengths were measured from older samples. For age determinations, 15 to 31 grains per sample were selected at random and dated; 1 sample yielded only 4 countable grains. Following convention, all statistical uncertainties on pooled ages and mean track lengths are quoted at the $\pm 1\sigma$ level, but $\pm 2\sigma$ uncertainties are taken into account for geologic interpretation. To assess the kinetic properties of apatite, four Dpar measurements were averaged from each dated crystal and from each crystal which yielded a confined track length, provided that sufficient etch pits were present. Dpar values are operator and etchant-dependent [Sobel *et. al.*, 2004]. Therefore, seven samples were also analyzed with a CAMECA SX-50 or SX-100 electron microprobe in order to determine Cl content (Table 1). Every crystal with a single grain age or a confined track-length measurement was probed. The microprobe data were used to calibrate the Dpar measurements.

In the context of age-elevation data, we utilize the AFT data from 3 transects to reconstruct the onset and rate of exhumation for each transect. Subsequently, Cenozoic burial and exhumation histories are evaluated using thermal models of higher elevation samples.

Results

Shamsi

Samples were collected along a tributary of the Shamsi river valley between 2250 and 3770 m along a transect that traverses a continuous sequence of Carboniferous quartzite from the base of the valley up to the crest of the east flanking ridge (Fig. 3).

The six samples yielded Miocene to Jurassic ages, generally increasing with elevation (Table 1; Figure 7. Four of them define a readily interpretable succession that captures the base of an exhumed partial annealing zone. These samples also illustrate the complications introduced by apparent mixtures of apatites with different annealing temperatures within the same bedrock

sample. With an age of 6.3 ± 0.8 Ma, the basal, youngest sample (TS164) passes the χ^2 test; all analyzed grains have similar kinetic properties as shown by Dpar ($1.74 \mu\text{m}$, SD 0.11) and microprobe (0.07 wt% Cl, SD 0.05) (Table 1; Figure DR1). The next sample (TS165) has a central age of 14 ± 7 Ma and fails the χ^2 test. Eleven of the twelve countable grains form a young population, pass the χ^2 test with a pooled age of 6.7 ± 1.8 Ma and a mean Dpar of $1.74 \mu\text{m}$. A single grain has an age of 124 ± 44 Ma and a Dpar of $2.04 \mu\text{m}$. However, microprobe data does not differentiate this grain; the average chlorine value of the sample is 0.12 wt% and the old grain has a value of 0.11 wt%. The third sample (TS166) passes the χ^2 test and has a pooled age of 17 ± 2 Ma and a Dpar value of $1.74 \mu\text{m}$. The highest elevation sample (TS170) fails the χ^2 test and has a central age of 91 ± 6 Ma, a Dpar value of $1.65 \mu\text{m}$, and 0.12 wt%cl. However, one crystal has an anomalously high wt%cl of 0.45%; excluding this grain, the sample passes the χ^2 test and has a pooled age of 88 ± 5 Ma and 0.07 wt%cl. For these latter two samples, there is no relationship between age and Dpar. Excluding the single old, high Dpar grain in sample TS165, these 4 samples can be plotted together on an age-elevation plot (Figure 7).

The lower two samples show rapid cooling, while the upper two show slow cooling within an exhumed PAZ. The inflection point between the two segments, at ~ 2800 m and 7 Ma, defines the onset of rapid cooling. Assuming that the sample experienced some amount of heating due to Miocene sedimentation prior to rapid exhumation, the total annealing temperature corresponding to the inflection point of this low Cl path is 100-105°C. Based on the age and elevation differences of these two partially reset samples, the apparent exhumation rate for the exhumed PAZ is about 12 ± 1 m/Myr (0.012 ± 0.001 km/Myr). This value will be used to define the apparent exhumation rate for the exhumed PAZ at Issyk Ata, because this section experienced a similar burial history (c.f. Fig. 6). As will be shown below, the corresponding rate at Boom Gorge is ca. 0.01 km/Myr, supporting this assumption. After 7 Ma, the rate at Shamsi accelerated to ~ 1 km/Myr.

Two additional samples lie within the exhumed PAZ. Both pass the chi-squared test. TS167 has an age of 67 ± 3 Ma, Dpar of $1.96 \mu\text{m}$ and 0.10 wt\%Cl (0.08 wt\%Cl excluding 5 grains with high values); TS169 has an age of 151 ± 6 Ma, Dpar of 2.04 and 0.26 wt\%Cl (Table 1; Figure DR1). Because TS169 is significantly older than the two bounding samples TS167 and TS170, plotting all of the samples within the exhumed PAZ together cannot yield a readily interpretable age-elevation plot. However, placing kinetically different samples on subparallel trends reveals that more resistant apatites have consistently older ages, representing older portions of a single exhumed PAZ.

Issyk Ata

Samples were collected from a transect along the Issyk Ata river valley between 1840 and 3290 m. (Fig. 4). Nearby, glaciated peaks reach elevations of 4500 m. The transect samples primarily Late Ordovician granite; the second sample above the base is an apatite-poor Riphean metavolcanic rock.

Five of the six analyzed samples pass the chi-squared test, yielding ages ranging from 3.9 ± 0.7 Ma to 6.9 ± 0.6 Ma (Table 1; Figure 7). Four of these samples, Mav38, TS158, TS159, and TS162 appear to be monocompositional based on Dpar measurements and microprobe analysis. Dpar values are 1.65, 1.36, 1.87, and 1.92, respectively; the former sample yields a wt\%Cl of 0.02 (Table 1; Figure DR1). Sample TS163 yielded only 4 countable grains; the resulting age is consistent with the other samples but of too low precision to warrant further attention. Sample TS161 contains two components that each pass the chi-squared test. A young population of 25 grains yields an age of 7.6 ± 1.9 Ma; an older component with 6 grains provides an age of 102 ± 11 Ma. The younger population has a Dpar of $1.72 \mu\text{m}$ and a wt\%Cl of 0.02. Kinetic characteristics do not explain all of the grains in the older population: 5 of the 6 older grains yield higher values of 0.17 wt\%Cl , whereas 1 grain has a value of 0.01 wt\%Cl . Three of the old grains have large Dpar values of 2.43;

the other 3 fall within the cluster of young grains with an average value 1.83. When combined, the 6 grains have an average value of 2.13 μm .

The young, low resistant grains from these 6 samples define a steep linear trend on an age-elevation plot, indicating rapid cooling from below the base of an exhumed PAZ. The trend of the corresponding exhumed PAZ is assumed to have the same slope as the corresponding curve at Shamsi. Due to the absence of low resistance, partially reset samples, the position of this latter curve is poorly defined; hence, the onset of this rapid cooling can only be constrained as older than about 8 Ma. Using Fig. 6D as an analogy, the slope of the exhumed PAZ through the more resistant component of sample TS161 should have the same slope as the less resistant component; the two curves should be separated by a vertical distance corresponding to the difference in T_a for the two components. Although the more resistant slope is poorly constrained, this analysis suggests that the onset of rapid cooling should be represented by an elevation close to TS161 and hence only slightly older than 8 Ma.

Boom gorge

Two samples were collected from the Boom gorge along the Chu River at 1375 and 1530 m; these lie ca. 1500 m below the local peaks (Fig. 4). Both samples are from topographically low positions in the footwall of the main range-bounding thrust, in contrast to the hanging wall sections sampled at Shamsi and Issyk Ata. Cenozoic sediments lying above the regional erosion surface are preserved in the center of the range, overthrust by Paleozoic strata. The same sedimentary sequence lies north and south of the range, overthrust from the south and north, respectively. The Cenozoic strata in this region do not exceed 1.5 km in thickness [Trofimov *et al.*, 1976]. Sample TS84 was collected from a Permian granite just below the erosion surface; both the granite and the Cenozoic strata have been overthrust by Paleozoic units. Sample TS27 was collected from Devonian - Upper Carboniferous sandstone.

The two samples both pass the chi-squared test, with pooled ages of 128 ± 10 and 150 ± 8 Ma (Table 1; Figure 7). The older sample, TS84, has a Dpar of $1.70 \mu\text{m}$ (Table 1; Figure DR1). The younger sample, TS27, was prepared with slightly different etching conditions; therefore, Dpar was not measured. The samples yielded similar track-length data of 12.50 and $12.82 \mu\text{m}$, respectively. The two samples lie on a cooling trend representing an exhumed PAZ; assuming that the two samples have the same kinetic characteristics, they experienced an apparent exhumation rate of 0.01 km/Myr . Because sample TS27 was collected from a structurally deep position within the Boom gorge, the amount of exhumation in the gorge is clearly limited.

Thermal modeling

Track-length modeling cannot determine a unique thermal history; rather, it yields a range of solutions which are consistent with the observed data. Thermal modeling combining track length, single crystal ages and weight percent chlorine were performed using the AFTSolve program [Ketcham *et al.*, 2000] and the annealing model of Ketcham *et al.* [1999]. This program determines the best-fit models as well as good and acceptable fits. Modeling of partially annealed samples provides good constraints on the total annealing temperature and the maximum Miocene burial temperature; the minimum temperature prior to Late Cenozoic burial is less well constrained. With information on the thermal state of the crust, this information delineates the depth of the sample below the regional erosion surface and the Late Cenozoic sediments that formerly overlay the area. The constraints on the time of final exhumation of partially annealed samples from modeling are often less precise; however, this information may be available from lower elevation samples in the same transect.

Converting thermal histories into exhumation paths requires information on the thermal state of the crust and, ideally, thermal conductivity. Borehole data suggest that the geothermal gradient within the study area is presently $25\text{-}30^\circ\text{C/km}$ [Gubin, 1986]; herein, we use a value of 26°C

[Shvartzman, 1992]. Conductivity data are sparse. Exhumation rates are more difficult to calculate, given that one must also consider advection of isotherms due to thrusting [e.g., Brown and Summerfield, 1997; Mancktelow and Grasemann, 1997] and perturbations of isotherms due to topographic effects [e.g., Stüwe *et al.*, 1994]. In this study, neither factor likely had a significant effect, because there was almost no relief when exhumation began and there were only a few kilometers of rapid exhumation. As will be shown below, significant relief likely developed after the main phase of rapid exhumation had already set the fission-track ages.

Two of the Shamsi samples, TS167 and TS169, yielded sufficient track-length measurements to permit robust thermal modeling (Figure 8); however, given that TS169 yielded twice as many measurements, these results are considered more reliable. Both samples were modeled using four time-temperature constraints. Models were started at 250 Ma, with a temperature range between 70 and 160°C, such that all tracks initially formed could be completely annealed. The observed shortened track-length distributions require a late-stage heating event, consistent with burial heating due to the Oligo-Miocene depositional history discussed above. Three runs were made for each sample, with modeled reheating started at 30, 25, or 20 Ma. At this time, the model permitted sample temperatures between 25°C and 90°C, consistent with the samples being close to the paleo-surface. The peak reheating age of 7 Ma was set to match results from the vertical profile. The maximum reheating temperature was constrained to be between 30°C and 100°C. The final constraint was the present surface temperature of 10-20°C. Acceptable fits were not limited by the temperature or the position of the constraints, with the exception of the age of maximum reheating. Temperature paths between adjacent constraints had 8 segments. Heating and cooling rates were not constrained. Each model run had 10,000 iterations, using a Monte Carlo approach.

Several conclusions can be drawn from the modeling data (Figure 8 and Table 2). The influence of the Miocene sedimentary burial is significant; numerous model runs (not shown) which neglect this reheating did not produce good fits. The total annealing temperature (T_a)

depends on both apatite kinetic characteristics and cooling rate. T_a can be estimated as the best-fit temperature at which the oldest preserved track formed; the modeled temperatures can be verified by comparison with calculated temperatures reported by *Ketcham et al.* [1999]. Results from shallow samples can be used to understand the behavior of structurally deeper samples with similar kinetic characteristics because the temperature where and when the inflection point in the PAZ curve formed was approximately T_a . This position would have been buried beneath a column of bedrock and the Oligo-Miocene sedimentary basin.

The amount of Miocene reheating experienced by the samples provides a measure of the thickness of the Oligocene-Miocene sedimentary basin deposited prior to the onset of uplift of the Kyrgyz Range. From this reheating history, the thickness of the exhumed bedrock section and hence the subsurface position of the exhumed erosion surface can be estimated. Assuming a geothermal gradient of 26°C/km and based on the range of modeled heating of 18-34°C (Table 2) between 0.7 and 1.8 km of sediment was deposited at Shamsi. The broad range is partially due to the reduced sensitivity of the model at the low temperatures experienced prior to burial. Therefore, a more robust calculation taking into account the unsteady thermal conditions within a young sedimentary basin is inappropriate. However, the sedimentary thickness calculated is in agreement with geological observations from the Chu basin [*Chediya*, 1986; *Bullen et al.*, 2003].

AFTSolve modeling of sample TS84 from the Boom Gorge cannot precisely constrain the timing of final exhumation (Figure 8). The modeling strategy was similar to that used with the Shamsi samples, except that reheating began at 10, 15 or 20 Ma and final cooling began at 2, 3 or 5 Ma. Best-fit models suggest only 4-22°C of Neogene heating below the sedimentary basin; however, acceptable fits permit up to 32°C of heating, consistent with the up to 1.5 km of sediment preserved nearby.

Discussion

Multi-compositional age-elevation plots

Kinetically similar age-elevation curves at Shamsi and Issyk Ata represent an exhumed PAZ and are expected to have similar slopes, consistent with geological data that suggests that they have experienced similar thermal histories. However, curves within the same transect representing apatites with different resistances to annealing are often not parallel because both the T_a and the influence of Cenozoic burial heating are different. For instance, a more resistant apatite is reset at a lower elevation (higher temperature); at intermediate elevations, this apatite will display an older age than less resistant apatite because the former has experienced less annealing in the (now exhumed) PAZ (Figure 6A). In the case of a single large exhumation event, more resistant apatites should lie on a steeper trend within the PAZ. However, subsequent reheating due to burial beneath a sedimentary basin can partially reset this exhumed PAZ, creating a zone with a parallel trend (Fig. 6C). Subsequent exhumation can expose this history (Fig. 6D). In such a case, the transition from parallel to convergent paths in the exhumed PAZ marks the base of older exhumed PAZ. At Shamsi, this transition occurs 1 km above the base of the ultimate exhumed PAZ (Fig. 7). Making the simplifying assumptions that isotherms have not been perturbed and that the geothermal gradient has remained constant, and with independent information on the amount of burial, it is possible to estimate the magnitude of the older exhumation event (cf. Fig. 6D). If burial beneath the Chu basin was 1 to 1.5 km, this suggests that the magnitude of the exhumation event associated with creation of the Cretaceous erosion surface was 2 to 2.5 km. The range of old ages obtained from the Kyrgyz range and the adjacent Chu basin [this study; *Bullen et al.*, 2001] also implies that the penultimate exhumation event was not large enough to reset more thermally resistant all apatites.

Three-stage cooling history

Variable age-elevation slopes for kinetically dissimilar apatites support Oligo-Miocene burial followed by a three-stage cooling history for the Kyrgyz Range: (1) rapid cooling during removal of Cenozoic cover strata, (2) initially reduced erosion and cooling following exhumation of pre-Cenozoic bedrock, and (3) renewed rapid cooling and erosion into bedrock (Figure 9). This history is best defined by the Shamsi age-elevation curve. Only the lower portion of the Issyk Ata curve can presently be well defined with this cooling history. Although erosion has partially removed the AFT record of three-stage cooling at Ala Archa, it is also defined by U-Th/He dating of apatite there [Bullen *et al.*, 2003].

For Issyk Ata and Shamsi, the portion of the age-elevation plot below the inflection point yields apparent exhumation rates of ca. 0.4 and ca. 1 km/Myr, respectively. The ca. 1 to 1.5 km of sediment overlying the basement would require between 2 to 4 Myr and 1 to 1.5 Myr, respectively, to have been removed at these rates. For Shamsi, where the age and paleodepth of the inflection point is well constrained as 7 Ma and 4.0 to 4.6 km (Figure 7), the mean exhumation rate from this point to the surface is 0.6 to 0.7 km/Myr. This suggests that the rapid cooling recorded in the age-elevation profiles reflects the removal of the sedimentary section and that the exhumation rate decreased at least slightly afterwards. Similar conclusions about the magnitude of exhumation were reached by Bullen *et al.* [2003] for the Ala Archa section, based on both apatite fission-track and U-Th/He thermochronology. In particular, these authors concluded that a ca. 1 Myr pulse of rapid exhumation at ~ 11-10 Ma removed 1.5 km of section at 1.0 to 1.5 km/Myr. Subsequently, the exhumation rate decreased to <0.3 km/Myr until 3 Ma, when the rate increased again to 0.8 km/Myr. These changes were similar in magnitude to synchronous changes in rates of shortening along the northern flank of the central Kyrgyz Range and rates of sediment accumulation in the Chu Basin [Bullen *et al.*, 2003]. The fission-track data presented in this study cannot address whether the exhumation rate changed in the last several Myr at Issyk Ata or Shamsi.

The three-stage cooling pattern documented in the Kyrgyz range is likely to be broadly applicable. The typical geometry of a foreland-propagating thrust belt includes a foreland basin that is eventually disrupted by the advancing reverse-fault-front (Figure 9). In this setting, uplift above a new thrust or fold first exhumes the recently deposited sediment of the foreland basin. These sediments are typically poorly cemented and therefore easily eroded. Only when the vertical displacement of the fault exceeds the thickness of the overlying young sediment are older units exposed. Easily eroded, recently deposited sedimentary rocks can be rapidly exhumed with negligible surface uplift. As increasing amounts of resistant basement are exposed, exhumation rates decrease while surface uplift rates increase, if shortening rates remain steady [c.f., *Burbank et al.*, 1999; *Sobel and Strecker*, 2003]. Surface processes immediately respond to topographic relief developed by range growth and initiate drainage networks that can eventually bring erosion rates into balance with rock-uplift rates. Orographically enhanced precipitation and glacial erosion may further enhance the effectiveness of erosion as the range grows. At this point, if the time scale of geomorphic adjustment to range uplift is sufficiently rapid, range morphology may reach a steady state dictated by the interplay of surface processes and rock uplift.

Lateral propagation rate

The transition from slow cooling, followed by burial, to rapid cooling measures exhumation of the Kyrgyz Range via initial erosional stripping of Cenozoic cover strata at the onset of thrusting at the range tip. The best estimates for the onset of this rapid exhumation are 11 ± 1 Ma at Ala Archa [*Bullen et al.*, 2001] and 7 ± 0.5 Ma at Shamsi; these sections are 64 ± 7 km apart (Figure 7). The start of exhumation at Issyk Ata, located half-way between these locations, can only be constrained as slightly older than 8 Ma. Plotting initiation age versus distance east of Ala Archa shows that the range has propagated eastward at ca. 16 ± 6 km/Myr from 11 to 7 Ma.

Progressive changes in the geomorphology of basement rocks that form the easternmost Kyrgyz Range provides some independent constraint as to the relative rates of lateral propagation and uplift. As soon as rock uplift raises the Cenozoic sedimentary cover rocks above local base level, they appear to be rapidly stripped from above the pre-Cenozoic erosion surface and do not contribute significantly to the topography of the range. Topographic relief grows primarily within the pre-Cenozoic bedrock via surface uplift that results from the competition between rock uplift and exhumation. The abrupt increases in mean and maximum basin elevation in the surface uplift zone with only nominal gain of internal relief suggests that the form of the nascent range near its terminus is dictated primarily by rock uplift above the south-dipping thrust fault, that peak heights are correlated with the magnitude of fault slip, and that the magnitude of dissection is minimal. The gradient of peak elevations in the surface uplift zone define an east-west slope of $13\% \pm 2\%$ (Fig. 4), which, if built by thrusting at a uniform slip rate and without significant erosion of the peaks, corresponds to a lateral propagation rate that is only 7 to 9 times the rock uplift rate. Such a gradient could not have applied over the entire interval of range growth, however, because it would require over 15 km of rock uplift in the central part of the range: an amount inconsistent with the Ala Archa fission-track data. Hence, the propagation/rock-uplift ratio appears considerably lower near the eastern tip of the range than it does farther west. A quasi-elliptical distribution of fault slip, similar to that documented for propagating normal faults [Dawers, 1993], could be responsible for a steeper rock-uplift gradient on the presently propagating easternmost tip of the Kyrgyz Range than that derived from Miocene exhumation of the central part of the range. Alternatively, a diminished lateral propagation rate could have arose in response to structural interference [Gupta and Scholz, 2000] with reverse faults and strike-slip faults emerging from the Kungey Alatau to the northeast. Independent geochronological constraints of either fault slip rate or the ages of initiation of glaciation in the easternmost Kyrgyz Range as rocks were uplifted above the glacial ELA could test these predictions.

Geomorphic adjustment to bedrock uplift

The geomorphic evolution of the Kyrgyz Range supports progressive adjustment of surface uplift and incision in response to rock uplift. At the easternmost propagating tip of the Kyrgyz Range, limited dissection of the pre-Cenozoic erosion surface enhances surface uplift and dampens internal relief. This contrasts with the steady morphology zone in the central part of the range (Fig. 4) where the pre-Cenozoic erosion surface has been completely removed and large north-facing basins with > 1000 m of internal relief predominate. Given the north-vergent underlying thrust faults and the structural culmination along the northern edge of the range, the observation that the south-facing basins are significantly smaller than the north-facing basins suggests that the northern basins have grown at the expense of south-facing ones. This southward migration of the drainage divide results in a drainage asymmetry that is opposite to that expected for ranges developed above a (singular) actively deforming structure, wherein the steep limb or flank with shorter catchments lies above the active fault [Leeder and Jackson, 1993; Talling, 1997; Burbank and Anderson, 2001]. However, this observation is consistent with both range asymmetry driven by > 1000 m lower base-level on its north side [Ellis and Densmore, 2003] and with the higher precipitation received on the north flank of the range [Aizen *et al.*, 1995].

The transition zone, which lies between the zone of surface uplift and the zone of steady morphology, provides important insight into the transformation of the Kyrgyz Range by surface processes. Peak heights increase gradually from east to west within the transition zone, albeit at a much more gentle gradient than in the eastern surface-uplift zone, because of greater competition between rock uplift and erosion. The most striking aspect of the transition zone is that mean elevation attains a near-constant value of ~ 3200 m despite ongoing growth of peak heights, range of hypsometry, and internal relief (Fig. 4). Systematic increase of north-facing basin size explains these contradictory elevation and relief trends. The first significant enlargement of north-facing

basins occurs where peak elevations exceed 3500 m elevation above mean sea level (Fig. 4), enabling Pleistocene glaciation of the range crest to lengthen north-facing basins southward via cirque retreat (Figs. 3 and 5), [Oskin and Burbank, *submitted manuscript*]. Internal relief increases only modestly within these glacially expanded north-facing catchments because glacial erosion is limited to high elevations. Consequently, hypsometry remains concentrated near the glacial ELA [c.f. Brozovic *et al.*, 1997]. Further west within the transition zone, expansion of north-facing basins eventually leads to more effective fluvial and glacial erosion at lower elevations, which in turn causes the range of hypsometry to expand and internal relief to grow to >1500m. In the westernmost transition zone, the internal relief attains its maximum as rivers in deeply incised valleys abut against hillslopes that are at or near the threshold angle for failure. Overall, the transition zone appears to be a region of stabilization of elevation, if not locally even of surface depression, as large north-facing basins enlarge and mature.

Coupled Exhumation and Shortening

Structural reconstructions of the central Kyrgyz Range [Bullen *et al.*, 2003] suggest the pattern of shortening may be correlated to the exhumation rate. Initial, rapid shortening corresponds to high cooling rates during removal of Cenozoic cover rocks from the crest of the range. This was followed by a period of slow shortening rate and backthrusting within the foreland basin, north of the Kyrgyz Range, corresponding to a period of slow exhumation of Paleozoic bedrock. In the past 3 Myr, both shortening rate and exhumation of the bedrock core have increased. If the exhumation history of the Kyrgyz Range is driven by the interplay of rock erodability with both rock and surface uplift, then this correlation could indicate a feedback mechanism whereby exhumation rates are reduced when more resistant rocks are at the surface, thereby building topography. To the extent that larger topographic loads require more work for a given increment of shortening and rock uplift, shortening and both rock- and surface uplift rates may diminish as topography grows and the

locus of deformation shifts elsewhere in the range [e.g., *Masek and Duncan, 1998*]. If erosion in a given range is inefficient and its topography grows, the increased load may cause shortening rates to diminish or deformation to shift entirely to a site requiring less work. This model predicts variations in exhumation rate with time driven by changes in erosion parameters; the evidence of this behavior should be detectable both in the cooling history of the range and in the depositional history of the adjacent basin. If the Kyrgyz Range has continued to evolve in a similar manner to that expressed in the bedrock and detrital cooling history [*Bullen et al., 2003*], then the along-strike geomorphic evolution of the range should also be consistent with the proposed exhumation model. Here we explore the plausibility of coupling between surface uplift and shortening rate at the range scale.

In the Kyrgyz Range, a short pulse of rapid cooling at several sites is associated with 1 to 1.5 km of exhumation; this thickness corresponds well with the thickness of the young sedimentary basin which formerly overlay the range. Therefore, most of this pulse of rapid cooling is probably attributable to the removal of this sediment during the initial phase of rock uplift. Because the young sedimentary rocks are more easily eroded than the underlying Paleozoic units, this short episode of rapid cooling likely corresponded to only a small amount of surface uplift [*Bullen et al., 2003*]. Only when a significant amount of bedrock was exposed could the surface uplift increase and the concurrent exhumation rate decrease. This pattern is seen in the geomorphology of the surface uplift zone of the Kyrgyz Range, where easily eroded Cenozoic rocks are rapidly removed from the range but the underlying pre-Cenozoic unconformity surface is widely preserved up to high elevations. The observation that an initial pulse of rapid exhumation propagates along the strike of the range, roughly normal to the principal shortening direction, suggests that the range is growing due to lengthening of the bounding structure rather than due to changes in the regional stress field.

Bullen et al. [2003] suggested that the decrease in exhumation rate at ca. 10 Ma at Ala Archa was associated with the observed decrease in range-normal shortening rate and with a shift from thrusting to backthrusting. We further suggest that, as the range-bounding thrust fault lengthened, this deformation pattern likely propagated along the strike of the range in the same manner. Basinward propagating foreland thrust faults and folds, including prominent backthrusts, are observed along the length of the range east from Ala Archa. We deduce from the thermal history of lateral range propagation that these foreland faults have also propagated eastward as the range itself propagated.. Such a spatially varying decrease in shortening rate, if supported from the history of these foreland structures, would suggest a feedback between the size of the range and the activity of the basal thrust and growing topography [cf. *Davis et al.* 1983]. We speculate that the geomorphic transition zone is the surficial expression of a coupled deformation-erosion system that is out of balance, leading to a feedback between erosional efficiency and the locus of deformation.

Steady state time scale

Consistency between the cooling history and the along-strike geomorphic evolution of the Kyrgyz Range supports the hypothesis that exhumation rate, and possibly also shortening rate, are modulated by the time scale of adjustment of surface processes to rock uplift. No single steady state time scale adequately describes the variety and significance of adjustments toward steady morphology in the Kyrgyz Range. Erosion is immediately effective at stripping the cover from the pre-Cenozoic erosion surface, supporting an initial, short adjustment time of less than 1 Myr for steady state rock uplift and erosion of Cenozoic strata. Conversely, significantly longer time periods are necessary for erosion to balance rock uplift of resistant Paleozoic basement. In the surface uplift zone, below the elevation of glacial ice accumulation, surface processes fail to substantively alter the structural form of the range. Low elevation ranges of the western Tien Shan commonly preserve extensive areas of the pre-Cenozoic erosion surface [*Abdrakmatov et al.*,

2001], indicating that the steady state time scale in the absence of glaciation is longer than the time since Early to Mid Miocene onset of uplift. Glaciation of the easternmost Kyrgyz Range triggers the first significant erosional response to rock uplift via establishing, lengthening, and incising canyons. Formation of internal relief here corresponds to a sharp decrease in mean basin hypsometry and increasing mean hillslope angles as glacio-fluvial erosion counterbalances, and even temporarily exceeds, rock uplift. Over 80% of the adjustment of hypsometry, peak elevations, internal relief, and mean slope angles occurs by within the first 25 km of the transition zone, suggesting that a quasi-steady state is reached within 2 to 3 Myr after the onset of glaciation and canyon cutting in the surface uplift zone. The complete transition to a steady morphology occurs gradually and cannot be defined by a sharp break in morphometric indices at the end of the transition zone. Mean hypsometry is steady between 3000 and 3500 m for all points west of the surface uplift zone. Mean slope angle levels off gradually west of Shamsi, and internal relief climbs to maximum values west of Issyk Ata. Overall, approximately 110 km of the east Kyrgyz Range shows evidence for dynamic adjustment of its geomorphology to balance erosion and rock uplift. This probably represents over 10 Myr of range propagation, and suggests that the time scale of geomorphic adjustment over active basement-cored uplifts of the Tien Shan spans back into Late Miocene time – a significant proportion of the total Cenozoic history of the northern Tien Shan.

In actively deforming the mountain ranges, the time to steady state is likely to be dependent on the efficiency of surface processes and the rates of deformation. Rapid rock-uplift rates tend to generate steep hillslopes and rivers, thereby accelerating erosion rates. Numerical models suggest that topographic steady state can be attained in <1 Myr where rates of deformation and erosion are high (equivalent to several mm/yr: Willett, 1999). Not surprisingly, in the Kyrgyz Range where rates are commonly ≤ 1 mm/yr, a longer interval is expected to be required to attain steady state.

Conclusions

Comparisons between exhumation histories derived from apatite fission-track analysis and the geomorphic evolution based on quantitative DEM analysis of the Kyrgyz Range permits a reconstruction of the entire 11 Myr evolution of the range. Exhumation of the range commenced at ca. 11 Ma in the vicinity of Ala Archa and has propagated eastward. The lateral propagation rate between Ala Archa and Shamsi is ca. 16 ± 6 km/Myr from 11 Ma to 7 Ma, and this rate has likely slowed as the range propagated farther eastward towards the Kungey Alatau. Initial rock uplift leads to rapid stripping of poorly consolidated, young sediments; rapid exhumation (almost) balances rock uplift, creating only limited surface uplift. The ca. 1.5 km-thick portion of the Chu basin which formerly overlay the range above the Cretaceous erosion surface was stripped away in 1 to 2 Myr, corresponding to the brief episode of rapid cooling documented by apatite fission-track analysis and by the zone of surface uplift defined by the presence of the regional erosion surface. Once significant amounts of more resistant basement are exposed, the exhumation rate would be expected to decrease and surface uplift rate to increase if range-normal shortening rates were maintained. However, independent data suggests that the shortening rate actually decreased, suggesting that a feedback exists between erosional efficiency and the location and magnitude of shortening. In this transition zone, drainage networks propagate into the growing range, eventually bringing erosion rates into balance with rock-uplift rates. The timescale for the majority of this geomorphic adjustment is ca. 2 to 3 Myr after uplift of the range crest through the glacial ELA and development of glacially lengthened and incised canyons. However, additional systematic adjustments to mean slope angle, hypsometry, and internal relief occur before the transition to steady morphology is complete. Overall, the evolution of the Kyrgyz Range supports a model of a systematically time-varying exhumation and shortening rates that are modulated by changes in rock erodability, the efficiency of erosion processes, and the time scale of geomorphic adjustment to surface uplift.

Acknowledgements

Dieter Rhede and Oona Appelt helped collect the electron microprobe data. Mike Bullen kindly provided unpublished apatite kinetic data from the Ala Archa section. AM acknowledges support from the DAAD. Partial funding was provided by NASA (NAG5-9039; 10520).

References

- Abbott, L.D., E.A. Silver, R.S. Anderson, R.B. Smith, J.C. Ingle, S.A. Kling, D. Haig, E. Small, J. Galewsky, and W. Sliter, Measurement of the tectonic uplift rate in a young collisional mountain belt, Finisterre Range, Papua New Guinea, *Nature*, 385, 501-507, 1997.
- Abdrakhmatov, K.E., R. Weldon, S. Thompson, D. Burbank, C. Rubin, M. Miller, and P. Molnar, Origin, direction, and rate of modern compression in the central Tien Shan, Kyrgyzstan, *Geologiya i Geofizika (Russian Geology and Geophysics)*, 42, 1585-1609, 2001.
- Abdrakhmatov, K.Y., S.A. Aldazhanov, B.H. Hager, M.W. Hamburger, T.A. Herring, K.B. Kalabaev, K.B. Kalabayev, V.I. Makarov, P. Molnar, S.V. Panasyuk, M.T. Prilepin, R.E. Reilinger, I.S. Sadybakasov, B.J. Souter, Y.A. Trapeznikov, V.Y. Tsurkov, and A.V. Zubovich, Relatively recent construction of the Tien Shan inferred from GPS measurements of present-day crustal deformation rates, *Nature*, 384 (6608), 450-453, 1996.
- Ahnert, F., Functional relationships between denudation, relief, and uplift in large mid-latitude basins, *American Journal of Science*, 268, 243-263, 1970.
- Aizen, V.B., E.M. Aizen, and J.M. Melack, Climate, snow cover, glaciers, and runoff in the Tien Shan, Central Asia, *Water Resources Bulletin*, 31 (6), 1113-1129, 1995.
- Bazhenov, M.L., A.Q. Collins, K.E. Degtyarev, N.M. Levashova, A.V. Mikolaichuk, V.E. Pavlov, and R. Van der Voo, Paleozoic northward drift of the North Tien Shan (Central Asia) as revealed by Ordovician and Carboniferous paleomagnetism, *Tectonophysics*, 366, 113 – 141, 2003.
- Bazhenov, M.L., V.S. Burtman, and A.V. Dvorova, Permian paleomagnetism of the Tien Shan fold belt, Central Asia: post-collisional rotations and deformation, *Tectonophysics*, 312 (2-4), 303-329, 1999.
- Brown, R.W., and M.A. Summerfield, Some uncertainties in the derivation of rates of denudation from thermochronologic data, *Earth Surface Processes and Landforms*, 22 (3), 239-248, 1997.

- Brozovic, N., D.W. Burbank, and A.J. Meigs, Climatic limits on landscape development in the northwestern Himalaya, *Science*, 276, 571-574, 1997.
- Bullen, M.E., D.W. Burbank, and J.I. Garver, Building the Northern Tien Shan: Integrated thermal, structural, and topographic constraints, *Journal of Geology*, 111 (2), 149-165, 2003.
- Bullen, M.E., D.W. Burbank, J.I. Garver, and K.Y. Abdrakhmatov, Late Cenozoic tectonic evolution of the northwestern Tien Shan: New age estimates for the initiation of mountain building, *Geological Society of America Bulletin*, 113 (12), 1544-1559, 2001.
- Bune, V.I., and G.P. Gorshkov, Seismic zoning territory of the USSR. Methodical bases and the regional description of the map of 1978 year [Seismicheskoe rayonirovanie territorii SSSR. Metodicheskie osnovy i regionalnoe opisanie karty 1978 goda] (In Russian), pp. 306, Nauka, Moscow, 1980.
- Burbank, D., A. Meigs, and N. Brozovic, Interactions of growing folds and coeval depositional systems, *Basin Research*, 8, 199-223, 1996.
- Burbank, D.W., and R.S. Anderson, *Tectonic Geomorphology*, 273 pp., Blackwell Science, Malden, MA, 2001.
- Burbank, D.W., J.K. McLean, M. Bullen, K.Y. Abdrakhmatov, and M.M. Miller, Partitioning of intermontane basins by thrust-related folding, Tien Shan, Kyrgyzstan, *Basin research*, 11 (1), 1999.
- Burg, J.-P., A.V. Mikolaichuk, and F.Ch. Apayarov, (editors), Digital Geological Map of the Kyrgyz Range and Chu Basin Transitional Zone, SNF, Project No 7KSPJ065518, <http://www.kyrgyzstan.ethz.ch>, Zurich, 2004.
- Burtman, V.S., Structural geology of Variscan Tien Shan, USSR, *American Journal of Science*, 275-A, 157-186, 1975.
- Carroll, A.R., S.A. Graham, E. Chang, and C.L. McKnight, Sinian through Permian tectonostratigraphic evolution of the northwestern Tarim basin, China, in *Paleozoic and*

- Mesozoic tectonic evolution of central and eastern Asia: From continental assembly to intracontinental deformation*, Memoir, Vol. 194, edited by M.S. Hendrix, and G.A. Davis, pp. 47-70, Geological Society of America, Boulder, 2001.
- Cartwright, J.A., B.D. Trudgill, and C.S. Manfeld, Fault growth by segment linkage – An explanation for scatter in maximum displacement and trace length data from the Canyonlands grabens of SE Utah, *Journal of Structural Geology*, 17, 1319-1326, 1995.
- Chediya, O.K., K.Y. Abdrakhmatov, I.H. Lamzin, G. Michel, and V. Michailov, Seismotectonic characterization of the Issyk Ata fault, pp. 58–69, Institute Nauk Kyrgyzskoi, Bishkek, 1998.
- Chediya, O.K., *Morfostruktury i noveishii tektonenez Tyan'-Shanya (Morfostructures and Neotectonics of the Tien Shan)*, 314 pp., Ilim, Frunze, 1986.
- Chediya, O.K., V.M. Yazovskii, and A.B. Fortuna, O stratigraficheskom raschlenenii krasnotsvetnogo kompleksa v Chuyskoy vpadine i yeye gornom obramlenii (The stratigraphic subdivision of the Kyrgyz red-bed complex in the Chu basin and the surrounding mountains), in *Zakonomernosti geologicheskogo razvitiya Tyan-Shanya v kaynozoye (Principles of the geologic development of the Tyan-Shan in the Cenozoic)*, pp. 26–52, Ilim, Bishkek, 1973.
- Cobbold, P.R., E. Sadybakasov, and J.C. Thomas, Cenozoic transpression and basin development, Kyrgyz Tien Shan, central Asia, in *Geodynamic Evolution of Sedimentary Basins*, edited by F. Roure, N. Ellouz, V.S. Shein, and I. Skvortsov, pp. 181-202, Editions Technip, Paris, 1996.
- Dawers, N.H., M.H. Anders, and C.H. Scholz, Growth of normal faults: Displacement-length scaling, *Geology*, 21, 1107-1110, 1993.
- Donelick, R.A., R.A. Ketcham, and W.D. Carlson, Variability of apatite fission-track annealing kinetics: II. Crystallographic orientation effects, *American Mineralogist*, 84 (9), 1224-1234, 1999.
- Dumitru, T.A., A new computer automated microscope stage system for fission track analysis, *Nuclear tracks*, 21 (4), 575-580, 1993.

- Dumitru, T.A., D. Zhou, E.Z. Chang, S.A. Graham, M.S. Hendrix, E.R. Sobel, and A.R. Carroll, Uplift, exhumation, and deformation in the Chinese Tian Shan, in *Paleozoic and Mesozoic tectonic evolution of central and eastern Asia: From continental assembly to intracontinental deformation*, Memoir, Vol. 194, edited by M.S. Hendrix, and G.A. Davis, pp. 71-99, Geological Society of America, Boulder, 2001.
- England, P.C., and P. Molnar, Surface uplift, uplift of rocks, and exhumation of rocks, *Geology*, 18 (12), 1173-1177, 1990.
- Erslev, E.A., Basement balancing of Rocky Mountain foreland uplifts, *Geology*, 14, 259-262, 1986.
- Fitzgerald, P.G., R.B. Sorkhabi, T.F. Redfield, and E. Stump, Uplift and denudation of the central Alaska Range; a case study in the use of apatite fission track thermochronology to determine absolute uplift parameters, *Journal of Geophysical Research*, 100 (10), 20,175-20,191, 1995.
- Fortuna, A.B., C.K. Kerimbekov, S.I. Kyzikov, and A.V. Mikolaichuk, Lithostratigraphic and palynologic data of Cenozoic deposits of Tessik-Sarybulak depression, in *Geology of Cenozoic and Seismotectonics of the Tien Shan*, pp. 26-39, Ilim, Bishkek, 1994.
- Green, P.F., I.R. Duddy, A.J.W. Gleadow, and J.F. Lovering, Apatite fission-track analysis as a paleotemperature indicator for hydrocarbon exploration, in *Thermal History of Sedimentary Basins: Methods and Case Histories*, edited by N.D. Naeser, and T.H. McCulloh, pp. 181-195, Springer-Verlag, New York, 1989.
- Green, P.F., I.R. Duddy, G.M. Laslett, K.A. Hegarty, A.J.W. Gleadow, and J.F. Lovering, Thermal annealing of fission tracks in apatite, 4, Quantitative modelling techniques and extension to geological timescales, *Chem. Geol. (Isotope Geosci. Sec.)*, 79, 155-182, 1989.
- Gubin, I.E., *Lithosphere of Tien Shan*, 158 pp., Nauka, Moscow, 1986.
- Gupta, A., and C. Scholz, A model of normal fault interaction based on observations and theory, *Journal of Structural Geology*, 22, 865-879, 2000.

- Hallet, B., L. Hunter, and J. Bogen, Rates of erosion and sediment evacuation by glaciers: a review of field data and their implications, *Global Planetary Change*, 12, 213-235, 1996.
- Hendrix, M.S., S.A. Graham, A.R. Carroll, E.R. Sobel, C.L. McKnight, B.J. Schuelein, and Z. Wang, Sedimentary record and climatic implications of recurrent deformation in the Tian Shan: Evidence from Mesozoic strata of the north Tarim, south Junggar, and Turpan basins, Northwest China, *Geological Society of America Bulletin*, 104 (1), 53-79, 1992.
- Howard, A.D., A detachment-limited model of drainage basin evolution, *Water Resources Research*, 30, 2261-2285, 1994.
- Howard, A.D., and G. Kerby, Channel changes in badlands, *Geological Society of America Bulletin*, 94, 739-752, 1983.
- Hurford, A.J., and P.F. Green, The zeta age calibration of fission-track dating, *Chemical Geology*, 41 (4), 285-317, 1983.
- Ketcham, R.A., R.A. Donelick, and M.B. Donelick, AFTSolve: A program for multi-kinetic modeling of apatite fission-track data, *Geological Materials Research*, 2 (1), 1-32, 2000.
- Ketcham, R.A., R.A. Donelick, and W.D. Carlson, Variability of apatite fission-track annealing kinetics: III. Extrapolation to geological time scales, *American Mineralogist*, 84 (9), 1235-1255, 1999.
- Kooi, H., and C. Beaumont, Large-scale geomorphology: classical concepts reconciled and integrated with contemporary ideas via a surface processes model, *Journal of Geophysical Research*, 101, 3361-3386, 1996.
- Krilov, A.Y., Absolute age of the rocks of the Central Tien Shan and application of Argon methods to metamorphic and sedimentary sediments, in *Determination of the Absolute Age of Pre-Quaternary Formations*, edited by I.E. Starik, pp. 222-224, Nedra, Moscow, 1960.

- Leeder, M., R., and J.A. Jackson, The interaction between normal faulting and drainage in active extensional basins, with examples from the western United States and central Greece, *Basin Research*, 5, 79-102, 1993.
- Makarov, V.I., *New tectonic structure of the Central Tien Shan*, 172 pp., Nauka, Moscow, 1977.
- Mancktelow, N.S., and B. Grasemann, Time-dependent effects of heat advection and topography on cooling histories during erosion, *Tectonophysics*, 270, 167-195, 1997.
- Masek, J.G., and C.C. Duncan, Minimum-work mountain building, *Journal of Geophysical Research*, 103, 907-917, 1998.
- Mikolaichuk, A., E. Sobel, M. Gubrenko, and A. Lobanchenko, Structural Evolution of the Tien Shan Orogenic Northern Margin, *Proceedings of the National Academy of Sciences of Kyrgyz Republic*, 4, 50-58, 2003.
- Mikolaichuk, A.V., The structural position of thrusts in the recent orogen of the Central Tien Shan, *Russian Geology and Geophysics*, 41 (7), 961 - 970, 2000.
- Oskin, M., and D.W. Burbank, Alpine landscape evolution dominated by cirque retreat, *Geology*, in review.
- Reigber, C., G.W. Michel, R. Galas, D. Angermann, J. Klotz, J.Y. Chen, A. Papschev, R. Arslanov, V.E. Tzurkov, and M.C. Ishanov, New space geodetic constraints on the distribution of deformation in Central Asia, *Earth and Planetary Science Letters*, 191 (1-2), 157-165, 2001.
- Royden, L., Coupling and decoupling of crust and mantle in convergent orogens: Implications for strain partitioning in the crust, *Journal of Geophysical Research*, 101 (B8), 17679-17705, 1996.
- Sadybakasov, I.S., *Neotektonika Vysokoi Azii (Neotectonics of the High Asia)*, 181 pp., Nauka, Moscow, 1990.
- Schmidt, K.M., and D.R. Montgomery, Rock mass strength assessment for bedrock landsliding, *Environmental & Engineering Geoscience*, 2 (325-338), 1996.

- Shvartzman, Y.G., Thermal field, seismicity and geodynamics of the Tien Shan, Unpub. Ph.D. dissertation thesis, University of Kyrgyzstan, Bishkek, 1992.
- Sklar, L.S., and W.E. Dietrich, Sediment and rock strength controls on river incision into bedrock, *Geology*, 29, 1087-1090, 2001.
- Sobel, E., A. Mikolaichuk, J. Chen, and D. Burbank, Development of the Late Cenozoic Central Tian Shan in Kyrgyzstan and China Recorded by Apatite Fission Track Thermochronology, in *AGU Fall meeting*, pp. F1156, 2000.
- Sobel, E.R., and M.R. Strecker, Uplift, exhumation, and precipitation: Tectonic and climatic control of Late Cenozoic landscape evolution in the northern Sierras Pampeanas, Argentina, *Basin Research*, 15, doi: 10.1046/j.1365-2117.2003.00214.x, 2003.
- Sobel, E.R., and T.A. Dumitru, Exhumation of the margins of the western Tarim basin during the Himalayan orogeny, *Journal of Geophysical Research*, 102 (B3), 5043-5064, 1997.
- Sobel, E.R., Basin analysis of the Jurassic - Lower Cretaceous southwest Tarim basin, NW China, *Geological Society of America Bulletin*, 111 (5), 709-724, 1999.
- Sobel, E.R., D. Seward, G. Ruiz, A. Kuonov, H. Ege, M. Wipf, and C. Krugh, Influence of Etching Conditions on Dpar Measurements: Implications for Thermal Modeling, in *International Fission Track Workshop*, Amsterdam, 2004.
- SRTM, 2003
- Stock, J.D., and D.R. Montgomery, Geologic constraints on bedrock river incision using the stream power law, *Journal of Geophysical Research-Solid Earth*, 104 (B3), 4983-4993, 1999.
- Stüwe, K., L. White, and R. Brown, The influence of eroding topography on steady-state isotherms; application to fission track analysis, *Earth and Planetary Science Letters*, 124 (1-4), 63-74, 1994.
- Talling, P.J., M.D. Stewart, C.P. Stark, S. Gupta, and S.J. Vincent, Regular spacing of drainage outlets from linear fault-blocks, *Basin Research*, 9, 275-302, 1997.

- Thompson, S.C., R.J. Weldon, C.M. Rubin, K. Abdrakhmatov, P. Molnar, and G.W. Berger, Late Quaternary slip rates across the central Tien Shan, Kyrgyzstan, central Asia, *Journal of Geophysical Research-Solid Earth*, 107 (B9), 2002.
- Trofimov, A.K., N.F. Udalov, N.G. Utkina, F.B. Fortuna, O.K. Chediya, and V.M. Yazovskii, *Geologiya kainozoya Chuiskoi vpadiny i ee gornogo obramleniya (Cenozoic Geology of the Chu Depression and Its Mountainous Surroundings)*, 128 pp., Nauka, Leningrad, 1976.
- Whipple, K.X., and G.E. Tucker, Dynamics of the stream-power river incision model: Implications for height limits of mountain ranges, landscape response timescales, and research needs, *Journal of Geophysical Research-Solid Earth*, 104 (B8), 17661-17674, 1999.
- Whipple, K.X., Bedrock rivers and the geomorphology of active orogens, *Ann. Rev. Earth Planet. Sci.*, 32, 151-185, 2004.
- Willett, S.D., and M.T. Brandon, On steady states in mountain belts, *Geology*, 30 (2), 175-178, 2002.
- Willett, S.D., Orogeny and orography: The effects of erosion on the structure of mountain belts, *Journal of Geophysical Research-Solid Earth*, 104 (B12), 28957-28981, 1999.
- Yin, A., S. Nie, P. Craig, T.M. Harrison, F.J. Ryerson, X.L. Qian, and G. Yang, Late Cenozoic tectonic evolution of the southern Chinese Tian Shan, *Tectonics*, 17 (1), 1-27, 1998.
- Zhang, P., P. Molnar, and W.R. Downs, Increased sedimentation rates and grain sizes 2-4 Myr ago due to the influence of climate change on erosion rates, *Nature*, 410, 891-897, 2001.

Figures:

Figure 1. A. Topographic map of central Asia, showing locations of the Tien Shan with respect to adjacent plateaus and basins. The Kyrgyz Range forms the northern margin of the central Tien Shan. B. Topography of the Kyrgyz Range derived from 3 arcsec digital elevation model [SRTM, 2003]. Darker shades correspond to lower topography. Locations of apatite fission track (FT) samples from *Bullen et al.* [2001; 2003] and this study shown. Irregular outline defines east half of range analyzed in C and in Figure 4. C. Mean slope angle, mean elevation, and maximum elevation of the east half of the Kyrgyz Range measured in 10 km-wide swaths. Arrows point to area of analysis of B contained within white outline.

Figure 2. Map of the Kyrgyz range and adjacent basins, modified from *Mikolaichuk et al.* [2003]. Isopachs show depth to basement; Cenozoic strata of the Chu basin constitutes the majority of this sediment. The ranges are composed of Paleozoic units; Mesozoic units are virtually absent.

Figure 3. Shaded relief image and map of exhumed pre-Cenozoic erosion surface remnants of the easternmost Kyrgyz Range. Darker patches are mapped surface remnants with average southward dip shown in degrees. Lighter patches show extent of late Pleistocene glaciation shown. Reverse fault system bounds northern edge of range. Ages and sample locations from Shamsi River transect show complete exhumation of apatite fission-track partial annealing zone northwest of tilted erosion surface outcrops.

Figure 4. A. Topographic characteristics of north-facing basins along the length of the Kyrgyz range. Measured basins are shown directly below in B. Peak heights are highest elevations at the edge of each basin. Hypsometry shows median elevation bounded by 75th and 25th percentile

elevations. The difference between these is the hypsometric range, shown shaded as medium grey. Internal relief is measured as the difference between the highest and lowest elevations that are the same distance upstream from the basin outlet. The 75th percentile of the distribution of internal relief within each basin plotted with area beneath this curve shaded dark grey. Surface uplift zone shows sharp increase in peak elevation, hypsometry, and internal relief from east to west in proportion to structural growth of the Kyrgyz Range. Adjustment zone shows progressive increases in mean slope angle, hypsometric range, and internal relief as north-facing basins expand and incise uplifted bedrock. These same morphometric indices are constant in the steady morphology zone.

Figure 5. Examples of progressive expansion and deepening of north facing basins. Komorchek lies at the transition from the surface uplift to the adjustment zone; Tchuk lies within the adjustment zone; Ala Archa lies within the steady morphology zone. Erosion from Komorchek to Tchuk is dominated by southward expansion of basins, probably via glacial cirque retreat. Prominent convexity in stream profile at Tchuk is a result of insufficient fluvial erosion downstream of glacially expanded valley. Erosion from Tchuk to Ala Archa dominated by removal of convexity by fluvial and glacial incision. Internal relief shown graphically as the shaded region between river longitudinal profile and equidistant ridge line elevations, where distance is measured up main and tributary streams to the divide. Internal relief effectively captures deepening of basins in adjustment zone.

Figure 6. Schematic illustration of the affect of differing total annealing temperatures (T_a) on complex cooling paths. The 4 vertical elevation profiles (A to D) represent a sequence of exhumation (cooling) and burial (reheating) events. The upper panel of each pair shows the evolving temperature history; the lower panel represents the distribution of apatite fission-track ages in a vertical profile at the corresponding time step. Each profile shows the cooling path of

apatites that are more (solid line) and less (dashed line) resistant to annealing. The base of the partial annealing zone (PAZ) for each type of apatite is considered to be the respective T_a . Exhumation and burial events are (unrealistically) depicted as instantaneous for clarity. The geothermal gradient is assumed to remain constant and advection of isotherms is neglected for simplicity.

A. A large deformation event followed by a long period of quiescence gives shallow samples a common age. More resistant apatites are reset at lower elevation (hotter temperature); therefore, the slope of the more resistant cooling path is steeper in the PAZ.

B. Large exhumation event at time t_1 forms exhumed PAZ₁. A new PAZ forms at depth.

C. Section is buried and reheated beneath sediments of a sedimentary basin at time t_2 . Heating resets all apatites below their respective T_a . Exhumed PAZ₁ is partially reset. In the lower part of the current PAZ, cooling paths for apatites with different T_a may be parallel. If the exhumation event was large enough to shift the entire PAZ₁ to a temperature hotter than the appropriate T_a , then the exhumed PAZ₁ would be completely overprinted.

D. A second large exhumation event creates new exhumed PAZ₂ at time t_3 . Ongoing exhumation could subsequently expose the entire exhumed PAZ in mountainous topography. If the simplifying thermal assumptions are correct, the shape of the age-elevation curve can be used to reconstruct the magnitude of thermal events. The difference between the magnitude of exhumation t_1 (a) and burial (b) is equal to the difference between the base of PAZ₁ and the base of PAZ₂ (c) (for a given apatite type). Therefore, if the base of PAZ₁ and PAZ₂ can be determined and the magnitude of burial can be constrained by thermal modeling or independent geological data, it is possible to estimate the magnitude of exhumation that occurred at t_1 .

Figure 7. Fission-track age plotted versus elevation for the Boom Gorge, Shamsi, Issyk Ata, and Ala Archa sections (from left to right; east to west). All samples are plotted on a common vertical axis. Boom Gorge is in the footwall; other sections are in the hanging wall. Inset in upper right shows the young portion of the 3 hanging wall sections. Numbers next to samples indicate kinetic character of apatite; italics denote wt%Cl; normal text denotes Dpar. Ala Archa data is from *Bullen et al.* [2003]; Dpar values from this profile are not directly comparable with other Dpar values shown as Dpar measurements depend on both the operator and the etching conditions [Sobel *et al.*, 2004]. Upper dashed line indicates the maximum peak elevation. Lower dashed line indicates position of base of exhumed PAZ for low-chlorine apatite. Fine dashed line shows approximate age-elevation path, constructed following Fig. 6. Amount of exhumation calculated using a geothermal gradient of 26°C/km [Gubin, 1986] and the T_a (Table 2). Thermal conductivity of young sediments and basement were not differentiated. Grey region indicates average thickness of sedimentary basin that could have formerly overlain the range; the upper and lower limits are \pm ca. 300 m. The image at the top shows a Multispectral scanner image draped over an SRTM DEM, depicting the view of the range looking from the north. White circles denote the location of partially reset fission-track samples; grey circles denote fully reset samples.

Figure 8. Representative track-length models for the Shamsi and Boom Gorge profiles. See text for modeling details. Boom Gorge sample modeled using 0.07wt% Cl, chosen by comparison with other samples to be equivalent to Dpar of 1.70 μ m.

Figure 9. Schematic evolution of topography in the Kyrgyz range, showing the effect of contrasting lithologies on exhumation and surface uplift rates.

A. Oligocene Early Miocene foreland basin deposited above regional erosion surface.

B. Rapid exhumation of sediments in hanging wall of thrust causes rapid cooling but slow surface uplift of range.

C. As the area of exposed basement increases relative to young sedimentary cover, erosion rates decrease, leading to increasing surface uplift rates.

D. Range becomes large enough to create an orographic barrier and subsequently place upper portion of the range above the Equilibrium Line Altitude (ELA). Glacial erosion causes drainage basins on windward side to expand at the expense of more arid, less deeply incised basins on the leeward side.

Figure DR1. Characterization of apatite samples. Compositional data are plotted for all samples. Track-length histograms are only plotted for samples with a significant number of measurements.

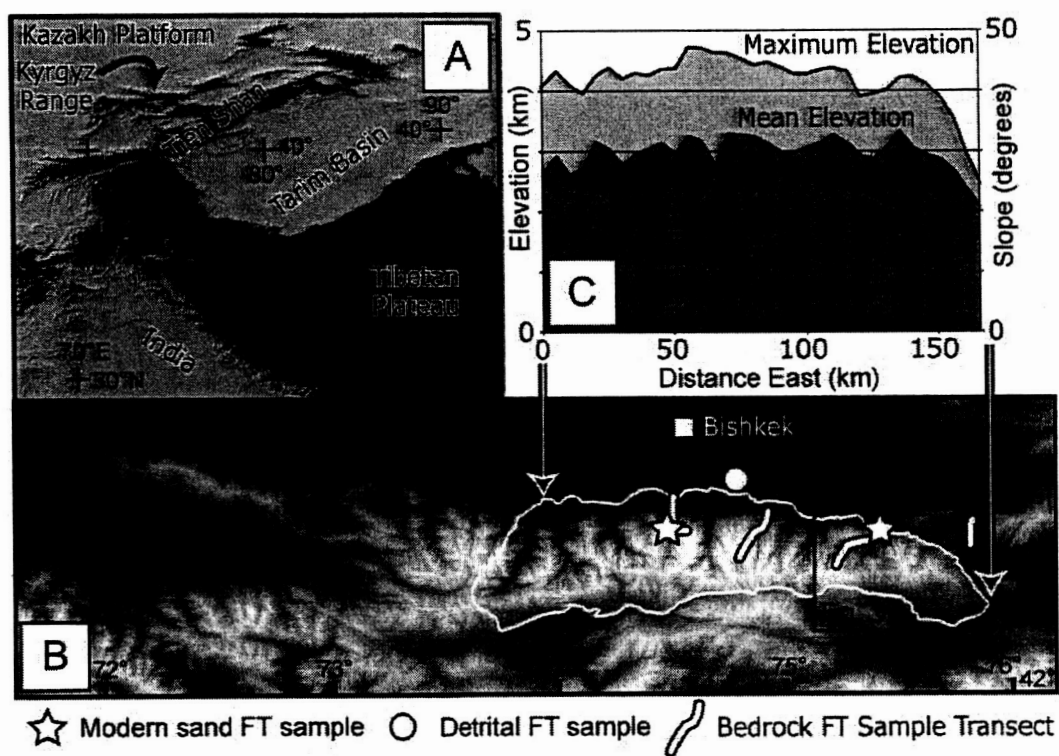


Figure 1, Sobel et al.

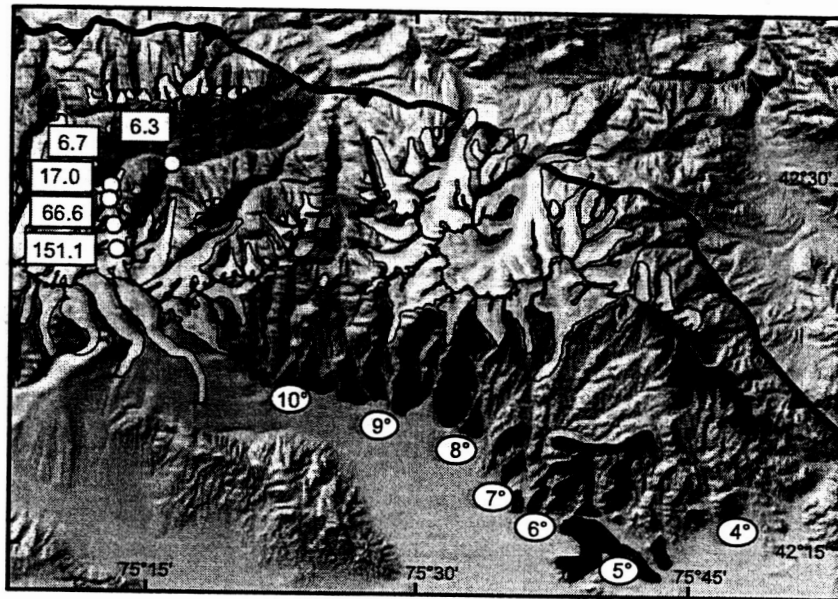


Figure 3, Sobel et al.

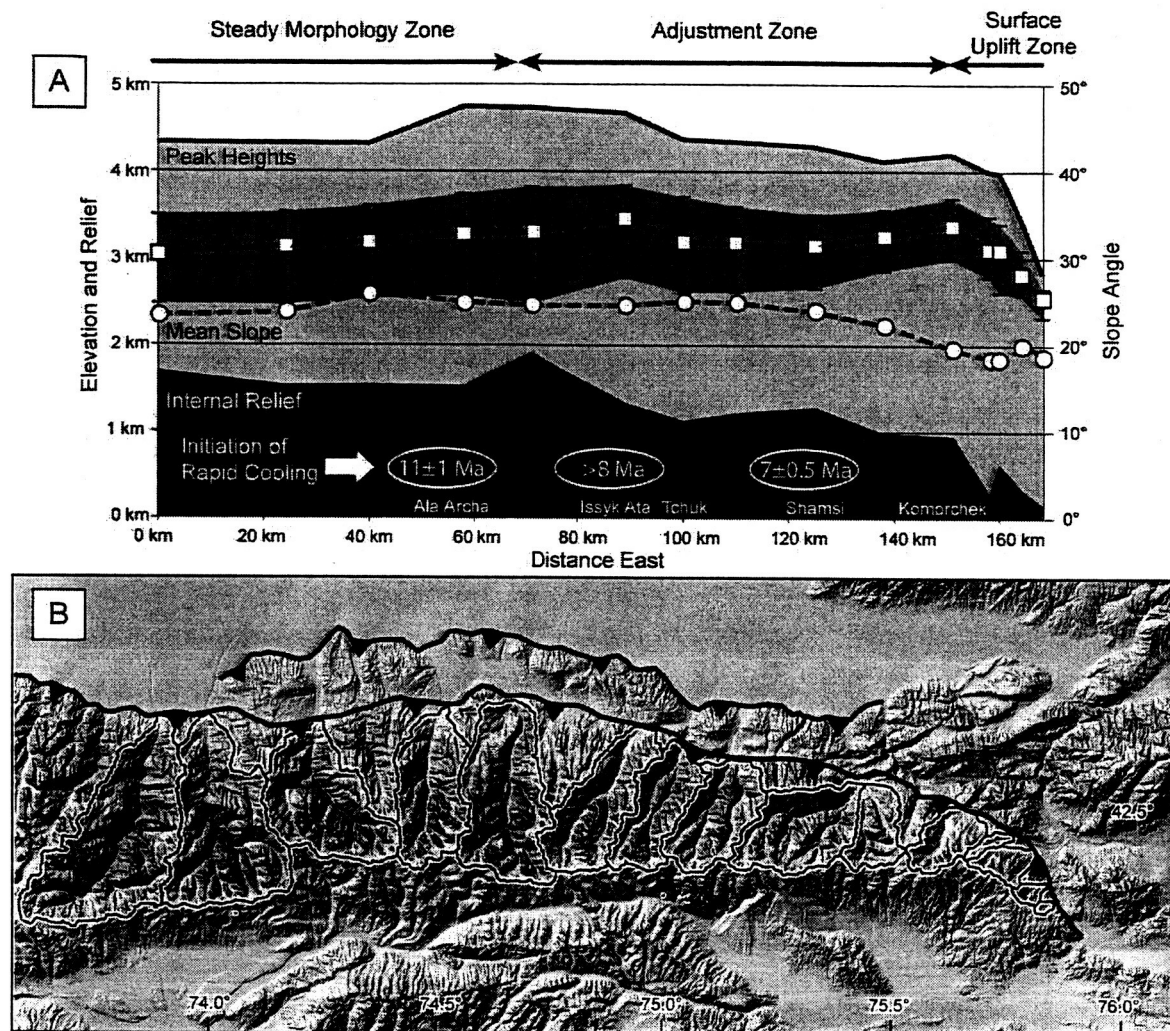


Figure 4, Sobel et al.

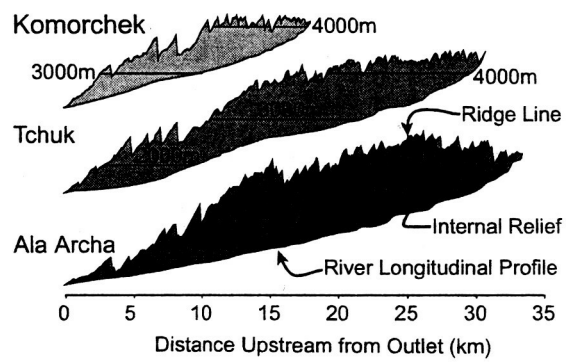
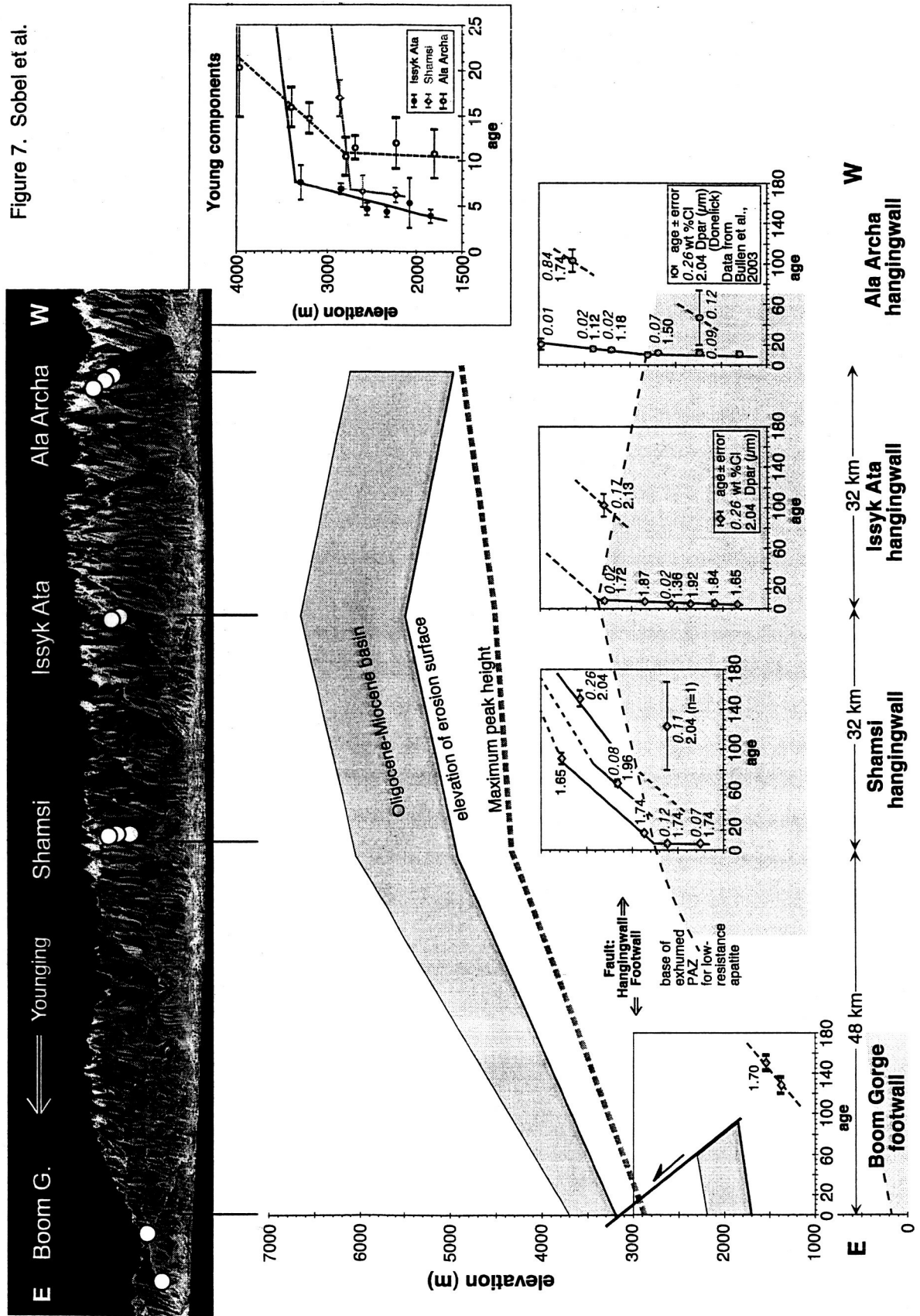


Figure 5, Sobel et al.

Figure 7. Sobel et al.



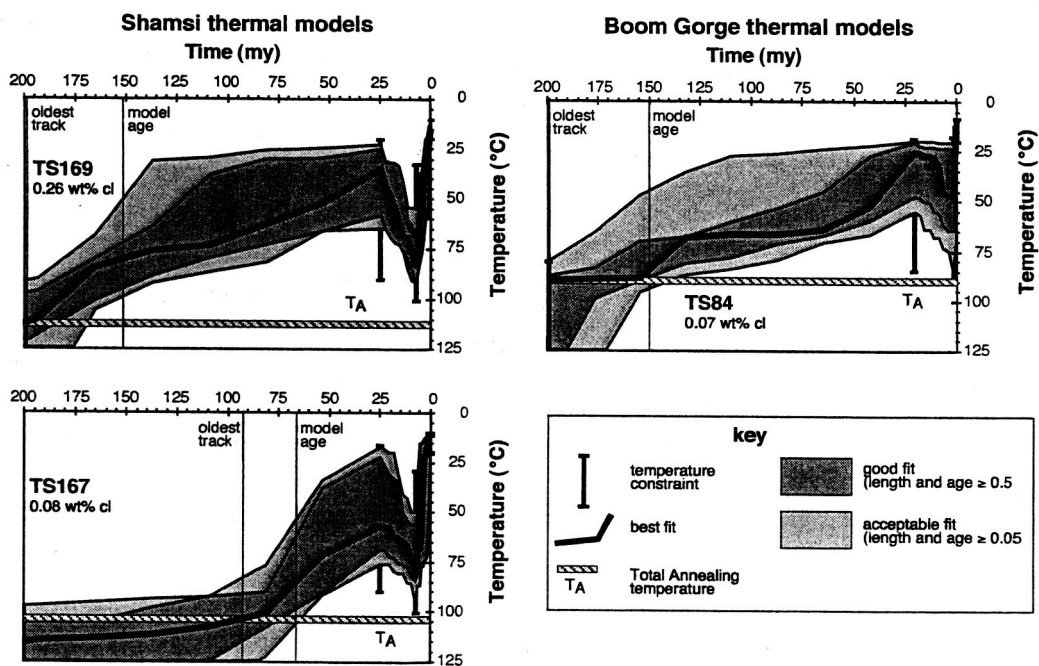


Figure 8, Sobel et al.

Landscape Development Model

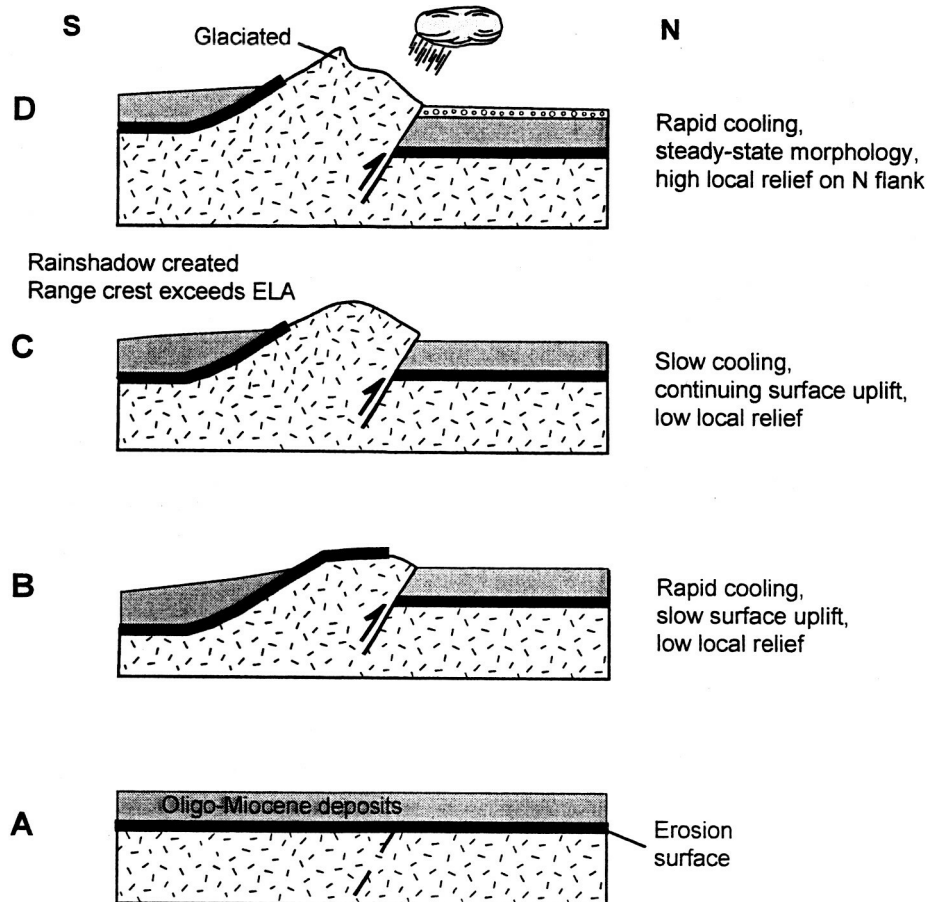


Figure 9, Sobel et al.

Table 1. Fission track data from the Kyrgyz range

sample	irradiation code	comp- onent	age	lithology	N long	E lat	altitude (gps)	m	XI*	No	Rho-S ($\times 10^5$)†	NS §	Rho-I ($\times 10^5$)†	NI §	P(χ^2) (%)	Rho-D ($\times 10^6$) **	ND ††	Age $\pm \sigma$ (Ma)	U ppm	Dpar (μm)	stdv (μm)	Cl wt%	length (μm)	error (μm)	stdv (μm)	No
Issyk Ata																										
TS161	UP32-13+	O3		granite	42°	74°	3350	3290	31	1.9880	145	11.750	857	0	1.3330	5420	24.5	7.6	11.0	1.85	0.29	0.10	12.92	0.32	1.63	26
	UP43-6+	young							25	0.3097	17	10.040	551	93	1.3330	5420	7.6	1.9	9.4	1.72	0.16	0.02				
	UP43-7	old							6	7.0970	128	16.980	306	0	1.3330	5420	102.0	11.0	15.9	2.13	0.34	0.17				
TS159	UP32-12	O3		granite	31.108	52.425	na	2850	20	1.0280	132	33.790	4338	8	1.2330	5034	6.9	0.6	34.3	1.87	0.14		13.50	0.49	1.37	8
TS158	UP32-11	O3		granite	32.364	52.178	2560	2560	25	0.5357	47	25.620	2248	99	1.2260	5034	4.7	0.7	26.1	1.36	0.09	0.02				0
TS162	UP43-8	O3		granite	33.391	53.351	2380	2350	31	0.4456	59	24.740	3275	24	1.3240	5420	4.4	0.6	23.4	1.92	0.08		13.44	0.07	0.10	2
TS163	UP43-9	R		metavolc	34.854	54.187	2060	2090	4	0.4827	4	21.600	179	74	1.3140	5420	5.4	2.8	20.5	1.84	0.35					0
Mav38	UP65-10+11	O3		granite	37.912	55.100	1840		34	0.2850	34	1.480	1765	93	1.0847	4531	3.9	0.7	17	1.65	0.25					
Shamsel																										
TS170	UP32-16	C2-3		sandstone	27.344	14.024	3865	3770	22	4.814	636	12.120	1601	4	1.2580	5034	91.1	5.6	12.0	1.65	0.13	0.12	12.58	0.33	1.53	22
TS169	UP32-15	C1		sandstone	27.751	13.944	3697	3570	19	16.2100	836	24.530	1265	22	1.2520	5034	151.1	7.7	24.5	2.04	0.16	0.26	12.06	0.17	1.69	100
TS167	UP43-12	C1		sandstone	28.237	13.135	3254	3160	24	4.0790	661	14.470	2344	18	1.2850	5420	66.6	3.4	14.1	1.96	0.14	0.10	11.89	0.26	1.88	52
TS166	UP32-14	C1		sandstone	29.301	12.973	2930	2870	22	1.0780	146	13.930	1886	35	1.2450	5034	17.0	2.0	14.0	1.74	0.15		14.38	0.47	0.95	4
TS165	UP43-11	C1		sandstone	29.830	12.996	2670	2610	12	0.6100	27	12.700	562	0	1.2950	5420	13.7	7.0	12.3	1.80	0.21	0.12	12.95			1
		young							11	0.3629	15	13.040	539	62	1.2950	5420	6.7	1.8	12.6	1.74	0.17	0.12				
		old							1	4.1030	12	7.864	23	na	1.2950	5420	123.6	44.1	7.6	2.04	na	0.11				
TS164	UP43-10	C1		sandstone	30.739	16.158	2280	2250	20	0.3551	63	13.590	2412	85	1.3040	5420	6.3	0.8	13.0	1.74	0.11	0.07	11.99	0.97	2.57	7
Boom Gorge																										
TS84	UP30-17	P		granite	32.688	48.867	1530	1620	20	9.694	826	15.410	1313	84	1.3070	5224	150.2	7.6	14.7	1.70	0.11		12.50	0.23	1.99	73
TS27	UP2-20	D-C3		sandstone	38.010	50.562	1376	na	12	6.378	569	9.394	838	12	1.0510	4299	127.5	10.1	11.2	na	na		12.82	0.20	1.96	100

Notes: Sample preparation and analysis were similar to that outlined in Sobel and Strecker (2003). Samples analyzed with a Leica DMRM microscope with drawing tube located above a digitizing tablet and a Kinetek computer-controlled stage driven by the FTStage program (Dumitru, 1993). Analysis performed with reflected and transmitted light at 1250x magnification. Samples were irradiated at Oregon State University, USA except TS27, which was irradiated at Risø National Laboratory, Denmark. Following irradiation, the mica external detectors were etched with 21°C, 40% hydrofluoric acid for 45 minutes. The pooled age (central age) is reported for samples with $P(\chi^2)$ greater than (less than) 5% as they pass (fail) the χ^2 test; error is one sigma, calculated using the zeta calibration method (Hurford and Green, 1983) with zeta of 369.6 ± 7.6 for apatite (E. Sobel, unpublished). Sample TS27 calculated with a zeta of 361 ± 20 (E. Sobel, unpublished). Note that 3 slides were combined for sample TS161 and 2 for Mav38.

*No XIs is the number of individual crystals dated. †Rho-S and Rho-I are the spontaneous and induced track density measured, respectively (tracks/cm²). §NS and NI are the number of spontaneous and induced tracks counted, respectively. # $P(\chi^2)$ (%) is the chi-square probability (Galbraith, 1981; Green, 1981). **Rho-D is the induced track density in external detector adjacent to CN5 dosimetry glass (tracks/cm²). ††ND is the number of tracks counted in determining Rho-D. Microprobe measurements were performed with PAP correction procedures, operating conditions of 15kV beam, beam current of 20 nA (measured on a Faraday cup) and a ca. 15 μm beam diameter. Chlorine was measured for 100 seconds, providing a ca. 150 ppm detection limit. Calibration included a Durango apatite standard which was repeatedly measured during the course of analysis.

Table 2. Summary of AFTSolve model results.

	TS169		TS167	
	min	max	min	max
Ta (°C)	112	113	100	103
Tmin (°C), pre-Cz seds	35	50	57	57
Tmax (°C) beneath Cz seds	81	84	75	82
burial beneath Cz seds (km)	1.2	1.8	0.7	1.0
Wt% Cl		0.26		0.08

Data summarized from all model runs that yielded good fits to the observed data.